# *Optical Conveyor-Belt Transport of Cs and Rb Atoms*

ALEX MATTHIES

MATTHIES, ALEX (2023) Optical Conveyor-Belt Transport of Cs and Rb Atoms. Doctoral thesis, Durham University.

# Optical Conveyor-Belt Transport of Cs and Rb Atoms

Alex J. Matthies

A Thesis presented for the degree of

Doctor of Philosophy

Department of Physics
Durham University, UK
July 2023

# Abstract

In this thesis the fast and efficient transport of Caesium and Rubidium atoms using an optical conveyor-belt is presented. Up to $7 \times 10^7$ atoms of either species can be transported in under 25ms across the 37.2cm gap between the MOT Chamber, where they are initially cooled, and the Science Cell, where future experiments will be performed. Once in the Science Cell, either species can be evaporatively cooled to form a Bose-Einstein condensate. Simultaneously loading both species into the optical-conveyor belt did not lead to a reduction in the transport efficiency of either species.

Our transport scheme was able to avoid the use of more complicated Bessel beams or variable-focus lenses by carefully choosing the waists and focus positions. To that end detailed calculations of the trapping potential were performed to find the optimum beam parameters. It was found that separating the focus positions of the two transport beams can lead to dramatic increases in the minimum trap depth. The use of magnetic coils at the start and end of the transport path, to compensate for the effect of gravity, was also found to be highly beneficial. Beam waists of $195\mu$m and focus positions 6.6cm from each end of the transport paths were found to be optimum for both species.

The setup and implementation of the two transport beams is presented and the performance of the transport characterised. The equations of motions of several different transport trajectories are derived and compared both theoretically and experimentally. The performance of the Minimum Jerk Trajectory was found to be the best, with that of the Minimum Snap Trajectory a close second. The characterisation measurements allow insight to be gained into different loss mechanism during transport.

# Contents

# Declaration

The work in this thesis is based on research carried out at the Department of Physics, Durham University, United Kingdom. No part of this thesis has been submitted elsewhere for any other degree or qualification. Where material has been generated by joint work, the work of others has been indicated.

Alex Matthies
July 2023

# Acknowledgements

I feel it has become cliche to start thesis acknowledgements talking about how hard the process of doing a PhD is. Aside from a these two sentences of meta-commentary, I will not be departing from this. Doing a PhD is challenging at the best of times, and with the way the 2020s have been going so far I've hardly picked an easy time. I am enormously thankful for everyone who helped my along the way. I always knew this would be a long list if/when I got this far but it has still turned out far longer than I anticipated.

First off, I'd like to thank my supervisor Simon Cornish for all his help and support throughout my nearly four years in Durham. For his depth of knowledge, suggestions of what else to consider and how the work could be better understood and improved.

Secondly, I'd like to thank everyone I've shared a lab with. My fellow PhD students Jonathan, Mew, Andrew and Adarsh and post-docs Sarah, Lewis, Phil and Alex. I learned a lot from all of you. I joined a large lab with several simultaneous projects, but when I needed help or to talk things through there was always someone happy to lend a hand or an ear. My days in the lab working closely with someone else where by far the best.

The work in this thesis could not have been done without the amazing help from the department's technical and admin staff. In particular I'd like to thank Kevin Ring, Malcolm Robertshaw, Hannah Frost, Andrew Hunter, Robert Platt, Fabrice Wandji, John Dobson, Wayne Dobby, Michael Armstrong and Joanne Lakey. They were always warm, welcoming and happy to help no matter if it was something I barely knew how to ask about or if I was showing up for the third time to annoy them about the same thing.

Outside of my lab I feel lucky to have found myself in a wonderful research group. In particular I'd like to thank Jude, Karen, Bethan, Lucy, Dani, Kali, Dan, Luke, Tobias, Jack, Mitch, Hannah, Kev and Ifan.

Kev and Ifan I am especially thankful to for their heroic efforts that ensured my viva could take place as planned.

My friends from undergrad Abhijay, Rhidian, Griffin and Benjamin kept me sane

for the first lockdown and Alavya was an amazing housemate to spend the second lockdown with.
Moving to Durham after an undergrad in London was daunting to say the least. The lockdowns did not help. But the communities I found during and afterwards were more than I ever could have imagined and I am immensely grateful for them. Jude, Karen, Bethan (all again), Mal, Robin and Tal all made Durham a place close to my heart and always managed to brighten my week whether it was at the climbing wall, chatting about a book or spending far too long in a coffee shop. Outside of Durham: Floor, Rebecca, Kathryn, Rosa, Neve, Bethan S, Sarah H, Mamoud, Chantelle, Dawn, Amy, Fran, Andrea, Katie, Iain and James. You've all helped and supported me more than you realise even if it was just some much needed time away.

To my parents Jana and Karsten and to my brother Freddie for the all support, encouragement and enthusiasm.

But most of all to Marian. For the support and understanding at the worst times, for the excitement and encouragement at the best times and for the never-ending love.

*I know histories of nations I'll never have chance to visit*
*Complexities of science and language with great precision*
*But in the end I've seen nothing of what's been given*
*This life that I've employed, while I love it, it has its limits*
*The failing I regret, though it's painful, I must admit it*
*For everything I know of this world, I never lived it*
– Zack Hemsey, The Pursuit Of Knowledge

*"My life amounts to no more than a single drop in a limitless ocean.*
*Yet what is an ocean but a multitude of drops?"*
– David Mitchell, Cloud Atlas

# CHAPTER 1

# Introduction

Techniques to cool and trap atoms have enabled many fascinating and varied experiments including quantum simulation [1–4], quantum computing [5], quantum sensing [6] and high-precision measurements [7, 8]. These techniques include Zeeman slowers, magneto-optical traps, Sisyphus cooling, optical molasses, degenerate Raman sideband cooling and evaporative cooling in either optical or magnetic traps [9–17]. While these techniques are routinely implemented, they often carry specific requirements to implement successfully. For example, some techniques rely on multiple orthogonal laser beams to ensure cooling in all three spatial dimensions. Other techniques are based on carefully engineered combinations of optical and magnetic fields. Many experiments require multiple cooling techniques to reach cold or even ultracold temperatures and vacuum systems must be tailored to the requirements of the various cooling techniques.

Ultracold polar molecules are a natural extension to experiments with cold atoms as they open up new possibilities for quantum simulation [18–27], as well as quantum computing [28–34] and high-precision measurements [35–38]. This is due to their long-ranged dipole-dipole interactions [39, 40], long coherence times [41–46] and complex internal energy levels with electronic, vibrational, rotational and hyperfine structure. An important recent development is the realisation of the first quantum gas microscope of molecules [47, 48]. Alternative platforms for quantum simulation include trapped ions [49–51], superconducting circuits [52, 53], magnetic atoms [54–57] and Rydberg atoms [4, 58, 59].

## 1.1 The Need for Transport

As a result of the many different required cooling techniques, transport is necessary to increase the optical access to the experiment. Transport schemes that quickly and efficiently transfer atoms from one region of a vacuum system to another enable experiments of ever increasing complexity. Transport also enables atoms to be interfaced with other experimental components such as microwave cavities for studies of quantum electro-dynamics [60, 61], hollow-core fibres [62, 63], nanofibres [64] and mixtures of ions and atoms [65]. Transport has also enabled the investigation of quantum gas microscopy [66–73]. In these experiments atoms are loaded into an optical lattice and a high numerical aperture objective lens is used to collect florescence light, allowing for site-resolved imaging. This allows quantum simulation to be performed [1–3], where many-body systems that are impossible to simulate on a classical computer are mapped onto a quantum system in which the dynamics can be measured directly. For single-site imaging to be realised, the microscope objective lens must be placed close to the atoms. Hence, nearly all quantum gas microscopes require a vacuum system with two distinct regions and transport to be performed between them.

Another type of experiment that benefits greatly from atomic transport are experiments using multiple atomic species. Experiments utilising ultracold mixtures of different atomic species are of great interest due to the rich interplay between intra- and inter-species interactions. These enable studies of quantum-degenerate mixtures [74–80], Effimov physics [81–84] and impurity physics [85, 86]. Experiments with two different atomic species also enable the formation of ultracold heteronuclear molecular gases [47, 87–100]. While ultracold molecules formed from the association of cold atoms are currently capable of producing the coldest and densest sample, direct cooling of molecules shows much promise [101–109].

However, including a second or even a third species invariably increases the experimental complexity. The number of beams or even cooling techniques required increases considerably, enhancing the need for optical transport. Hence, the development of transport techniques that are compatible with the different properties and requirements of multiple atomic species are important for the continued development of ultracold mixture and molecule experiments. Additionally, increased experimental complexity often leads to longer duty cycles, driving the the need for fast and efficient transport.

## 1.2 Transport Methods

A variety of atomic transport schemes have been developed and implemented, each with their advantages and limitations. They can be broadly categorised into schemes based on either magnetic or optical traps.

Magnetic transport schemes are either based on a single coil that is moved mechanically [110–113] or a series of overlapping coils with time-varying currents [114–116]. These schemes have been demonstrated to work over long distances with minimal heating [114] and over short distances for precise positional control [115]. Magnetic traps have the advantage of a larger trap depth and volume, however they can take up a significant amount of optical access and often require transport times of several seconds. Additionally they are only viable for species with magnetically trappable states that are stable against inelastic collisions.

Optical transport schemes can be used for all atomic species, independent of internal ground state. They require significantly less space than magnetic transport schemes, making them usable for a much greater range of experiments. The most straightforward method uses a translation stage to move the focus position of a single Gaussian beam optical dipole trap [117–119]. However the translation stage can be a significant source of mechanical vibrations and this scheme suffers from weak axial confinement along the propagation direction, and hence transport direction, which leads to elongated atomic clouds. The technical limits on the moving parts typically lead to long transport times. Variations of the scheme have also been demonstrated, including passing two beams through the translated lens to form a shallow-angle crossed optical dipole trap [120] or a pair of translation stages to shift the position of a lattice [121]. Using a variable-focus lens: either an electrically tunable liquid-based lens [122] or a phase-pattern Moiré lens [123], eliminates noise due to mechanically moving components but still suffers from weak axial confinement. Novel hybrid optical and magnetic transport schemes have also been developed [124, 125].

A different approach is to use an optical conveyor-belt scheme, where a moving lattice is used to transport the atoms [126–130]. Here, the use of an optical lattice eliminates the problem of weak axial confinement. By introducing a frequency difference $\Delta f$ the lattice is translated at speed $v = \lambda\Delta f/2$, where $\lambda$ is the wavelength, along the propagation direction of the beam with the greater frequency. Dynamically changing the detuning between the lattice beams allows the translation of the lattice sites to transport the ultracold sample. Typically transport over 30cm can be achieved in less than 50ms, and the initial axial extent of the cloud is preserved by the lattice.

## 1.3 A Quantum Gas Microscope of Molecules

Our apparatus is designed to create a quantum gas microscope for RbCs molecules. In our case, the objective lens required for single-site imaging sits below a glass "Science Cell". As we are working with multiple species as well as a utilising a quantum gas microscope, ensuring sufficient optical access in the Science Cell is crucial. To that end, atoms are initially prepared in a "MOT chamber" region of the vacuum apparatus, a 12-port stainless steel vacuum chamber. Atoms must therefore be transported 37.2cm to the Science Cell.

The primary focus of this thesis is on $^{133}$Cs and $^{87}$Rb. However, the MOT Chamber is designed to additionally produce samples of Potassium, with the aim of studying K-Cs mixtures. These have the advantage of more favourable scattering properties as well as the choice of either bosonic isotopes in $^{39}$K and $^{41}$K and a fermionic isotope in $^{40}$K [86, 131, 132].

As fast duty cycles are desirable, we employ degenerate Raman sideband cooling in the MOT chamber to produce samples of $^{133}$Cs and $^{87}$Rb atoms with temperatures of a few $\mu$K. Degenerate Raman sideband cooling spin-polarises the atoms into the lowest Zeeman state, $|F=3, m_{\mathrm{F}}=3\rangle$ for $^{133}$Cs and $|F=1, m_{\mathrm{F}}=1\rangle$ for $^{87}$Rb. These states are not magnetically trappable and hence an optical transport scheme must be employed. Once the atoms are transported to the Science Cell, they are to be loaded into a 3D optical lattice used in the quantum gas microscope.

Optical conveyor-belt transport is thus ideal for our needs, with short transport times and comparatively easy spatial mode-matching to the 3D lattice. In this thesis, efficient transport of Cs and Rb over 37.2cm, both separately and simultaneously is demonstrated. It is shown that transport over such a distance is possible using an optical conveyor-belt formed by two Gaussian beams with displaced focuses, aided by magnetic levitation at the start and end of the transport path.

## 1.4 Thesis Overview

The remainder of this thesis is structured as follows:

- *Chapter 2* details calculations of the optical conveyor-belt trapping potential. The lattice beam parameters are optimised under several different circumstances and the results compared.

- *Chapter 3* describes our experimental setup. The techniques used to prepare samples of cold atoms are discussed briefly before the setup of the transport beams is then discussed in detail.

- *Chapter 4* presents characterisation measurements. Different transport trajectories are considered and compared both theoretically and experimentally. Simultaneous dual-species transport is demonstrated, as is the production of a Bose-Einstein condensate of either Cs or Rb.

- *Chapter 5* summarises the key results of the thesis and discusses possible improvements to the transport scheme.

## 1.5 Contributions of the Author

Over the course of my PhD I've had the benefit of working with many other people and had the work of several people to build up from. Simon Cornish my supervisor; fellow PhD students Jonathan Mortlock, Andrew Innes, Apichayaporn (Mew) Ratkata and Adarsh Raghuram and post-docs Sarah Bromley, Phil Gregory, Lewis McArd and Alexandros (Alex) Alampounti.

The microscope lab absorbed an older K-Cs lab which was worked on by Danielle Pizzey, Mew Ratkata, Zhengkun Fu and Elizabeth Bridge. Design work for the microscope experimental setup was done by Ana Rakonjac, Phil Gregory, Vincent Brooks and Lewis McArd.

Optics for cooling atoms in the MOT Chamber were setup by Sarah, Andrew, Mew and Alex. Science Cell imaging was setup by Adarsh and Jonathan. The Science Cell magnetic coils were designed and made by Lewis and put into the experiment by myself and Sarah with help from Jonathan, Andrew and Adarsh.

The optical setup of the fibre amplifiers and their seeds was done by me, Jonathan and Sarah. An original frequency control system for the fibre amplifier seeds was designed by Lewis as well as Andrew Hunter, later being replaced by a commercial unit. Both were implemented into the experiment by Jonathan and Sarah.

The calculations presented were performed by me, with plenty of helpful input especially from Jonathan, Simon and Sarah. Code for the calculation of magnetic fields, was adapted to Python from Matlab code written by Steve Hopkins and Tim Wiles.

The investigation into different transport trajectories was done by me with help from Jonathan and Sarah, particularly for the experimental part. The transport characterisation data was taken by me, again with help from Jonathan and Sarah as well as Adarsh. Production of the Bose-Einstein Condensates was principally undertaken by Jonathan, along side Sarah and help from myself and Adarsh. The data shown in the BEC figure was taken by Jonathan.

## 1.6 List of Publications

Significant parts of this thesis are also presented in :

**Long distance optical conveyor-belt transport of ultracold $^{133}$Cs and $^{87}$Rb atoms**

*Alex J. Matthies*, Jonathan M. Mortlock, Lewis A. McArd, Adarsh P. Raghuram, Andrew D. Innes, Philip D. Gregory, Sarah L. Bromley, Simon L. Cornish (2023). Pre-print

I also contributed to:

**Measurement of the tune-out wavelength for $^{133}$Cs at 880 nm**

Apichayaporn Ratkata, Philip D. Gregory, Andrew D. Innes, *Alex J. Matthies*, Lewis A. McArd, Jonathan M. Mortlock, M. S. Safronova, Sarah L. Bromley, and Simon L. Cornish [133] (2021)

# CHAPTER 2

# Transport Calculations

In this chapter detailed calculations of the trapping potential are presented. These are used to find the optimum parameters for the beams that form our optical conveyor-belt. Section 2.1 outlines the trap depth challenge for optical conveyor-belts as well as different approaches taken in previous experiments. In Section 2.2 the transport problem in our experiment is described briefly. Section 2.3 gives an overview of the theoretical basis for the calculations, including optical trapping, 1D optical lattices, the effect of gravity and magnetic levitation. The simplest solution to the transport problem is given in Section 2.4, forming the basis of complete optimisation presented in Section 2.5. Section 2.6 summarises the results of the optimisation and the trap depths achieved. Finally, calculations of the trap frequencies are presented in Section 2.7.

## 2.1 The Background

The main challenge for optical conveyor-belt transport is maintaining sufficient trap depth throughout the whole of the transport path. This is challenging due to the radial divergence of Gaussian beams, leading to reduced trap depth away from the foci of the beams. Unlike optical transport schemes based on a translation stage or a variable-focus lens, the transport beams in an optical conveyor-belt are static and hence the atoms need to be trapped away from their focus. The problem is exacerbated by gravity which “tilts” the trapping potential and thereby reduces the effective trap depth in the vertical direction. It is especially severe for heavy atoms, such as Cs and Rb considered in this work. The trap depth reduction from the gravitation tilt is amplified due to the radial divergence, as the larger the trapping beams are, the greater the trap depth reduction is. Due to the combination of radial divergence and gravitational tilt, the transport distances achievable are typically limited to about one Rayleigh range when using Gaussian beams [126]. The Rayleigh range can be increased by increasing the beam waists, however this comes at the cost of decreased trap depth at the focus. This again is exacerbated by the gravitational tilt.

One solution to the problem of providing sufficient trap depth is to use a Bessel beam [127,128]. Bessel beams, like Gaussian beams, are a solution to the Helmholtz equation with an electric field described by a Bessel function of the first kind [134]. These beams have the key feature of a central spot whose size is independent of position along the beam’s propagation. This makes Bessel beams very attractive for optical conveyor-belt transport as they eliminate the problem of radial divergence. If a Bessel beam is used that has a sufficiently high intensity to trap atoms against gravity, the challenge of having a sufficient trap depth would be overcome

However, a good quality Bessel beam can be hard to create. They are most readily made using a refractive axicon (a conical lens). When illuminated with a Gaussian beam, an axicon creates a Bessel-like beam over a finite region along the beam’s propagation whose size is determined by the size of the incident beam and the apex angle of the tip. An optical conveyor-belt using such a Bessel beam was first successfully implemented by a group in Innsbruck (that later moved to Ulm) for $^{87}$Rb over a transport distance of 20cm in 2006 [127], albeit with some difficulty finding an axicon with a sufficiently high tip quality [134]. More recently, in 2022, a very similar scheme was implemented by a group in Munich to transport $^{133}$Cs over a distance of 43cm [128]. Both experiments make use of a Bessel beam for one of the lattice beams and a Gaussian beam for the other, with the Bessel beam providing the majority of the radial confinement. The size of the central spots of the Bessel beams were $36\mu$m and $\sim 80\mu$m for the Innsbruck and Munich experiments respectively. These small beams would, in principle, mean relatively modest power requirements. However only a small fraction of the power incident onto the axicon is carried by the desired central order, $\sim 5\%$ in Innsbruck [134] and $\sim 10\%$ in the Munich experiment. In both experiments, the power in the central order decreased with distance from the axicon. Hence, 200mW of near-resonant light needed to be used in Innsbruck and 35W of 1064nm light needed to be used in Munich for the Bessel beams to support the atoms against gravity.

Another solution is using both a moving lattice and a variable-focus lens. This solution combines the high axial confinement of the conveyor-belt's lattice with the high radial trap depth achievable for a single beam dipole trap with a moving focus position. Recently, in 2022, this combined method was implemented by a group in Harvard/MIT working with Calcium Monofluoride (CaF) molecules over a transport distance of 46cm [129]. They employ a liquid-based tunable lens to translate the focus position of a narrow $57\mu$m beam, while keeping the other larger $320\mu$m waist beam static. In a similar fashion to the Bessel beams described above, the translated beam provides the majority of the radial confinement. The final position of the molecules is set by the frequency ramp applied to the lattice beams, rather than focus shift due to the tunable lens. Therefore, this scheme retains the ability of a conveyor-belt to precisely select the final molecule position. However, the variable-focus lens' response time places a lower limit on the transport duration. By using a specially designed pulse profile, the group were able to reduce their transport time to 50ms, but observed heavy losses at shorter duration, attributed to non-linear effects in the lens' response. While still fast compared to other transport schemes, it is nonetheless a factor of two slower than the Bessel beam implementation over a similar distance [128].

A third option to solve the trap depth problem is to construct the experimental apparatus such that the transport occurs vertically, turning the conveyor-belt into an "elevator". This essentially eliminates the problem of the gravitational tilt, due to the large axial trap frequencies, typically of order 100kHz. Note that this is true regardless of whether the atoms are transported up or down. Elevator transport was successfully implemented by a group in Ulm (formerly of Innsbruck, the same group that pioneered Bessel beam based transport) to transport Rb atoms over 30cm [65, 135]. Making the transport direction vertical allowed large beams of 500$\mu$m waist to be used, which have the benefit of a long Rayleigh range, without incurring large trap depth reductions due to gravity. However due to the many other constrains placed on cold atom experiments vertical transport is often unfeasible, as is unfortunately the case for our experiment.

The final and simplest approach was taken in a recent paper from a group in Chicago [130]: use enough laser power. They transport Cs atoms over 28cm using a 40W laser. The optical conveyor-belt is formed by retro-reflecting beam which increases the amount of power on the atoms, compared to splitting the light as done in [126]. However, the transport efficiencies are comparatively low, at $20-30\%$, and transport times are comparatively long, at 400ms. This may be due to the more complex frequency control setup required to implement the retro-reflected lattice.

## 2.2 The Problem

The transport problem for our experiment is illustrated in Figure 2.1. Atoms are initially cooled in the MOT Chamber and need to be transported to the Science Cell for future experiments, which is situated 37.2cm from the centre of the MOT Chamber.

We are able to avoid using either a Bessel beam or a variable-focus lens and instead implement optical conveyor-belt transport using two Gaussian beams. It is possible to provide sufficient trap depth throughout the transport path with two Gaussian beams by offsetting the two focus positions and carefully selecting the beam waists and focus offsets. Additionally, the atoms are magnetically levitated at either end of the transport path. In the remainder of this chapter, in-depth calculations of the trap depth are presented. These calculations enabled an optical conveyor-belt transport to be implemented for $^{133}$Cs and $^{87}$Rb, hereafter referred

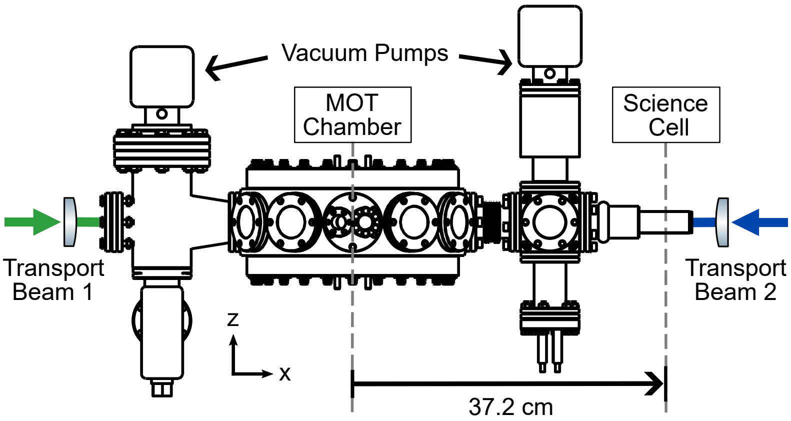

Figure 2.1: Schematic of the vacuum apparatus and overview of the transport problem. Transport is performed between the "MOT Chamber" where the atoms are initially cooled and the "Science Cell" where future experiments will be performed. The transport problem is transferring atoms across the 37.2cm gap between these two regions of the vacuum system.

to as Cs and Rb respectively. Calculations are also presented for $^{41}$K (hereafter referred to as K), in order to ensure the transport scheme will enable K-Cs mixture experiments to be performed in the future.

## 2.3 The Ingredients

### 2.3.1 Optical dipole traps

Optical dipole traps, as their name suggests, are based on the dipole force exerted on atoms by laser light. In a semi-classical model, the electric field of the light induces an atomic dipole moment in the atoms. This induced dipole then interacts with the same electric field, giving an interaction potential [136]

$$U_{\mathrm{dip}} = -\frac{\alpha_\lambda}{2\epsilon_0 c} I \tag{2.1}$$

where $U_{\mathrm{dip}}$ is the dipole potential, $I$ is the intensity of the applied field and $\alpha_\lambda$ is the real part of the atomic polarisability. The subscript $\lambda$ indicates that the polarisability is dependent on the wavelength of the laser field. For convenience, we define $\mathcal{A}$

$$U_{\text{dip}} = -\mathcal{A} I \tag{2.2}$$

such that it is the proportionality constant between the optical potential and the intensity of the laser field.

The general form of the polarisability contains scalar, vector and tensor components. For linearly polarised light the vector component is zero. For a ground-state alkali atom the tensor component is less than one part per million, and not relevant for these calculations. The tensor component is relevant for high precision measurements, e.g. of the tune-out wavelength [133, 137], but for the purpose of transport calculations it is negligible. Thus the polarisability can be simplified to just the scalar component. Complete treatments of the atomic polarisability can be found in e.g. [138, 139].

In a simplified semi-classical model of a two level atom interacting with a classical field, the polarisability can be given by [136]

$$\alpha_\lambda = \frac{3\pi c^3 \epsilon_0}{{\omega_0}^3}\left(\frac{\Gamma}{\omega_0 - \omega} - \frac{\Gamma}{\omega_0 + \omega}\right), \tag{2.3}$$

where $\omega_0$ is the (angular) transition frequency, $\omega$ is the angular frequency of the laser field and $\Gamma$ is the spontaneous decay rate of the excited state. For alkali atoms in the ground state, the dominant contributions to the scalar polarisability are from the $\text{D}_1$ and $\text{D}_2$ lines. As an approximation, the weighted average of the D-line contributions can be used.

For this work however the polarisability values calculated in [140] are used. For an alkali atom in the ground state $ns$, where $n$ is the principle quantum number, the polarisability, in atomic units, is given by

$$\begin{aligned}\alpha^{ns} = \alpha_{\text{core}} + \alpha_{vc} + \frac{1}{3}\sum_{n'}\Bigg(&\frac{\delta E_{n'p_{1/2}} \langle n'p_{1/2}||D||ns\rangle^2}{\delta E^2_{n'p_{1/2}} - \omega^2} \\ &+ \frac{\delta E_{n'p_{3/2}} \langle n'p_{3/2}||D||ns\rangle^2}{\delta E^2_{n'p_{3/2}} - \omega^2}\Bigg).\end{aligned} \tag{2.4}$$

Here $\alpha_{\text{core}}$ and $\alpha_{vc}$ are constants due to the core electrons and a core modification

| Species | $\alpha^{ns}$ $(4\pi\epsilon_0 {a_0}^3)$ [140] | $\mathcal{A}$ $(m^2 s)$ |
|---|---|---|
| K | 597.5(1.2) | $1.856(4) \times 10^{-36}$ |
| Rb | 686.9(9) | $2.132(3) \times 10^{-36}$ |
| Cs | 1162.1(1.9) | $3.609(6) \times 10^{-36}$ |

Table 2.1: Table of polarizabilities for K, Rb and Cs at 1064nm. The polarizabilities are given in terms of atomic units and $\mathcal{A}$ is given in SI units such that it converts an intensity in Watts per meter squared $(Wm^{-2})$ into a potential in Joules $(J)$.

due to the valence electron respectively, the sum is over contributions from excited states $p_{1/2}$ and $p_{3/2}$ with principle quantum numbers $n'$, $\langle n'p||D||ns\rangle$ is the reduced electric-dipole matrix element between excited state $|n'p\rangle$ and ground state $|ns\rangle$ and $\delta E_{n'p}$ is the energy difference between the states $\delta E_{n'p} = E_{n'p} - E_{ns}$. Table 2.1 gives the polarisability values for K, Rb and Cs used for the transport calculations, as given in [140] at 1064nm. The corresponding values of $\mathcal{A}$ are also given in units of $m^2 s$, which are convenient for the calculations as they convert an intensity in Watts per meter squared $(Wm^{-2})$ into a potential in Joules $(J)$. Data for the transitions can be found in [141] for K, in [142] for Rb and in [143] for Cs.

### 2.3.2 Gaussian Beams

A Gaussian beam propagating along the $x$ axis has an electric field given by

$$E_{\text{Gauß}}(\rho, x) = E_0 \frac{w_0}{w(x)} \exp\left[-\frac{\rho^2}{w(x)^2}\right] \exp\left[ikx - i\omega t + ik\frac{\rho^2}{2R(x)} - i\varphi(x)\right] \tag{2.5}$$

where $\rho$ is the radial coordinate, $E_0$ is the field amplitude, $k$ is the wavevector, $\omega$ is the angular frequency and $w(x)$ is the beam size, $R(x)$ gives the of curvature of the wavefronts and $\varphi(x)$ is the Gouy phase.

The beam size, at position $x$, is defined as the $1/e^2$ radius of the Gaussian profile at that position. At the focus position the beam size is equal to the beam waist $w_0$, $w(x_\text{f}) = w_0$. The wavefront curvature and Gouy phase have been omitted for

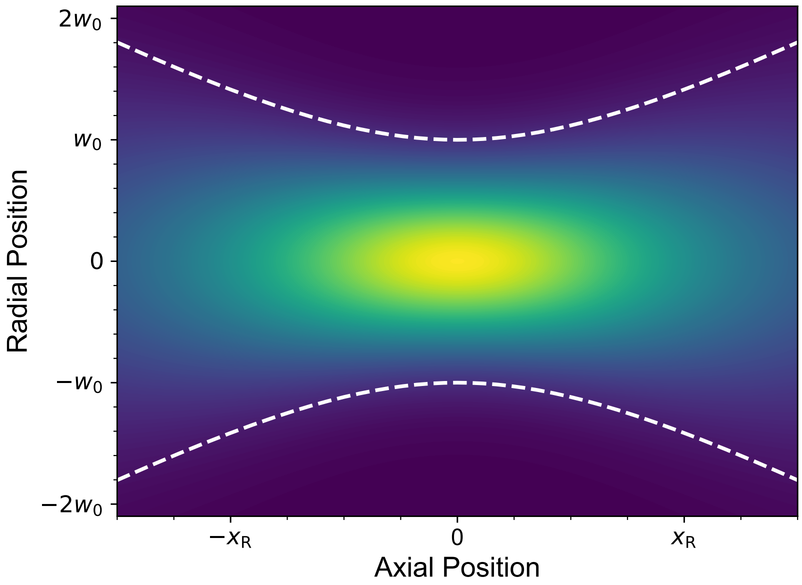

Figure 2.2: Contour plot of the intensity of a Gaussian beam with axial and radial position. White dashed lines show the beam size $w(x)$. The radial and axial length scales are given by the beam waist $w_0$ and Rayleigh range $x_{\mathrm{R}}$ respectively. For transport calculations, the beam waist of interest are of order $100\mu$m, giving Rayleigh ranges of order 10cm.

simplicity. The beam size $w(x)$ varies with the axial position according to

$$w(x) = w_0 \sqrt{1 + \left(\frac{x - x_\mathrm{f}}{x_\mathrm{R}}\right)^2}, \tag{2.6}$$

where $x_\mathrm{f}$ is the focus position and $x_\mathrm{R}$ is the Rayleigh range which in turn is given by

$$x_\mathrm{R} = \frac{\pi {w_0}^2}{\lambda}, \tag{2.7}$$

where $\lambda$ is the wavelength. The curvature of the Gaussian beam's wavefronts is given by $R(x)$ which varies as

$$R(x) = \frac{(x - x_\mathrm{f})^2 + {x_\mathrm{R}}^2}{x - x_\mathrm{f}}. \tag{2.8}$$

At the focus the curvature diverges and the wavefronts become planar. Downstream of the waist (along the direction of propagation) the curvature is positive, meaning the wavefront is furthest advanced on the beam's axis. In other words, the curvature points along the direction of propagation. The reverse is true before the focus position. In analogy with spherical waves in the paraxial approximation, $R(x)$ is frequently referred to as a radius of curvature.

Finally, the Gouy phase is given by

$$\varphi = \arctan\left(\frac{x - x_\mathrm{f}}{x_\mathrm{R}}\right). \tag{2.9}$$

As the name suggests, this is constitutes a phase shift of *pi* which Gaussian beams acquire relative to a plane wave of the same frequency when moving from one side of the focus to the other. Heuristically this can be understood as arising from the finite size of the beam at the focus [144, 145].

For optical trapping we are interested in the intensity of the Gaussian beam. For a single beam the intensity can be found using

$$I_\mathrm{Gauß}(\rho, x) = \frac{c\epsilon_0}{2} \left|E_\mathrm{Gauß}(\rho, x)\right|^2. \tag{2.10}$$

The intensity is thus given by

$$I_{\text{Gauß}}(\rho, x) = I_0 \left( \frac{w_0}{w(x)} \right)^2 \exp\left[ -\frac{2\rho^2}{w(x)^2} \right]. \tag{2.11}$$

where $I_0$ is a constant related to the amplitude of the electric field. Figure 2.2 shows a contour plot of the intensity of a Gaussian beam against axial and radial position. A more practically useful expression for $I_{\text{Gauß}}$ can be found by relating $I_0$ to the total power in the beam, which can be measured much more readily. The total power is given by the integral of Equation 2.11 over its cross-sectional area. Working in cylindrical polar coordinates

$$P = \int_{\rho=0}^{\infty} d\rho \int_{\phi=0}^{2\pi} \rho d\phi \cdot I_{\text{Gauß}}. \tag{2.12}$$

$$P = 2\pi I_0 {w_0}^2 \int_{\rho=0}^{\infty} d\rho \frac{\rho}{w(x)^2} \exp\left( -\frac{2\rho^2}{w(x)^2} \right) \tag{2.13}$$

$$P = 2\pi I_0 {w_0}^2 \cdot \frac{1}{4} \left[ -\exp\left( -\frac{2\rho^2}{w(x)^2} \right) \right]_0^{\infty} \tag{2.14}$$

$$P = \pi I_0 {w_0}^2 \cdot \frac{1}{2} \left[ 1 \right]. \tag{2.15}$$

Hence

$$I_0 = \frac{2P}{\pi {w_0}^2}, \tag{2.16}$$

and Equation 2.11 can be re-written

$$I_{\text{Gauß}}(\rho, x) = \frac{2P}{\pi} \frac{1}{w(x)^2} \exp\left[ -\frac{2\rho^2}{w(x)^2} \right]. \tag{2.17}$$

For convenience, $\mathcal{I}(x)$ is defined to be the peak intensity of the beam at a point $x$ along the beam axis, such that

$$\mathcal{I}(x) = \frac{2P}{\pi} \frac{1}{w(x)^2}. \tag{2.18}$$

Noting that the intensity of a Gaussian does not depend on the travelling wave term, wavefront curvature or Gouy phase, the position dependent amplitude of the electric field can be defined as

$$\mathcal{E}(\rho, x) = E_0 \frac{w_0}{w(x)} \exp\left[-\frac{\rho^2}{w(x)^2}\right], \tag{2.19}$$

such that

$$E_{\text{Gauß}}(\rho, x) = \mathcal{E}(\rho, x) \exp\left[ikx - i\omega t + ik\frac{\rho^2}{2R(x)} - i\varphi(x)\right], \tag{2.20}$$

and

$$I_{\text{Gauß}}(\rho, x) = \frac{c\epsilon_0}{2}\mathcal{E}(\rho, x)^2 \tag{2.21}$$

### 2.3.3 1D Optical Lattices

In this section we will derive a general equation for the intensity of the optical conveyor-belt's 1D lattice, formed from two counter-propagating beams. In general, these two beams may have different beam waists, focus positions and powers. In order to implement transport, a frequency difference needs to be introduced to the beams. Hence the frequency and wavevectors of the two beams are different in general. Initially, the wavefront curvature and Gouy phase terms will be dropped from the derivation, before being considered in more detail at the end of this section. These terms do not cancel, as they do for a single beam trap and do affect the trapping potential. However, as will be shown, they leave all trap depths unchanged and are thus not included in later calculations.

The total intensity is given by

$$I(\rho, x) = \frac{c\epsilon_0}{2}|E_1(\rho, x) + E_2(\rho, x)|^2, \tag{2.22}$$

where, as before, $\rho$ is the radial coordinate (perpendicular to the beams' propagation), $x$ is the axial coordinate (along the beams' propagation) and $E_1$ and $E_2$ are the electric fields from Beam 1 and Beam 2 respectively. These electric fields are given by

$$E_1(\rho, x) = \mathcal{E}_1(\rho, x)e^{ik_1x - i\omega_1 t}, \tag{2.23}$$

$$E_2(\rho, x) = \mathcal{E}_2(\rho, x)e^{-ik_2x-i\omega_2t} \tag{2.24}$$

where $\mathcal{E}_i$ are the real electric field amplitudes (defined in Equation 2.19), $k_\text{i}$ are the wavevectors and $\omega_\text{i}$ are the the angular frequencies. The wavevectors have opposite signs as the beams are propagating in opposite directions. Here we have taken Beam 1 (Beam 2) to be propagating towards $x = +\infty$ ($x = -\infty$). For the sake of brevity we will drop the coordinate dependence of the amplitudes. Substituting into Equation 2.22 thus gives

$$I = \frac{c\epsilon_0}{2}\left(\mathcal{E}_1e^{ik_1x-i\omega_1t} + \mathcal{E}_2e^{-ik_2x-i\omega_2t}\right)\left(\mathcal{E}_1e^{-ik_1x+i\omega_1t} + \mathcal{E}_2e^{ik_2x+i\omega_2t}\right), \tag{2.25}$$

$$I = \frac{c\epsilon_0}{2}\left[{\mathcal{E}_1}^2 + {\mathcal{E}_2}^2 + \mathcal{E}_1\mathcal{E}_2\left(e^{-i(k_1+k_2)x+i(\omega_1-\omega_2)t} + e^{i(k_1+k_2)x-i(\omega_1-\omega_2)t}\right)\right], \tag{2.26}$$

$$I = \frac{c\epsilon_0}{2}\left[{\mathcal{E}_1}^2 + {\mathcal{E}_2}^2 + 2\mathcal{E}_1\mathcal{E}_2\cos\left(2kx - \Delta\omega t\right)\right]. \tag{2.27}$$

Here we define $\Delta\omega$ to be the frequency difference

$$\Delta\omega = \omega_1 - \omega_2, \tag{2.28}$$

and $k$ to be the average wavevector

$$k = \frac{k_1 + k_2}{2}. \tag{2.29}$$

For optical conveyor-belt transport the frequency differences are of order 10MHz, compared to the laser frequency of order 100THz. Thus we can alternatively take the approximation:

$$k_1 + k_2 \sim 2k_1 = 2k. \tag{2.30}$$

Substituting the equation for a single beam's intensity,

$$I_\text{i} = \frac{c\epsilon_0}{2}|E_\text{i}|^2 = \frac{c\epsilon_0}{2}{\mathcal{E}_\text{i}}^2, \tag{2.31}$$

gives

$$I = I_1 + I_2 + 2\sqrt{I_1I_2}\cos\left(2kx - \Delta\omega t\right) \tag{2.32}$$

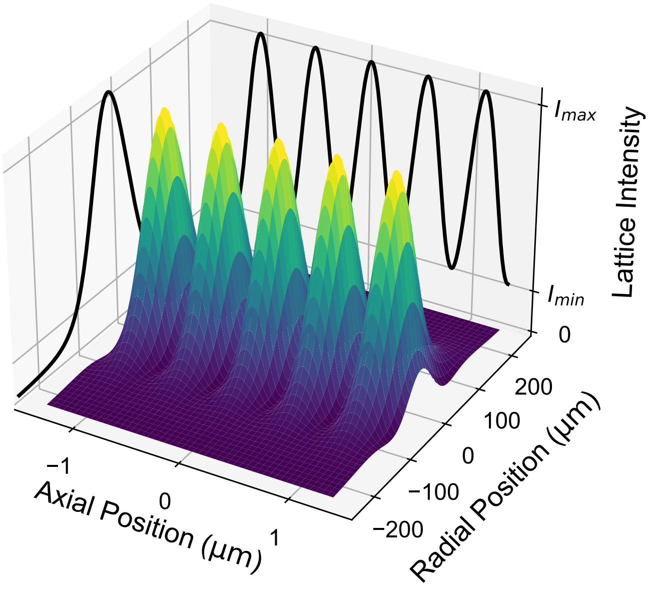

Figure 2.3: Plot of the intensity a 1D lattice along its axial and radial directions. The lattice is formed from two beam of equal powers and focus positions but different waists. Note the difference in the scales between the the axial and radial positions.

which is the general equation for the intensity of a 1D lattice formed by two counter-propagating beams.

### Lattice Velocity

From Equation 2.32 we find the velocity of the lattice to be given by

$$v_{\text{lattice}} = \frac{\Delta\omega}{2k} = \frac{\lambda \Delta f}{2}, \tag{2.33}$$

where $\lambda$ is the wavelength and $\Delta f$ is the frequency difference. For positive $\Delta f$, where $f_1 > f_2$, the lattice moves in the same direction as Beam 1, towards $x = +\infty$.

We can arrive at the same equation using a more heuristic argument. Consider the two counter-propagating beams to have frequencies given by

$$f_1 \quad \text{and} \quad f_2 = f_1 - \Delta f. \tag{2.34}$$

For any frequency difference $\Delta f$ there exists a reference frame, moving at a constant velocity $v$ relative to the lab frame, where the Doppler effect cancels out the frequency difference between the two beams. In that frame a stationary 1D lattice is formed, which is equivalent to a moving lattice of velocity $v$ in the lab frame. This condition is met when

$$\Delta f_{\text{Doppler}} = \frac{\Delta f}{2}. \tag{2.35}$$

The frequency shift from the Doppler effect is given by

$$\Delta f_{\text{Doppler}} = \frac{\Delta v}{c} f_s, \tag{2.36}$$

where $f_s$ is the frequency emitted by the "source" and $\Delta v$ is the velocity difference between the "source" and "receiver". In our case $\Delta v = v_{\text{lattice}}$ and hence, as before,

$$v_{\text{lattice}} = \lambda \Delta f_{\text{Doppler}} = \frac{\lambda \Delta f}{2}. \tag{2.37}$$

The direction the lattice moves in can also be obtained by recalling that moving towards (away from) a source "blue-shifts" ("red-shifts") the received frequency. If $f_2$ is less than $f_1$, the frame in which the two beam's frequencies are equal must be moving towards the source of Beam 2, which is equivalent to moving in the same direction as Beam 1.

### Lattice Potential

For the remaining considerations of the lattice potential, we will omit the time component of Equation 2.32 and work in the moving frame in which the frequency difference between the beams is zero. This is equivalent to the instantaneous rest frame of the transported atoms. In this frame $k_1 = k_2 = k$ and $\omega_1 = \omega_2$.

Axially, the potential varies sinusoidally between the a minimum and maximum intensity given by

$$I_{\text{min}} = I_1 + I_2 - 2\sqrt{I_1 I_2} \tag{2.38}$$

and

$$I_{\text{max}} = I_1 + I_2 + 2\sqrt{I_1 I_2}. \tag{2.39}$$

We can thus define the amplitude of the sinusoid to be

$$I_{\text{lattice}} = I_{\max} - I_{\min} = 4\sqrt{I_1 I_2}. \tag{2.40}$$

Using

$$\cos(2\theta) = 2\cos^2(\theta) - 1, \tag{2.41}$$

the lattice potential can then be written as

$$I = I_{\min} + I_{\text{lattice}} \cos^2(kx). \tag{2.42}$$

In the limiting case of equal beams $I_1 = I_2 = I_0$, this reduces to the familiar

$$I = 4\ I_0 \cos^2(kx). \tag{2.43}$$

A contour plot of the lattice intensity is shown in Figure 2.3 for two Gaussian beams. Axially, the sinusoidal variation between $I_{\min}$ and $I_{\max}$ is evident. Radially, the potential follows the familiar Gaussian profile with a peak intensity of $I_{\max}$.

### Potential Depths

From the equations for the 1D lattice potential, we can determine the trap depths. As already suggested by Figure 2.3, the trap depths can be split into an axial depth along the beams' propagation direction and a radial depth from the Gaussian beam profile. Plots of the trap potential along the axial and radial directions are shown in Figure 2.4, with the radial direction split into the horizontal direction without gravity and the vertical direction with gravity.

Axially the trap depth is taken to be the sinusoidal part of the potential. At a given point along the transport path it is given by

$$\mathcal{U}_{\text{axial}}(x) = \mathcal{A} I_{\text{lattice}}(\rho = 0, x) = 4\mathcal{A}\sqrt{\mathcal{I}_1(x)\mathcal{I}_2(x)}. \tag{2.44}$$

Here we use $\mathcal{U}$ to denote a trap *depth* to distinguish it from $U$, the trap *potential.* As before in Equation 2.18, $\mathcal{I}_{\text{i}}(x)$ is the maximum intensity of Beam i at axial position

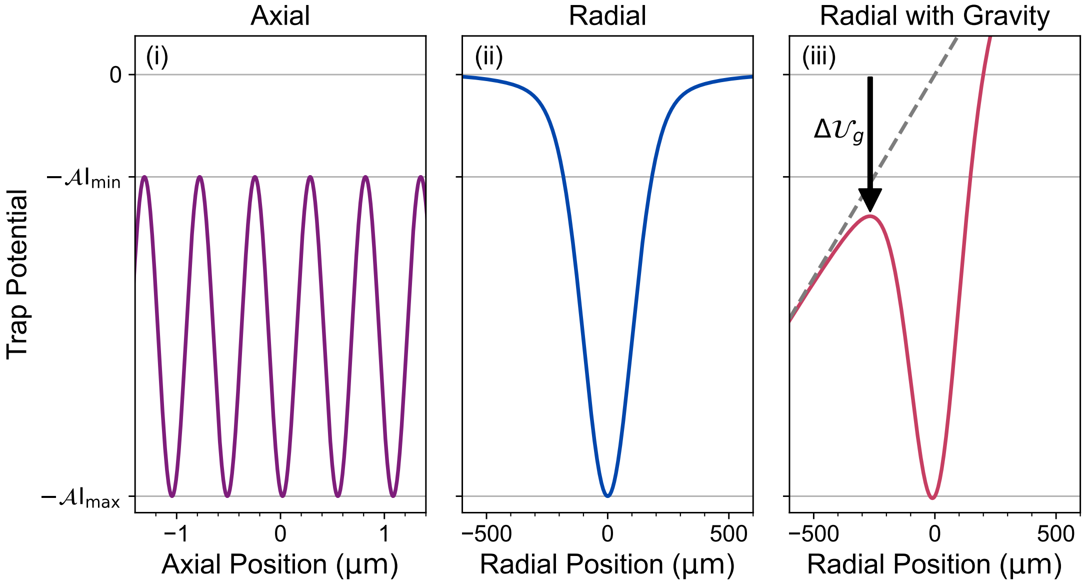

Figure 2.4: Origin of 1D lattice trap depths. (i) Axially, along the axis of the beams' propagation, the potential varies sinusoidally and trap depth is taken to be the amplitude. (ii) Radially, the trap follows the typical Gaussian shape and the trap depth is given by the peak intensity. (iii) Gravity adds an additional potential term and "tilts" the potential thereby reducing trap depth by $\Delta\mathcal{U}_\mathrm{g}$ as shown.

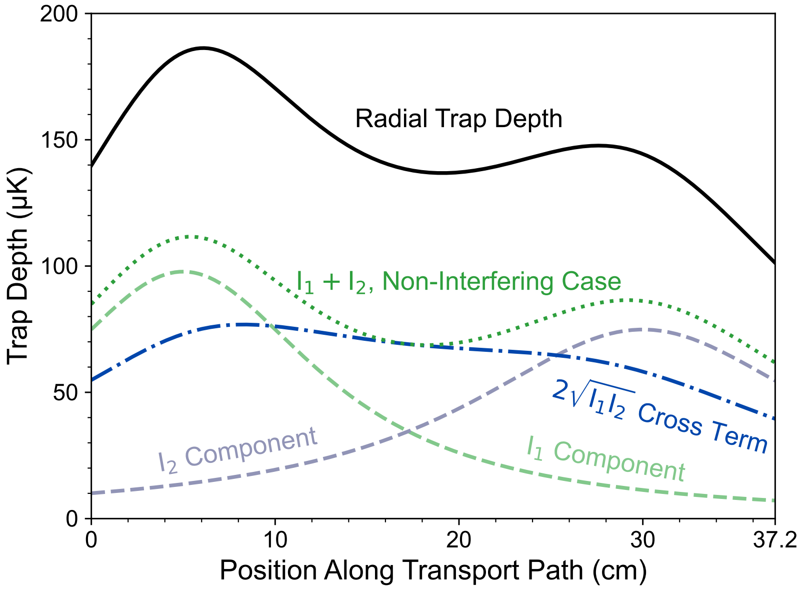

Figure 2.5: Components contributing to the radial trap depth (excluding gravity) for Cs in a 1D lattice. In this example beam 1 (2) has a waist of 175$\mu$m (200$\mu$m) and a focus position of 5cm (30cm) along the transport path. Both beams have 18W of power. The contribution from Beam 1 (Beam 2) is shown by the dashed light green (blue-grey) line and the interference cross term by the dash-dotted blue line. The sum of those three components give the radial trap depth, shown by the black solid line. The non-interfering case is shown for comparison by the dotted green line.

$x$. The axial depth is given only by the sinusoidal part and not the additional $I_{\text{min}}$ term. Any atoms trapped only by this term and not by the lattice can not be accelerated or decelerated by the lattice and hence are considered lost.

Radially, perpendicular to the direction of beam propagation, the optical potential has the typical Gaussian shape. As the lattice uses far red-detuned light, the optical potential is attractive and the atoms are trapped at the anti-nodes of the lattice. In the limit of large radial distances $\rho \to \pm\infty$, the optical potential goes to zero. Hence the trap depth at a given point along the transport path is given by the value of $I_{\text{max}}$ at that point[1]

$$\mathcal{U}_{\text{radial}}(x) = \mathcal{A} I_{\text{max}}(\rho = 0, x) = \mathcal{A}\left(\mathcal{I}_1(x) + \mathcal{I}_2(x) + 2\sqrt{\mathcal{I}_1(x)\mathcal{I}_2(x)}\right). \tag{2.45}$$

However, due to the effect of gravity the radial trap depths are separated into the horizontal and vertical directions. Horizontally, the trap is purely Gaussian with a depth given by Eq. 2.45. Vertically there is an additional gravitational term $mgz$ which “tilts” the potential, lowering the trap depth. There is no straightforward analytic expression for the reduction in trap depth so the vertical trap depth is found by calculating the potential along the $z$ axis at each point along the transport path and numerically finding the difference between the local maximum and local minimum in the trap potential. The effect of gravity is considered further in Section 2.3.4.

For any position $x$ along the transport path, the beam size can be calculated for each beam using Equation 2.6. Then, using Equation 2.18, the beams' peak intensity can be calculated and hence the axial and radial trap depths found using Equation 2.44 and Equation 2.45 respectively. A plot of the radial depth throughout the transport paths is shown in Figure 2.5, for two 18W beams of waists 175$\mu$m and 200$\mu$m and focus positions 5cm and 30cm along the transport path. The figure also shows the contribution to the trap depth from each of the three terms in

---

[1] Strictly speaking the radial trap depth is only a meaningful quantity at $x$ values where there exists an anti-node. However we can treat the radial depth as a continuous quantity that gives the trap depth at any point $x$ at the *instantaneous point in time, during a transport ramp, at which an anti-node is located at that point.*

Equation 2.45: $\mathcal{I}_1$ by the green dashed line, $\mathcal{I}_2$ in the blue-grey dashed line and the interference cross term in the blue dash-dotted line. The non-interfering case is also shown for comparison in the light green dotted line. The efficacy of separating the focus positions of the two beams can clearly be seen in the figure. The majority of the radial trap depth is provided by the $\mathcal{I}_1$ at the start of the transport path, by $\mathcal{I}_2$ at the end of the transport path and by the cross term in the middle. As will be shown in later sections, this separation of beams enables much greater trap depths to be achieved.

### Effect of Wavefront Curvature and Gouy Phase

Relaxing the previous simplification and including both the wavefront curvature and Gouy phase terms into the electric field equations gives

$$E_1(\rho, x) = \mathcal{E}_1(\rho, x) \exp\left[+ik_1 x - i\omega_1 t + ik_1 \frac{\rho^2}{2R_1(x)} - i\varphi_1(x)\right], \tag{2.46}$$

and

$$E_2(\rho, x) = \mathcal{E}_2(\rho, x) \exp\left[-ik_2 x - i\omega_2 t - ik_2 \frac{\rho^2}{2R_2(x)} - i\varphi_2(x)\right], \tag{2.47}$$

for the electric field of the two beams. The wavefront curvature of the two beams are given by

$$R_1(x) = \frac{(x - x_{\mathrm{f},1})^2 + {x_{\mathrm{R},1}}^2}{x - x_{\mathrm{f},1}}, \tag{2.48}$$

$$R_2(x) = \frac{(x - x_{\mathrm{f},2})^2 + {x_{\mathrm{R},2}}^2}{x - x_{\mathrm{f},2}}, \tag{2.49}$$

and the Gouy phase terms given by

$$\varphi_1(x) = \arctan\left(\frac{x - x_{\mathrm{f},1}}{x_{\mathrm{R},1}}\right). \tag{2.50}$$

$$\varphi_2(x) = -\arctan\left(\frac{x - x_{\mathrm{f},2}}{x_{\mathrm{R},2}}\right), \tag{2.51}$$

where $x_{\mathrm{f,i}}$ and $x_{\mathrm{R,i}}$ are the focus position and Rayleigh range of Beam i respectively.

The curvature terms are defined such that a positive curvature means that the wavefronts point along the $x$-axis for both beams. Hence the equations for $R_1(x)$ and $R_2(x)$ have the same sign. Beam 1 has a positive curvature downstream (after) of its focus, while Beam 2 has a positive focus upstream (before) its focus. This difference is reflected in the opposite sign in the exponent in the equations for $E_1(\rho, x)$ and $E_2(\rho, x)$. The variation of the radius of curvature of the two beams is shown in Figure 2.7(a) for beams of waist 195$\mu$m that are focussed 7.2cm from each end of the transport path.

The Gouy phase terms are defined such that the phase shift in negative upstream (before) of each beam's focus and positive downstream (after) the beams focus. The equations for $\varphi_1(x)$ and $\varphi_2(x)$ thus differ by a minus sign. Figure 2.6(a) shows the variation of the Gouy phase for both beams along the transport path. As before, beam waist of 195$\mu$m and focus positions 7.2$cm$ from the transport path ends are used.

Following the derivation in Section 2.3.3, the lattice intensity is then given by

$$I = I_1 + I_2 + 2\sqrt{I_1 I_2} \cos\left[2kx - \Delta\omega t + \frac{k_1\rho^2}{2R_1(x)} + \frac{k_2\rho^2}{2R_2(x)} + \Delta\varphi\right], \tag{2.52}$$

where $\Delta\varphi = \varphi_1 - \varphi_2$ is the Gouy phase difference and other terms are defined as before. In the rest frame of the lattice, where $\omega_1 = \omega_2$ and $k_1 = k_2 = k$, this simplifies to

$$I = I_1 + I_2 + 2\sqrt{I_1 I_2} \cos\left[2kx + \frac{k\rho^2}{2}\left(\frac{1}{R_1(x)} + \frac{1}{R_2(x)}\right) + \Delta\varphi\right]. \tag{2.53}$$

As can be expected, the wavefront curvature and Gouy phase terms cancel out in intensity terms from each beam individually and only appear in the interference term.

The Gouy phase term is shifts the location of the intensity maxima and minima equal to the difference in the two phase terms. The size of the shift varies along the transport path as shown in Figure 2.6, with panels (b) showing the unshifted potential and panels (c) showing the contours with the Gouy phase included. As the beams are symmetric around the centre of the transport path, both beams have an equal Gouy phase shift at the centre and therefore the potential is unaffected.

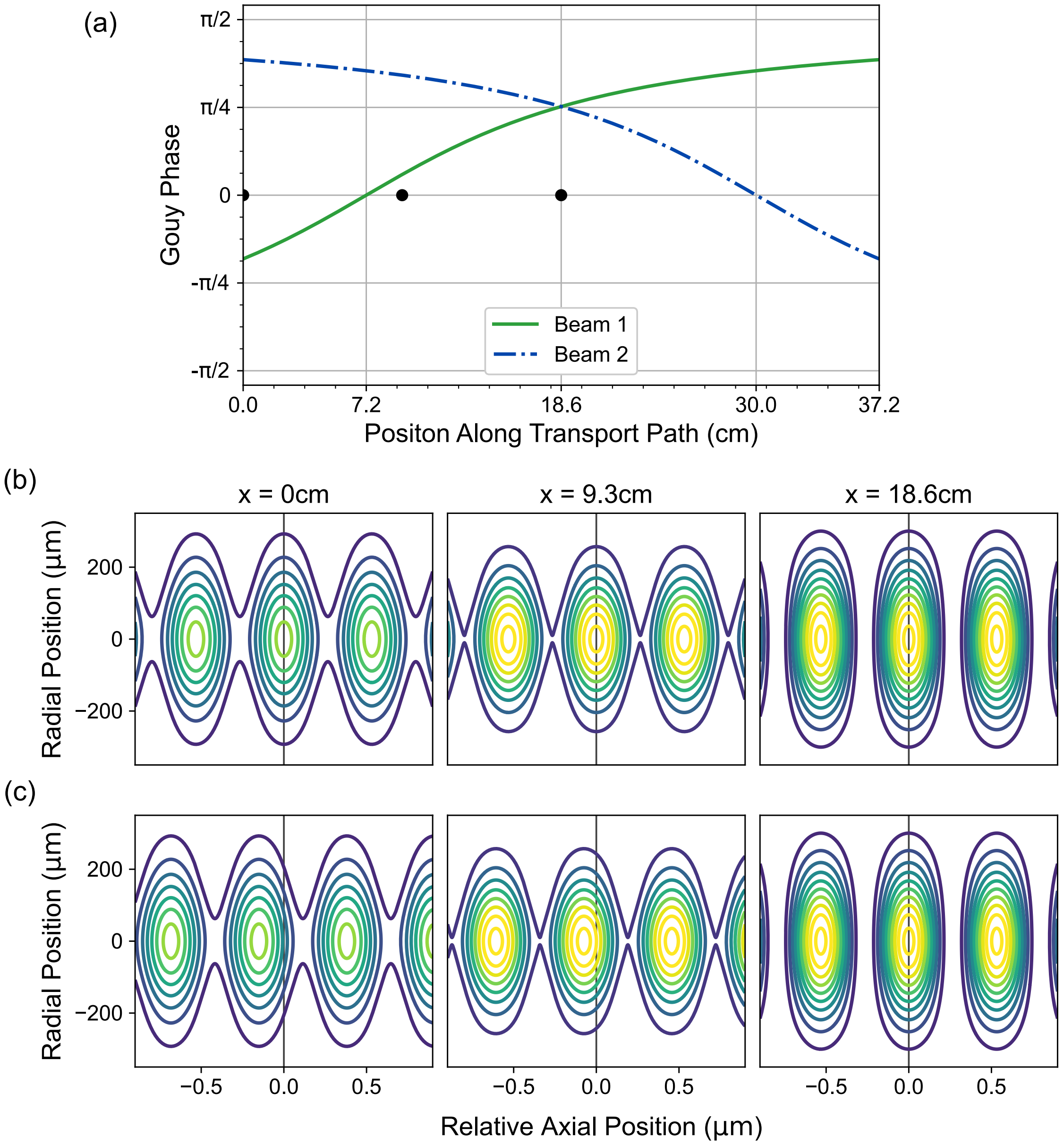

Figure 2.6: Effect of the Gouy phase term of Gaussian beam on the trapping potential of a 1D lattice. (a) Shows how the Gouy phase of the transport beams varies along the transport path. The beams have a waist of 195$\mu$m and are focussed 7.2cm from each end of the transport path, see Section 2.5.3. Contour plots of the lattice potential at three different points along the transport path are shown in (b) and (c), their positions are indicated by black dots in (a). All contours share the same scale. (b) Shows the potential for Gaussian beams, without the Gouy phase. (c) Shows the potential at the same points, including the Gouy phase which shifts the location of the intensity maxima and minima according the the *difference* of the two phase terms.

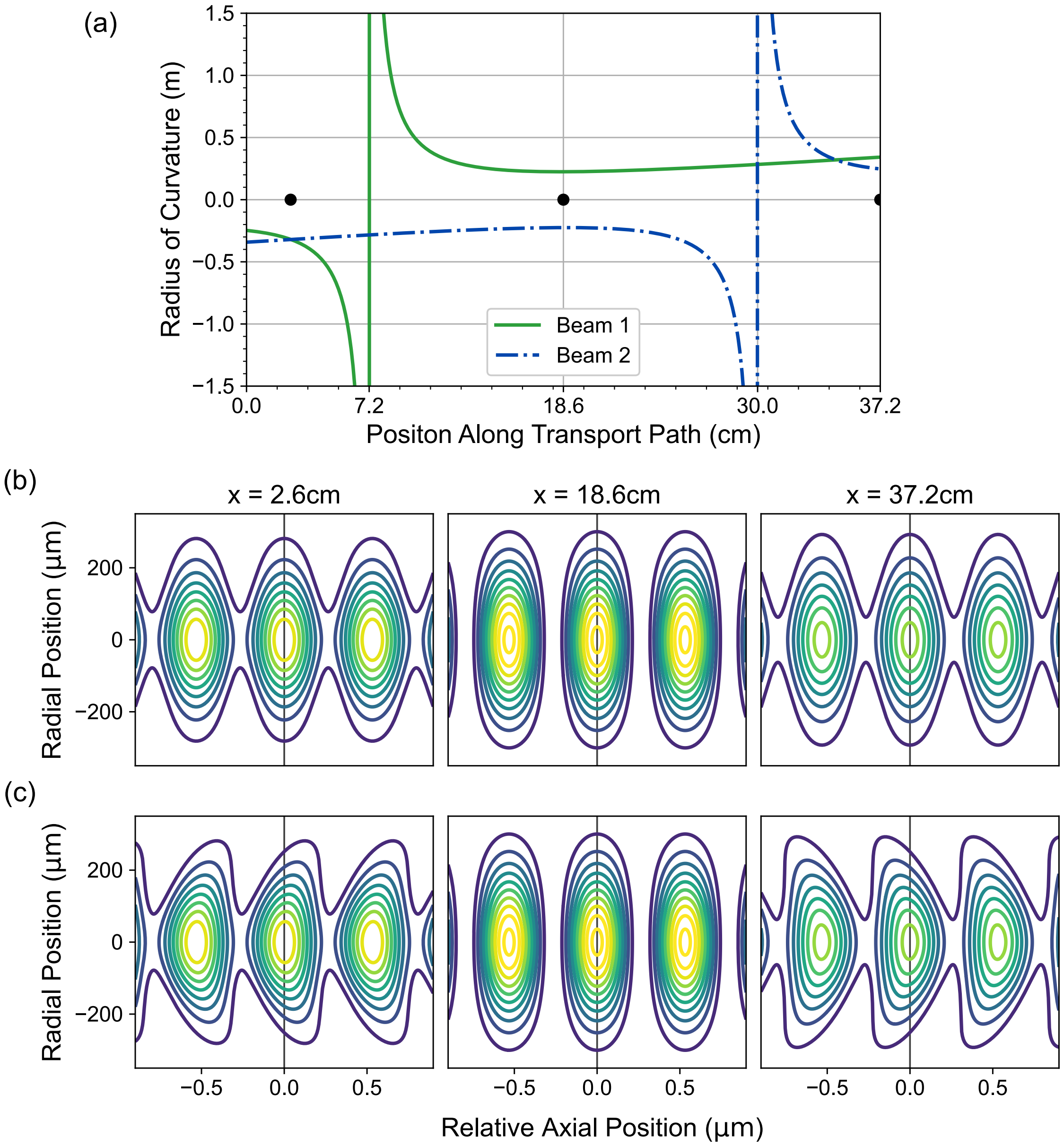

Figure 2.7: Effect of the wavefront curvature term of Gaussian beam on the trapping potential of a 1D lattice. (a) Shows how the radius of curvature of the transport beams varies along the transport path. The beams have a waist of 195$\mu$m and are focussed 7.2cm from each end of the transport path, see Section 2.5.3. Contour plots of the lattice potential at three different points along the transport path are shown in (b) and (c), their positions are indicated by black dots in (a). All contours share the same scale. (b) Shows the potential for Gaussian beams, neglecting the Wavefront curvature term. (c) Shows the potential at the same points, including the wavefront curvature which curves the potential according to the *sum* of the two curvature terms.

The largest shifts occur the edges of the transport path, where the phase difference is just over $\pi/2$ for the beam shapes used. The shift increases smoothly going from the centre of the transport path to either edge. As the cloud of atoms that are being transported have an axial extent of the order of $100\mu$m, the shift in lattice position is negligible for conveyor-belt transport. There is also, in principle, a small effect on the axial trap frequency. This is due to a "missing" lattice maxima and minima from the accumulated phase throughout the transport path. However, as there are just under $7 \times 10^5$ of each intensity extrema in the transport path, this difference is also negligible.

The effect of the wavefront curvature terms is somewhat more subtle. They are proportional to $\rho^2$, hence the leave the potential on the axis of the transport path unchanged, which is defined by $\rho = 0$. This means that the axial trap depth is entirely unaffected. It also means that the wavefront curvature does not affect the maximum intensity of the lattice $I_{\max}(\rho = 0, x)$ , which always occurs on the axis of the transport beams. The wavefront curvature terms do however change the radial shape of the traps, with the size of the distortion given by the sum of the wavefront curvature terms. This change is shown in Figure 2.7 for three different points along the transport path. The panels in (b) show the potential when the wavefront terms are neglected, whereas panels in (c) include them. At the centre of the transport path, $x = 18.6$cm, the wavefront curvatures of the two beams have an equal magnitude but an opposite sign. The contributions thus cancel and the potential remains unaffected. Meanwhile, at $x = 2.6$cm (and at $x = 34.6$cm) the wavefront curvature terms have the same magnitude and sign and the potentials noticeably affected.

The fact that the wavefront curvature does not affect the potential at the centre of the transport axis may seem counter-intuitive at first but can be understood with a simplistic model. Consider two wavefronts of equal and opposite curvature travelling towards each other. Each point (or more precisely pair of points) along the wavefront will intersect with the other wavefront at a different time, but the location of that intersection will be a straight line orthogonal to the direction of the wavefronts' propagation. On the other hand, consider two wavefronts of curvature of equal size and direction. Each point will intersect the other wavefront at the same point in time, but the line describing the intersection will now be a curve. These intersection lines in the simplified picture are equivalent to lines of constant phase for the real lattice.

Despite the curvature of the potential, the radial trap depths remain unaffected. The horizontal trap depth is given only by the maximum intensity of the lattice and hence is unchanged by the addition of the wavefront curvature. The vertical trap depth is dependent on the shape of the trap due to the gravitational tilt, as discussed in Section 2.3.4. If the vertical trap depth were to be found by taking a vertical slice of the potential, the wavefront curvature would appear to lead to a tighter trap and hence larger trap depth due to the gravitational tilt[2]. However, this is only an artefact. Rather than a straight line, the potential needs to be considered along the curved line of constant phase of the lattice as this represents the easiest escape path for the atoms. Along these lines the trap shape and hence the trap depth are unaffected when plotted against radial position.

Alternatively the effect of the wavefront curvature can be seen as a distortion of the *axial* shape of the trap, with the distortion dependent on the radial coordinate). However, as gravity and the Gaussian intensity drop-off depend only on the radial coordinate, the trap depth is unaffected by this distortion.

Therefore, as both the Gouy phase and the wavefront curvature do not affect the trap depths, they are neglected in future calculations in the interest of simplicity.

### 2.3.4 Gravitational Tilt

Gravity contributes a linear term $mgz$ to the trap potential, giving a different radial trap depth in the horizontal and radial directions. As already seen in Figure 2.4, this has the effect of reducing the trap depth. The vertical trap depth is defined as the difference between the local minimum at the centre of the trap and the local maximum formed due to the gravitational potential term.

Vertical trapping potentials for K, Rb and Cs are shown in Figure 2.8. The

---

[2] It is worth noting that even taking this more, let's say, "optimistic" definition of the vertical trap depth, the trap depth would only be increased by a maximum of around 2%.

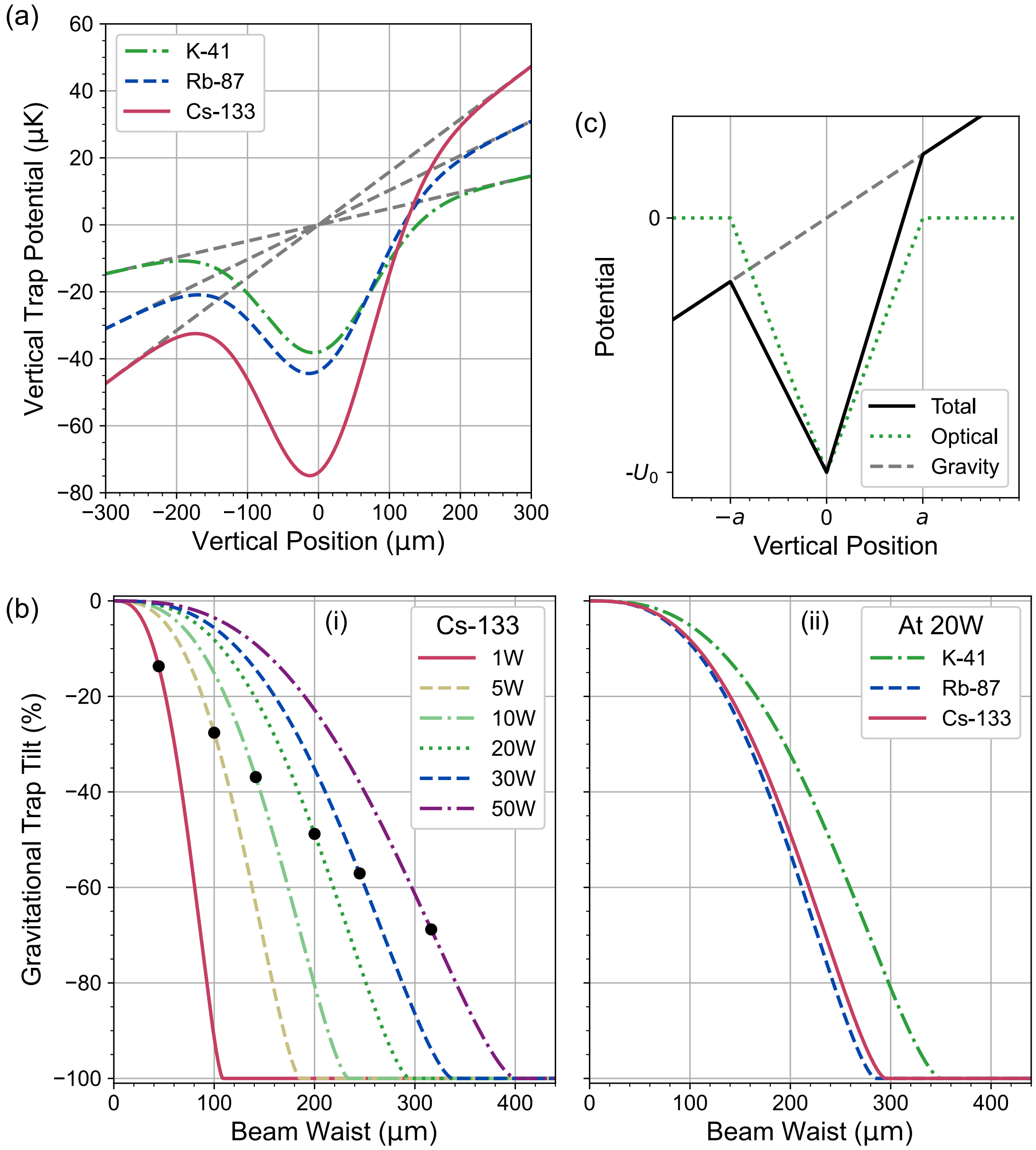

Figure 2.8: Effect of gravity on the trapping potential. (a) Trap potential along the vertical direction with gravity. Cs is shown with the solid red line, Rb with the dashed blue line and K with the dash-dotted green line. The gravitational potential terms are shown with the grey dashed lines. (b) Variation in vertical trap depth drop with beam size. (i) The percentage drop in trap depth due to gravity is plotted against the beam waist for different powers for Cs. The black dots indicate the beam waist for each value of power that gives the same trap depth. (ii) effect of varying the beam waist for the three different species is shown at a power of 20W. (c) Simplified model to explain the dependence on beam waist. The optical trap uses a triangular beam shape. See main text for details.

optical potential is calculated for a single 1064nm beam with a waist of 150$\mu$m and 10W of power. The larger polarisability of Cs as compared to K and Rb is evident from the deeper trap minimum, and the same is true for Rb compared to K. As is obvious from the equation for the gravitational term, the gravitational tilt is more severe for heavy atoms such as Cs and Rb.

The severity of the gravitational tilt is strongly dependent on the size of the trap vertically, as shown in Figure 2.8(b). The plots show the percentage drop in vertical trap depth as a function of the beam waist. The left plot shows the trap depth drop for different beam powers for Cs with a sharp drop-off evident for all powers. The right plot shows the decrease in trap depth at 20W for the three different species over the same beam waist range.

The reason for the increased trap depth decrease can be understood by considering the simplified model shown in Figure 2.8(c). The model uses a triangular beam shape for the optical trap with a vertical extent of $2a$ and depth $U_0$, shown in the dotted green line. As for the Gaussian trap, the gravitational term (light green dashed line) tilts the trap as shown by the solid black line. In this case however the drop in trap depth due to gravity is easily described analytically, namely $\Delta\mathcal{U}_{\mathrm{g}} = mga$. Thus the dependence of the trap depth drop on the size of the trap becomes clear. In triangular beam shape model this is valid provided

$$a < \frac{U_0}{mg}, \tag{2.54}$$

above which the local maximum and minimum no longer exist and no trap is formed.

The same argument also applies to Gaussian beams. The local maximum in the trap potential occurs at some distance $a_{\mathrm{Gauß}}$ from the central local minimum and the decrease in trap depth due to gravity is equal to $\Delta\mathcal{U}_{\mathrm{g}} = mga_{\mathrm{Gauß}}$. The larger the beam size, the further away the local maximum occurs and hence the larger $a_{\mathrm{Gauß}}$ and the decrease in trap depth are. For Gaussian beams, the relationship between the beam waist and the location of the local maximum in the potential is more complicated. This leads to the shape of the curves in Figure 2.8(b).

This dependence of the gravitational trap depth drop on the beam size exacerbates the challenge of providing sufficient trap depth to the atoms posed by the beam divergence and by gravity. It also demonstrates why vertical optical "elevators" eliminate the issue of gravitational tilting. For an elevator, the size of the trap is given by the wavelength of the light $\lambda/2 = 532$nm and thus the trap depth drop due to gravity is negligible.

### 2.3.5 Magnetic Levitation

The effect of the gravitational tilt can be reduced using a magnetic gradient field. Due to the Zeeman effect, a magnetic field will add a further term to the potential given by

$$U_{\mathrm{B}} = -\boldsymbol{\mu} \cdot \mathbf{B} \tag{2.55}$$

where $\mathbf{B}$ is the magnetic field and $\boldsymbol{\mu}$ is the atom's magnetic moment. For Cs and Rb, we work in the weak field limit, where the Zeeman shift is small compared to the hyperfine splitting, wherein the potential term can be written [15]

$$U_{\mathrm{B}} = g_{\mathrm{F}} \mu_{\mathrm{B}} m_{\mathrm{F}} B \tag{2.56}$$

where $g_{\mathrm{F}}$ is the Landé $g$-factor, $\mu_{\mathrm{B}}$ is the Bohr Magneton, $m_{\mathrm{F}}$ is the projection of the total angular momentum onto the quantisation axis and $B = |\mathbf{B}|$ is the magnitude of the magnetic field. The magnitude of the magnetic field is used as the magnetic moment of the atoms aligns to the direction of the magnetic field [15]. This is due to magnetic field providing the quantisation axis for the atoms.

By engineering a field that varies linearly in the vertical direction

$$B = \frac{dB}{dz} z = B' z \tag{2.57}$$

the effect of gravity can be counteracted, thereby "magnetically levitating" the atoms. The magnitude of the gradient field required to fully levitate the atoms is given by

$$B'_{\mathrm{lev}} = \frac{mg}{|g_{\mathrm{f}}| \mu_{\mathrm{B}} m_{\mathrm{F}}}. \tag{2.58}$$

### Magnetic Coils

Quadrupole coils are well suited for magnetic levitation and consist of a pair of coils of equal radius $R$ and separation $s$ that have an equal current $I$ flowing through them in opposite directions. This is known as the anti-Helmholtz configuration. This produces a magnetic field zero at the centre of the coils, which we will take to be at $z = 0$. For small distances around the centre of the coils, the gradient is linear and hence the coil are able to levitate the atoms.

However there is some subtly due to field zero at the centre of the coils. Above the zero, the field points in the positive $z$-direction and increases in magnitude. Below the zero the field similarly increases in magnitude but points in the negative $z$-direction. As the direction of magnetic field sets the quantisation axis of the atoms, the quantisation axis will similarly undergo a sign change. To understand why this is an issue, consider a cloud of atoms in a high-field seeking state at the centre of a quadrupole coil pair. Any atoms situated above the field zero would have their quantisation axis aligned with the $z$-axis and see an increasing (positive) field with $z$. They would thus experience an "upwards" force to counteract gravity, as desired. Any atoms situated below the field zero would have their quantisation axis anti-aligned with $z$-axis. Hence they too would see an increasing (positive) magnetic field *along their quantisation axis* and experience a force in that direction. However, this force is now in the *same* direction as gravity due to change in the quantisation axis' direction. Instead of counteracting gravity for these atoms, it is instead enhanced by a factor of two. Additionally the field zero would create a point at which there is no quantisation axis to ensure that the atoms remain in the Zeeman state they were prepared in.

To remedy this issue, an offset or "bias" field can be used to shift the position of the field zero away from the atomic cloud. This field can be provided by an addition set of coils in the Helmholtz configuration, with the currents through the two coils flowing in the same direction. For high-field seeking atomic states, this bias field must be positive such that the magnetic field zero is at lower $z$ than the atomic cloud and hence the atoms see a gradient field that is continually increasing with increasing $z$. The atoms would then always experience a force that counteracts gravity.

In our setup we have a pair of bias coils and a pair of quadrupole around the MOT Chamber and Science Cell, see Table 2.2. Their centre sets the position of the start and end points of the transport path respectively. However due to the limited size of the quadrupole coils, with a radius of about 4 cm, they only cover the edges of the transport. Moving away from their axis, the magnitude of the magnetic gradient field produced by the quadrupole coils diminishes and the direction of the field will become increasingly horizontal until, on the far side of the coils' radii, the field once again becomes increasingly vertical, this time with opposite sign. The reason for this behaviour becomes clear when recalling that magnetic field lines must form complete loops. This also means that when moving away from the axis of the coils the magnitude of the gradient field also decreases before it too changes sign before asymptotically approaching zero for distances much greater than the coil radius. The drop-off in magnetic gradient field is purely a geometric effect, and cannot be eliminated by adjusting the current, and hence central gradient field of the coils.

This implies a diminished ability to counteract gravity when the atoms are transported out of the MOT chamber (and before they arrive in Science Cell) and even a slight enhancement in the trap tilting at some distances along the transport path. This is only the case if the offset field applied to atoms were to be uniform across the transport path. The bias coils too have have a finite extent, with a radii of 6.6cm and 5.2cm for the MOT Chamber and Science Cell coils respectively. The offset field they produce is therefore also not homogenous along the transport path and its direction will also vary. This spatial variation must be taken into account in combination with the spatial variation of the field produced by the quadrupole coils.

### Application to Cs, Rb and K

We work with atoms in their ground state: Cs in $|F = 3, m_F = 3\rangle$, Rb in $|F = 1, m_F = 1\rangle$ and K in $|F = 1, m_F = 1\rangle$ which are all high-field seeking. This means their energy is reduced at larger fields as $g_\mathrm{F}$ is negative. Hence to counteract gravity, the magnetic gradient must be positive $B' > 0$ such that $B$ increases with increasing

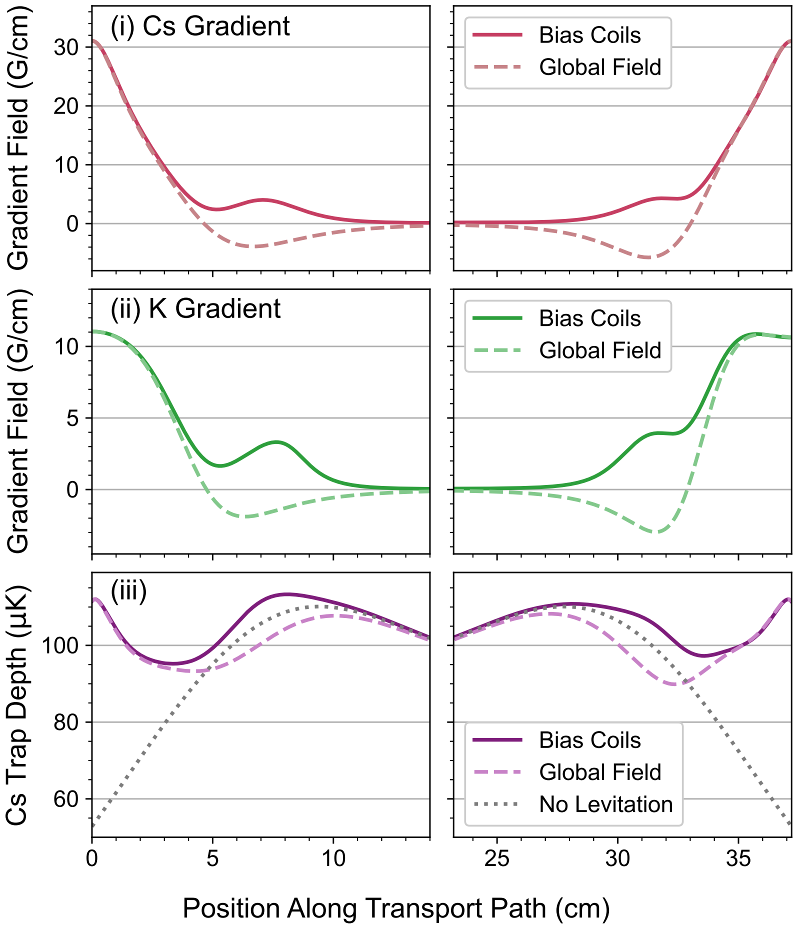

Figure 2.9: Magnetic gradient field produced for levitation as a function of the position along the transport path. The central gradient is set to the levitation gradient for Cs in (i) and for K in (ii). The gradient fields are calculated both using the bias coils centred on the MOT Chamber and Science Cell, set to give a 22G field at their centre, shown by the solid lines. The gradient field are also calculated using a global, global offset field of 22G, shown in the dashed lines. (iii) Shows the vertical trap depth for Cs in both levitation configurations and in the unlevitated case. The beam parameters used are $x_0 = 7.2$cm and $w_0 = 195\mu$m, see Section 2.5.3.

| Coil | Radius $R$ (cm) | Separation $s$ (cm) | Turns $N$ |
|---|---|---|---|
| MC Bias | 6.6(2) | 6.83(8) | 8 |
| MC Quad | 4.0(1) | 6.89(4) | 6 |
| SC Bias | 5.156(1) | 5.88(1) | 12 |
| SC Quad | 3.917(2) | 5.2(4) | 6 |

Table 2.2: Table of measured coil parameters. Values are based on equivalent-coil fits to calibration measurements of the magnetic field along the axis of each coil pair.

$z$. A negative gradient field $B' < 0$ would "anti-levitate" the atoms, enhancing the gravitational tilt. In these states, the values for $g_{\mathrm{F}}$ can be taken as $-1/4$ for Cs [146] and $-1/2$ for Rb [147] to a good approximation[3].

For all subsequent calculations, the current through the bias coils is set to give a 22 G offset field, which corresponds to the Cs three-body loss minimum [148]. Due to a fortunate near-equivalence in the mass-magnetic moment ratio for Cs and Rb, the gradient fields required to levitate those species are 31.1G/cm and 30.6G/cm respectively. For simplicity a gradient field of 31G/cm is used for both Cs and Rb in all subsequent calculations.

However for K, the ground state hyperfine splitting is much smaller at 0.254GHz [149], compared to 6.83GHz for Rb [147] and 9.19GHz for Cs [146], such that the weak field approximation is no longer valid. Hence the potential is no longer linear with magnetic field. For the purposes of magnetic levitation this means that $B'_{\mathrm{lev}}$ depends on the magnitude of the offset field used. For the offset field of 22G used (discussed in the next section) K requires a gradient field of 11G/cm, which is the value used for later calculations. The challenges arising from the different gradient field required for K are discussed in Section 2.5.4.

The variation in magnetic gradient field along the transport path is shown in Figure 2.9 for both the Cs and K levitation gradients. The gradient field is plotted in the case where there is uniform, global offset field (dashed lines) and when taking

---

[3] This assumes that the contribution to $g_{\mathrm{F}}$ from the nuclear spin is zero and that $g_{\mathrm{J}} = 2$ for the ground state. Both of these are reasonable assumptions, with $g_{\mathrm{F}} = -0.2508$ for Cs and $g_{\mathrm{F}} = -0.5018$ for Rb when these assumptions are relaxed. Data is taken from the same references.

the finite extent of the bias coils into account (solid lines). In the case of a global offset field, the gradient field becomes negative approximately 4cm from the centres of the gradient coils before decreasing back to zero, as discussed above. In this region, the atoms would be anti-levitated by the magnetic gradient. Fortunately, when the real bias coil pairs are considered instead, the gradient field diminishes to zero without ever becoming negative for both the MOT Chamber and Science Cell coils. Hence the magnetic levitation in our experiment will only ever be beneficial for the radial trap depth.

Also shown are the vertical trap depths for Cs in both levitation scenarios (solid lines and dashed lines respectively) and in the case without levitation. The difference in trap depth between the levitated an unlevitated cases is stark which highlights the usefulness of magnetic levitation, which will be fully explored in Section 2.5.3. The beam shapes used are those which will be found optimum in that section.

### Calculating the Magnetic Field

Finding the magnetic field produced by the quadrupole and bias coils for transport is complicated as the field away from the coils' axis must be calculated. Due to the cylindrical symmetry of the coils, we work in cylindrical polar coordinates $(\rho, \phi, z)$ where $\rho$ is the radial distance, where $\phi$ is the azimuthal angle, and $z$ is the axial position. Note that $\rho_{\text{coils}}$ used here is not the same as the $\rho_{\text{beam}}$ used in Section 2.3.2, with $\rho_{\text{coils}} = \sqrt{x^2 + y^2}$ and $\rho_{\text{beam}} = \sqrt{y^2 + z^2}$, as the axes of symmetry for the beams and the coils are orthogonal. For the calculations we use an "equivalent" coil wherein a real coil is treated as a thin coil with one turn with a radius $R$. The current through the equivalent coil is given by $I = NI_{\text{real}}$ where $N$ is the number of turns in the real coil and $I_{\text{real}}$ is the current through the real coil. An equivalent coil pair is made of two coils of the same radius and current which have a separation $s$. The origin is taken to be at the centre of the coil pair such that the individual coils are centred on $z = +s/2$ and $z = -s/2$. The $B$-field contribution from a single coil is given by [17]

$$
\begin{aligned}
B_\rho &= \frac{\mu_0 I}{2\pi} \frac{\tilde{z}}{\rho\sqrt{(R+\rho)^2 + \tilde{z}^2}} \left[ \frac{R^2 + \rho^2 + \tilde{z}^2}{(R-\rho)^2 + \tilde{z}^2} E(\kappa) - K(\kappa) \right], \\
B_\phi &= 0, \qquad (2.59) \\
B_z &= \frac{\mu_0 I}{2\pi} \frac{1}{\sqrt{(R+\rho)^2 + \tilde{z}^2}} \left[ \frac{R^2 - \rho^2 - \tilde{z}^2}{(R-\rho)^2 + \tilde{z}^2} E(\kappa) + K(\kappa) \right],
\end{aligned}
$$

where $\tilde{z} = z \mp s/2$ for a coil centred at $z = \pm s/2$. $K(\kappa)$ and $E(\kappa)$ are complete elliptic integrals of the first and second kind given by

$$K(\kappa) = \int_0^{\pi/2} d\theta \frac{1}{\sqrt{1 - \kappa \sin^2\theta}}, \qquad (2.60)$$

and

$$E(\kappa) = \int_0^{\pi/2} d\theta \sqrt{1 - \kappa \sin^2\theta}, \qquad (2.61)$$

with the argument $\kappa$ given by

$$\kappa = \frac{4R\rho}{(R+\rho)^2 + \tilde{z}^2}. \qquad (2.62)$$

These equations are derived using the Biot-Savart law to find the vector potential $\mathbf{A}$ from the coil loop, which has only a $A_\phi$ component equal to

$$A_\phi = \frac{\mu_0 I}{\pi} \frac{1}{\kappa} \sqrt{\frac{R}{\rho}} \left[ \left(1 - \frac{1}{2}\kappa^2\right) K(\kappa) - E(\kappa) \right]. \qquad (2.63)$$

From there the $B$-field components are found by taking the curl $\mathbf{B} = \nabla \times \mathbf{A}$. Full derivations can be found in [150] and [151].

For the transport calculations, the $B_\rho$ and $B_z$ contributions from each individual coil are calculated and summed to find the magnitude $|\mathbf{B}|$. For the bias coils in the Helmholtz configuration both coils have current flowing in the same direction, whereas for the quadrupole coils in the anti-Helmholtz configuration the coils have current flowing in opposite directions. The upper quadrupole coil, centred at $z = +s/2$, has a negative current while all other coils have a positive current.

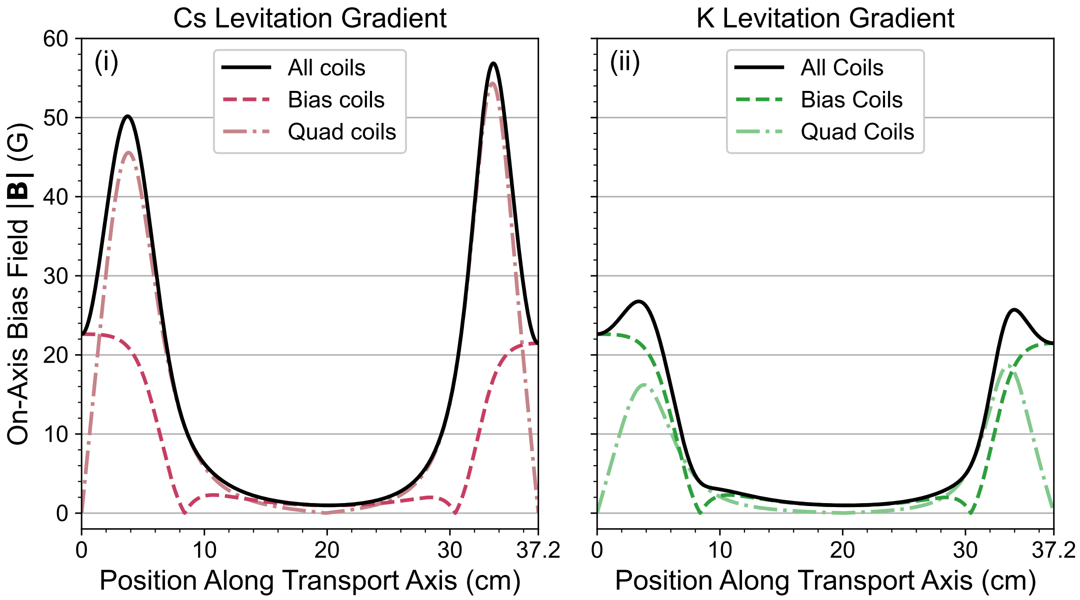

Figure 2.10: Magnetic bias field on the transport axis, $z = 0$ and $y = 0$, along the transport path (solid lines). Contributions from the bias coils (dashed lines) and quadrupole coils (dash-dotted lines) are shown with the bias coil currents set to give a 22G offset field at both ends of the transport path and the quadrupole coil currents set to fully levitate Cs in panel (i) and K in panel (ii).

### Magnetic Anti-Trapping

As well as the beneficial gradient field vertically, the quadrupole coils also produce anti-trapping potential terms in the directions orthogonal to the coils' axis [152,153]. This can significantly reduce the trap depths in some circumstance, and must be compensated for with a sufficiently large bias field. For our transport scheme, the trap depths affected are in the axial and horizontal radial directions. Fortunately in our case this effect is negligible, causing a reduction no greater than 1%. This is due to the size of the beam relative to the coils as well as the 22G bias field used. Additionally, the horizontal trap depth is the one most significantly affected but it is not limiting in any of the following optimisations. Hence this small effect is omitted in the subsequent calculations.

**Quantisation Axis**

Due to degenerate Raman sideband cooling used to prepare atoms in the Main Chamber, Cs and Rb atoms are prepared in their lowest hyperfine states, $|F = 3, m_{\mathrm{F}} = 3\rangle$ and $|F = 1, m_{\mathrm{F}} = 1\rangle$ respectively. To ensure the atoms remain in these states, a quantisation axis in the form of a bias magnetic field must be provided to the atoms throughout the transport path.

Fortunately, the bias and quadrupole coils around the Main Chamber and Science Cell provide a sufficient bias field throughout the transport path, even with currents set to those required for magnetic levitation. Figure 2.10 shows the variation of the bias field along the entire transport path, for both the Cs and K levitation gradient fields. The bias field on the transport axis is considered $y = z = 0$ (or equivalently $\rho = 0$). The contributions of the bias (quadrupole) coils is shown in the dashed (dash-dotted) lines. For both gradient fields, the minimum offset field is 1G which is sufficient to provide a quantisation axis.

To confirm that the atoms do remain in the same hyperfine state, we perform Stern-Gerlach separation. Optical traps are turned off but the magnetic field is kept at the levitation gradient for the lowest hyperfine states. Any atoms not in that state would then be spacially separated. We do not observe any atoms in other hyperfine states.

## 2.4 The Simplest Beam Configuration

As a starting point in optimising the beam parameters, we will consider the simplest case: two beams of equal power and beam size focused at the centre of the transport path, $x = 18.6$cm. The optical conveyor-belt is formed from two transport beams, derived from separate 30W 1064nm fibre amplifiers. Details of the amplifier setup are presented in Chapter 3. For the purpose of these calculations a conservative estimate of 18W of power for each beam is taken. Note that while the power dictates the trap depth, it does not affect the optimisation.

Initially, the vertical trap depth is considered without any magnetic levitation. The effect of adding magnetic levitation is considered in Section 2.4.1. In Sec-

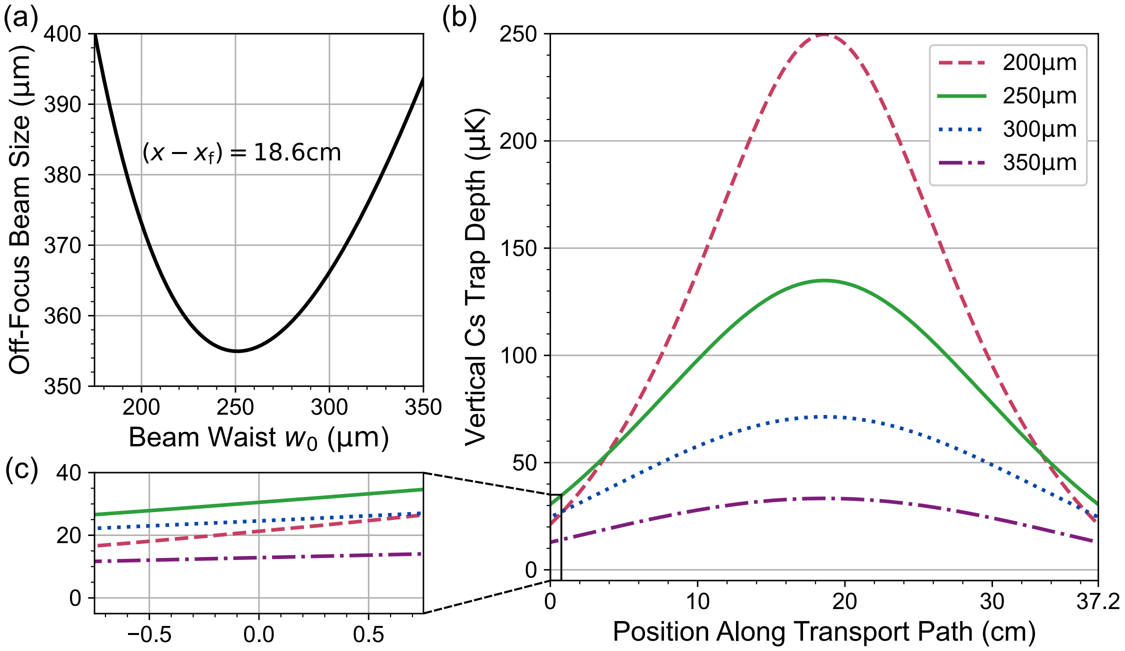

Figure 2.11: Varying the beam waist for the simplest case of two beam of equal power both focused at the centre of the transport path, $x = 18.6$cm. (a) Shows the dependence on beam waist of the beam size at the edges of the transport path where $(x - x_\mathrm{f}) = 18.6$cm. (b) Shows the Cs vertical radial trap depth variation along the transport path for different beam waists. (c) Shows a zoom-in of the same trap depths for the MOT Chamber end of the transport path.

tion 2.4.2, the assumption that both beams are focused at the centre of the transport path is relaxed.

With these assumptions, the only parameter left to optimise is the beam waist $w_0$, common to both beams. With both beams focussed at the centre of the transport path, the trap depth at the edges of the transport path will be the lowest. Hence we only need to consider the trap depth at the start of the transport path, $x = 0$cm, or equivalently at the end of the transport path, $x = 37.2$cm. The optimum waist will therefore be the one that minimise the beam size 18.6cm from the beam's focus.

This optimum can be found analytically and for the general case of minimising the beam size at some distance $s$ from the focus. For Gaussian beams, the beam size $w$ varies with axial position $x$ and beam waist $w_0$ according to:

$$w(x, w_0) = w_0\sqrt{1 + \frac{(x - x_\mathrm{f})^2}{{x_\mathrm{R}}^2}} = w_0\sqrt{1 + \frac{(x - x_\mathrm{f})^2\lambda^2}{\pi^2{w_0}^4}} \tag{2.64}$$

where $\lambda$ is the wavelength and $x_{\mathrm{f}}$ is the focus position. As we want to find the minimum beam size at a given position away from the beam focus, we can set $x = s$ and treat is as a constant. Then taking the derivative of $w$ with respect to $w_0$ and setting it to zero:

$$\frac{dw}{dw_0} = \sqrt{1 + \frac{(s - x_{\mathrm{f}})^2 \lambda^2}{\pi^2 {w_0}^4}} + w_0 \left(\frac{1}{2}\right) \left(1 + \frac{(s - x_{\mathrm{f}})^2 \lambda^2}{\pi^2 {w_0}^4}\right)^{-\frac{1}{2}} \left(-4\frac{(s - x_{\mathrm{f}})^2 \lambda^2}{\pi^2} {w_0}^{-5}\right), \tag{2.65}$$

$$\frac{dw}{dw_0} = 0 \Rightarrow 1 - \frac{(s - x_{\mathrm{f}})^2 \lambda^2}{\pi^2 {w_0}^4} = 0, \tag{2.66}$$

$$\therefore (s - x_{\mathrm{f}})^2 = \frac{\pi^2 {w_0}^4}{\lambda^2} = {x_{\mathrm{R}}}^2. \tag{2.67}$$

Hence, the optimum waist is that for which $s$ is exactly one Rayleigh range from the focus. Rearranging gives:

$$w_0 = \sqrt{\frac{\lambda}{\pi} |s - x_{\mathrm{f}}|}, \tag{2.68}$$

where the absolute value ensures a real $w_0$ is taken for all $s$. In our case we have 1064nm light and distance away from the focus position equal to half the transport distance $(s - x_{\mathrm{f}}) = 18.6$cm, giving an optimum waist of $w_0 = 251\mu$m.

Figure 2.11 shows the effect of varying the beam waist on the trap depth. The variation of the beam size a distance of 18.6cm away from the focus is shown in 2.11(a), with the minimum around 250$\mu$m clearly visible. The variation in vertical trap depth along the transport path for a range of beam waists is shown in 2.11(b) and a more detailed plot of the depth close to the edge of the transport path shown in 2.11(c). The trap depths for Cs are shown, but in this case all species share the same optimum.

The significance of the beam size on the gravitational tilt can again be seen in this figure. Looking at the trap depth for the 250$\mu$m waist beams, the trap depth at the edges is a factor of 4.5 smaller at the edges than at the centre. As the edge and the centre are exactly a Rayleigh range apart, the radial trap depth in the horizontal direction drops by only a factor of 2.

The optimum waist of 250$\mu$m, shown by the solid green line, gives a minimum

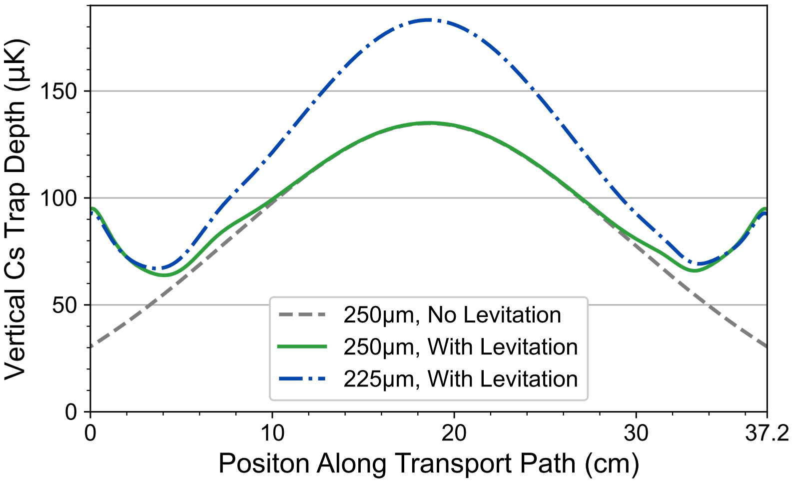

Figure 2.12: Adding magnetic levitation to the simplest case. The Cs vertical radial trap depth is shown with (without) levitation by the solid green (dashed grey) lines, with previously optimum waist of $w_0 = 250\mu$m. The levitated trap depth for a reduced beam size of $w_0 = 225\mu$m is shown by the blue dash-dotted line which yields a further increase in minimum trap depth compared to a waist of $250\mu$m.

trap depth of $30.5\mu$K for Cs, $15.2\mu$K for Rb and $26.3\mu$K for K. Beams of smaller waists, $200\mu$m is shown in the dashed red line, give a greater trap depth at the beams' focus but suffer from a sharper drop-off towards the edge of the transport. On the other hand larger waists, $300\mu$m shown in the blue dotted line and $350\mu$m shown in the purple dash-dotted line, give a smaller variation in trap depth along the trap depth but again with a lower trap depth at the edges of the transport path.

### 2.4.1 Adding in Levitation

Now we will consider the effect of adding in magnetic levitation. In our setup we have two pairs of quadrupole coils of radius $\sim$ 4cm, centred on the MOT Chamber and Science Cell respectively. These, combined with a bias field, can compensate the gravitational tilt and thereby increase the minimum trap depth.

Figure 2.12 shows the effect of including the quadrupole coils and the bias coils, with the previous unlevitated case shown in the grey dashed line and the levitated case shown in green. At the edges of the transport path the gravitational tilt is compensated fully and the vertical radial trap depth becomes equal to the horizontal

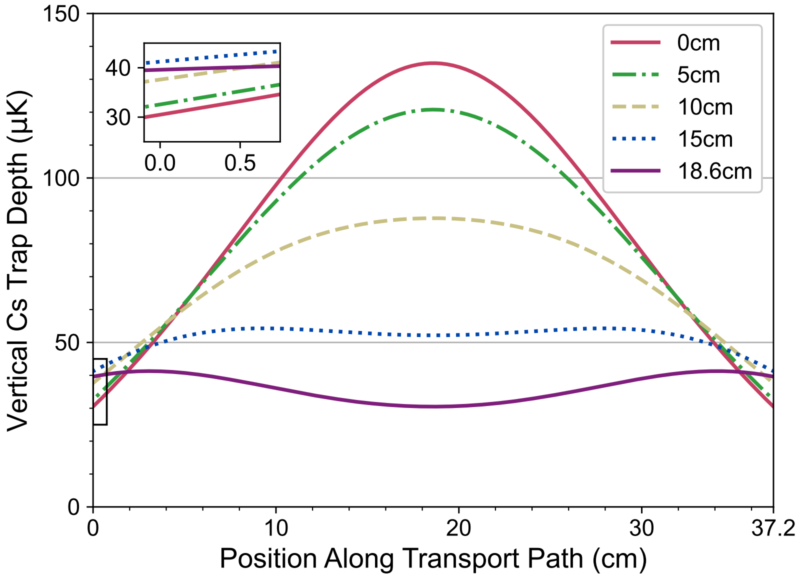

Figure 2.13: Adding an offset to the beams' focus positions in the simplest case. The beams are displaced in opposite directions along the transport axis by the amount indicated. In the case of 0cm displacement (solid red line) the two beams are positioned as before, whereas for 18.6cm displacement, Beam 1 and Beam 2 are focussed in the MOT Chamber and Science Cell respectively.

radial trap depth at 94$\mu$K for Cs. However, as the drop off in gradient field moving away from the centre of the coils outcompetes the decrease in beam size moving close to the focus, the minimum trap no longer occurs at the edge of the transport path. Instead the minima are now at $x = 4.1$cm and $x = 33.2$cm with depth of 62.6$\mu$K and 64.7$\mu$K respectively for Cs. The differences between the two trap depth minima is due to the slightly different sizes of the MOT Chamber and Science Cell quadrupole and bias coils.

With the position of the trap depth minimum now closer to the centre of transport path, and hence also the focus positions of the beams, further improvements in the trap depth can be gained by reducing the beam waist. An example is shown by the blue dash-dotted line, which the shows the levitated trap depth for a the beam waist of 225$\mu$m. This waist yields trap depth minima of 65.8$\mu$K and 67.9$\mu$K, situated at $x = 3.6$cm and $x = 33.4$cm respectively.

### 2.4.2 Separating the beams

Returning back to the calculations without magnetic levitation, we will now consider the effect of adding an offset to the beams. As the problem has mirror symmetry around the centre of the transport path, an equal offset of $\Delta x$ is added to both beams. Beam 1 (Beam 2) is offset towards smaller (larger) $x$ to be focused closer to the MOT Chamber (Science Cell).

The trap depths for three different beam offsets are shown in Figure 2.13. An increase in trap depth at the edge of the transport path is clearly seen in the inset. This increase grows with the displacement up to 15cm, which gives a minimum Cs trap depth of 40.3$\mu$K. For the even larger offset of $\Delta x = 18.6$cm, where the beams are focused at the edges of the transport path, the trap depth reduces again. This is due to diminished contribution of the beam furthest away from each edge (Beam 2 in the MOT chamber and Beam 1 in the Science Cell). For $\Delta x = 18.6$cm an additional trap depth minimum is evident at the centre of the transport path, at $x = 18.6$cm.

As for the calculations adding in magnetic levitation, the distance between the trap depth minimum and the beams' foci is reduced when an offset is added, opening up the possibility of further increases in trap depth by reducing the beam waists. This is explored in the following sections where the beam waist and beam offsets are varied simultaneously.

## 2.5 The Full Solution

Following on from the basic calculations, we will now fully optimise the transport lattice trap depths. As before each beam is assumed to have a power of 18W. Due to the equal power in the two transport lattice beams, there is a mirror symmetry in the problem of optimising the trap depth along the centre of the transport path. The optimum beam shapes will respect this symmetry and therefore the two beam waists and the focus position's displacement from the centre of the transport path will be equal. This is illustrated in Figure 2.14, with the beams waist set to $w_0$ and beam 1 (green) and beam 2 (blue) focused a distance $x_0$ from the MOT Chamber

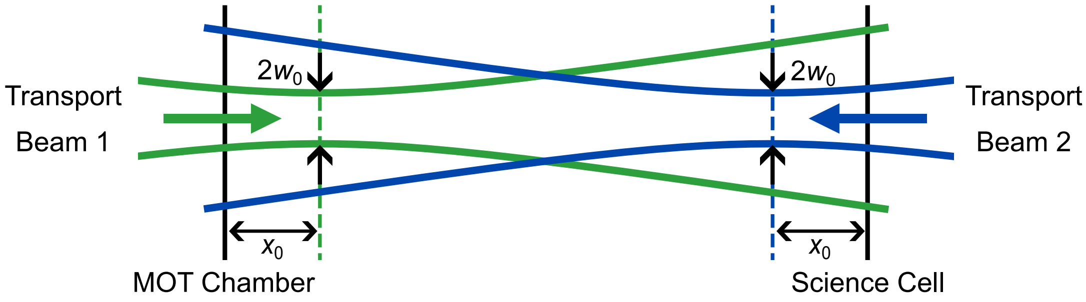

Figure 2.14: Sketch of the transport beams in the equal power case. The beam size of beam 1 (beam 2) along the transport path is illustrated by the green (blue) lines. Both beams share a waist of $w_0$ and a focus position $x_0$ away from the MOT Chamber and Science Cell respectively.

and Science Cell respectively. These two parameters, $w_0$ and $x_0$, are the main focus of the trap depth optimisation.

As a starting point, we will optimise for the vertical radial depth in Section 2.5.1 before considering the axial depth in Section 2.5.2. In Section 2.5.3 the effects of adding in magnetic levitation are included. Finally, Section 2.5.4 will compare the optimum transport conditions for the three different species.

### 2.5.1 Optimise for Radial Depth

The beam shapes are optimised by varying $x_0$ and $w_0$ simultaneously. As discussed in Section 2.4.2, offsetting the beams relative to each other changes the distance between their focus position and the location of the trap depth minimum and hence the waist that gives the greatest minimum trap depth. In this first optimisation, magnetic levitation is not considered. Due to the symmetry of the two lattice beams, the trap depth minimum can therefore either be in the centre of the transport path, for smaller values of $x_0$, or at *both* ends of the transport path for larger values of $x_0$. Therefore, the trap depth need only be calculated at one of the ends of the transport path, say $x = 0$cm, and at the centre $x = 18.6$cm and the minimum of those two values taken.

Figure 2.15(a) shows the contour plot of the minimum trap depth of Cs versus $x_0$ and $w_0$ with yellow/bright regions signifying deeper traps and blue/dark regions shallow traps to no trap. The focus position is varied from 0 cm to 18.6 cm, cor-

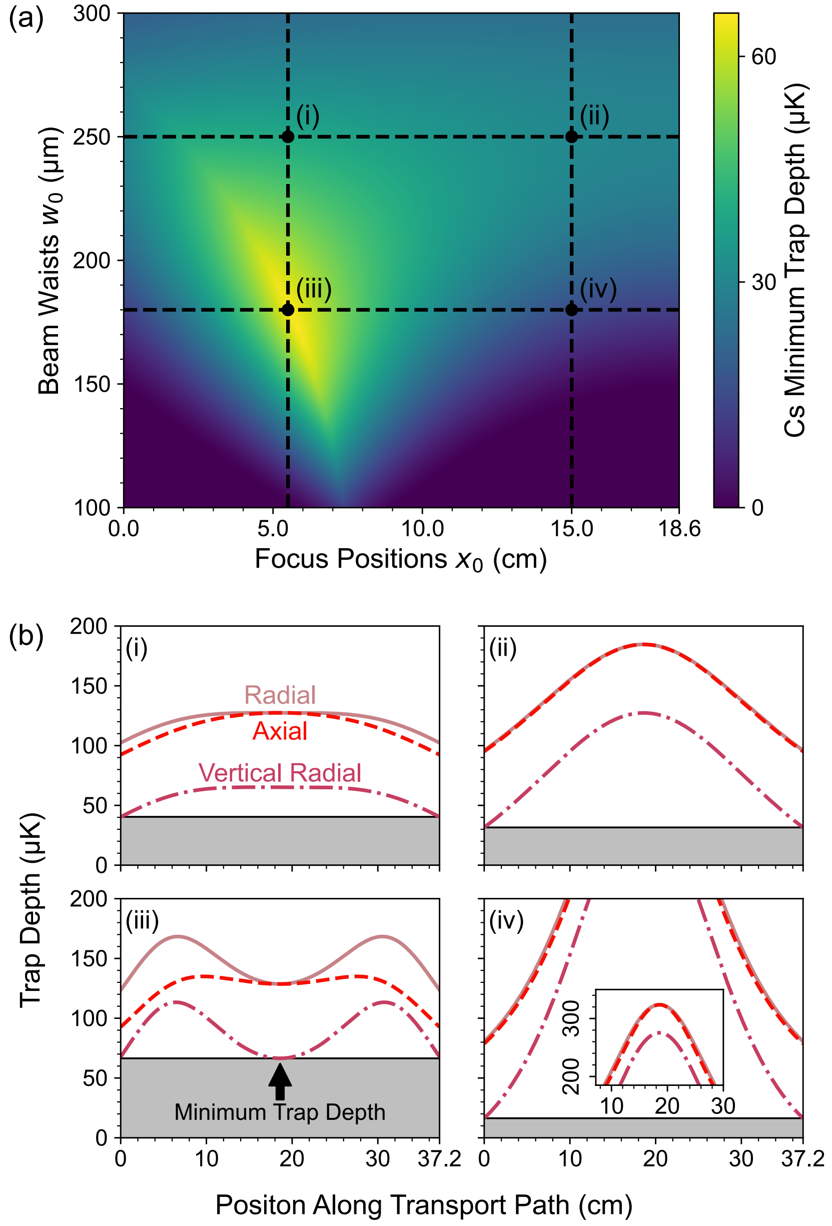

Figure 2.15: Optimisation of the radial trap depth. (a) Shows a contour plot of the minimum trap depth for Cs along the transport path, varying the waists and focus positions of the lattice beams. (b) Shows the variation of the trap depth along the transport path in the axial (red dashed lines), radial (light red solid lines) and radial with gravity (dark red dash-dotted lines) for different beam parameters. The minimum trap depth is indicated with the grey shaded region and is maximised in (iii) with $x_0 = 5.5$ cm and $w_0 = 180$ $\mu$m, when the trap depth in the centre is equal to that at either end.

responding to the beams being focused in the centre of their respective vacuum chamber and being focused at the centre of the transport path respectively. The beams waists is varied between 100$\mu$m and 300$\mu$m in order to give a broad enough range to encompass the previous consideration. Only the optimisation contour for Cs is shown here, although as will be shown explicitly in Section 2.5.4 there is a negligible difference between the three species for this optimisation.

Figure 2.15(b) shows how the trap depth varies along the transport path for four different pairs of $x_0$ and $w_0$ values. The black horizontal line and the grey shaded region show the minimum trap depth. As panel (iii) shows, the optimum beam shapes of $x_0 = 5.5$cm and $w_0 = 180\mu$m, balance the trap depths at the edges and at the centre. As can be seen in Figure 2.15, (iii) lies on a distinct "ridge" that exists for focus positions up to $\sim 7.5$cm which consists of pairs of beam shape parameters that balance the trap depth at the centre and edges of the transport path. Left of the ridge the centre trap depth is limiting, while on its right the edges of the transport path are limiting.

Increasing the waist to 250$\mu$m, as seen in (i), flattens the trap depth profile, but at the cost of reduced trap depth at the edges. The larger waist means lower peak intensity and hence lower trap depth. At the same time, a larger waist beam has a longer Rayleigh range and so slower drop-off of intensity and trap depth away from the focus. On the other hand increasing $x_0$ to 15cm, as seen in (iv), greatly increases the trap depth around the centre of the transport path at the cost of a dramatic reduction at the edges. Finally (ii) shows the case of larger $x_0$ and $w_0$ with a flatter profile than (iv) but still with the same limitation.

### Comparing Axial and Radial Depths

For all four of the selected points, the axial trap depth is always less than or equal to the radial trap depth (without gravity). This is in fact a general result for a 1D optical lattice which becomes clear when considering the difference between the two depths:

$$\mathcal{U}_{\text{Radial}} - \mathcal{U}_{\text{Axial}} = \mathcal{A}\left(\mathcal{I}_1 + \mathcal{I}_2 - 2\sqrt{\mathcal{I}_1\mathcal{I}_2}\right) = \mathcal{A}\Big(\sqrt{\mathcal{I}_1} - \sqrt{\mathcal{I}_2}\Big)^2. \tag{2.69}$$

The difference between the two depths is proportional to a square of real quantities, $I_1$ and $I_2$, and $\mathcal{A}$ is positive. Hence the difference can never be negative and the axial depth is never greater than the radial depth. In the limiting case of $I_1 = I_2$ the two depths are equal. This means that when adding in the magnetic levitation to increase the vertical trap depth, we need only to compare it to the axial trap depth.

### 2.5.2 Optimise for Axial Depth

As for the radial trap depth, we can optimise for the axial trap depth by simultaneously varying the beam waists and focus positions in order to find a contour similar to Figure 2.15(a), which is shown in Figure 2.16(a). The contour for the axial optimisation does however look rather different to the radial contour, with a large portion of the parameter space yield a minimum trap depth close to the optimum. In fact it will be shown below, there is not a single pair of optimum beam parameters. Rather there is a "ridge" of beam parameters that give the same minimum trap depth.

To gain some insight into the axial optimisation, the axial depth is considered analytically which will give the expressions for the two curves shown in Figure 2.16(a). From Equation 2.44, the axial depth is given by

$$\mathcal{U}_{\text{axial}}(x) = 4\mathcal{A}\sqrt{\mathcal{I}_1(x)\mathcal{I}_2(x)} = 8\mathcal{A}\frac{P}{\pi}\left(\frac{1}{w_1(x)w_2(x)}\right). \tag{2.70}$$

The axial depth can thus be optimised by minimising the denominator in the equation above, $D = w_1(x)w_2(x)$. In order to make this minimisation tractable, we will make the simplifying assumption that the minimum trap depth will occur at the edges of the transport path. We will return back to this assumption later to find the region over which it holds true, but for now simply point out that this is the case for the four beam parameter pairs selected in Figure 2.15. Due to the symmetry of the beams, the trap depth at either end of the transport path will be equal. Selecting $x = 0$ and expanding out the terms gives

$$D(x=0) = {w_0}^2\sqrt{1+\frac{(x_0)^2\lambda^2}{\pi^2 {w_0}^4}}\;\sqrt{1+\frac{(d-x_0)^2\lambda^2}{\pi^2 {w_0}^4}}. \tag{2.71}$$

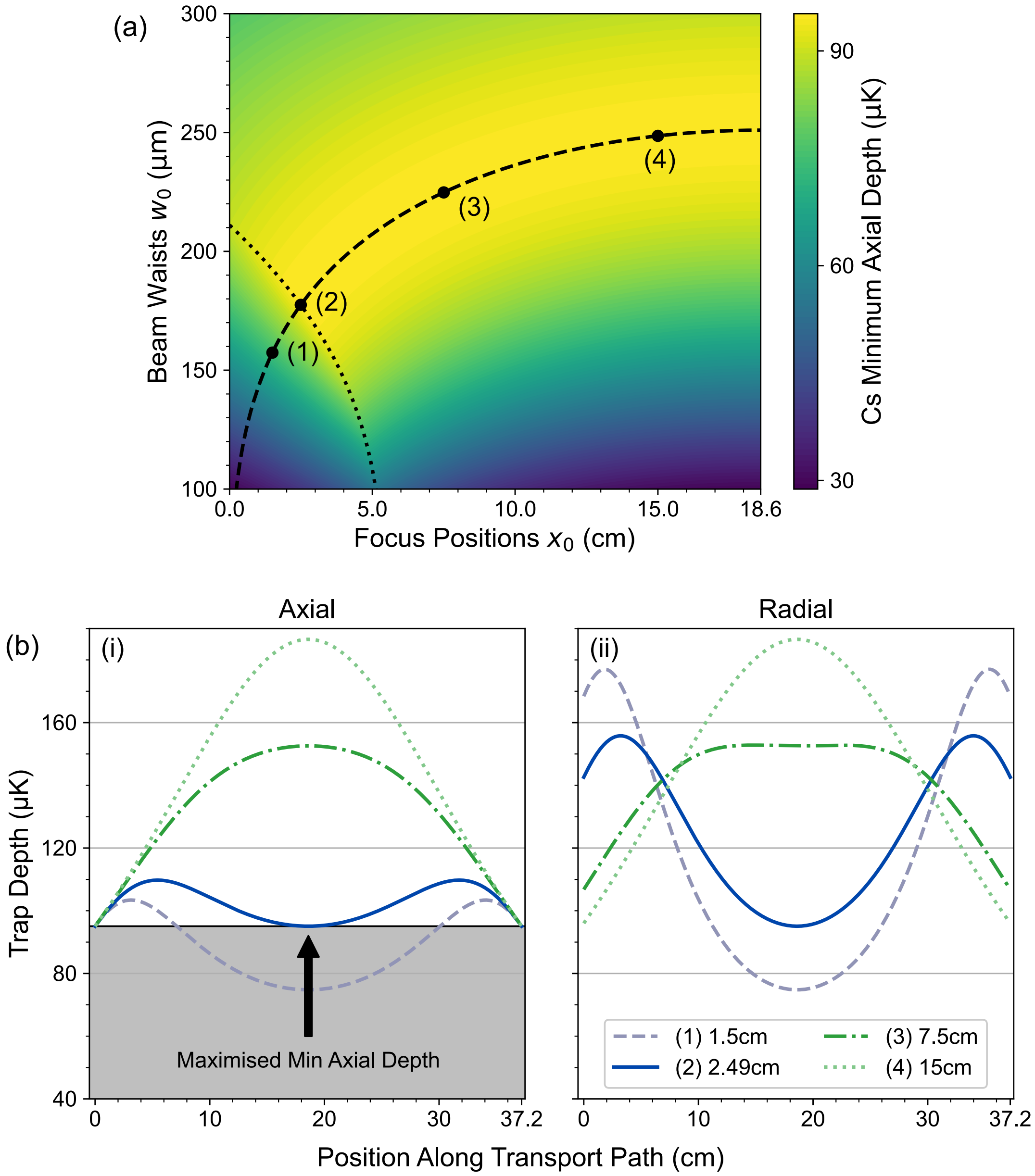

Figure 2.16: Optimising for the axial depth only. (a) Shows a contour plot of the Cs axial depth against the focus position $x_0$ and the beam waist $w_0$. The black dotted line shows the values for which the axial depth at the centre and the two ends is equal. The black dashed line shows the "ridge" of $x_0$ and their corresponding $w_0$ values that give the same minimum axial depth, located at both ends of the transport path. Four pairs of $x_0$ and $w_0$ values, points (1)-(4), are indicated with black circles. For these points, (b) shows the trap depths throughout the transport path (i) in the axial and (ii) in the radial direction.

as the equation to minimise. A *relatively* straightforward way of doing this is to treat $x_0$ as a parameter and minimise $D$ with respect to $w_0$:

$$\begin{aligned}\frac{dD}{dw_0} =&2w_0\sqrt{1+\frac{(x_0)^2\lambda^2}{\pi^2{w_0}^4}}\ \sqrt{1+\frac{(d-x_0)^2\lambda^2}{\pi^2{w_0}^4}}\\ &+{w_0}^2\left((-4{x_0}^2{w_0}^{-5})\frac{\sqrt{1+\frac{(d-x_0)^2\lambda^2}{\pi^2{w_0}^4}}}{2\sqrt{1+\frac{(x_0)^2\lambda^2}{\pi^2{w_0}^4}}}\right)\\ &+{w_0}^2\left((-4(d-x_0)^2{w_0}^{-5})\frac{\sqrt{1+\frac{(x_0)^2\lambda^2}{\pi^2{w_0}^4}}}{2\sqrt{1+\frac{(d-x_0)^2\lambda^2}{\pi^2{w_0}^4}}}\right)\end{aligned} \tag{2.72}$$

$$\frac{dD}{dw_0}=0 \Rightarrow 1-\frac{1}{{w_0}^8}\left(\frac{\lambda}{\pi}\right)^4(d-x_0)^2(x_0)^2=0 \tag{2.73}$$

Hence:

$$w_0=\sqrt{\frac{\lambda}{\pi}}\ \sqrt[4]{x_0\,(d-x_0)},\text{ for } 0\leq x_0\leq d, \tag{2.74}$$

which defines the black dashed line in Figure 2.16. Substituting this back into Equation 2.70 and simplifying gives:

$$\mathcal{U}_{\text{axial}}=8\mathcal{A}\frac{P}{\lambda d} \tag{2.75}$$

which interestingly is independent of $x_0$. This means that there is not a single pair of values for $w_0$ and $x_0$ that maximise the axial trap depth on either edge of the transport path. Instead for any value of $x_0$ (within the range $0\leq x_0\leq d/2$ we are interested in), there exists a value of $w_0$ which will give the same minimum axial depth. This maximum axial depth is equal to $95.1\mu$K for Cs, $56.2\mu$K for Rb and $48.9\mu$K for K.

However, this only holds if the edges of the transport are in fact where the axial trap depth is minimum, the simplifying assumption made earlier. The other possibility is that the axial trap depth minimum occurs in the centre of the transport path at $x=d/2=18.6$cm. In order to find the values of $x_0$ for which the axial trap depth at the edges is smaller than the axial depth at the centre, we will consider the limiting case where they are equal, giving:

$$\left(1+\frac{(d/2-x_0)^2}{{x_\mathrm{R}}^2}\right)=\sqrt{1+\frac{(d-x_0)^2}{{x_\mathrm{R}}^2}}\sqrt{1+\frac{(x_0)^2}{{x_\mathrm{R}}^2}} \tag{2.76}$$

Squaring both sides, expanding and collecting terms gives:

$${x_\mathrm{R}}^2\left[2(d/2-x_0)^2-(d-x_0)^2-{x_0}^2\right]={x_0}^2(d-x_0)^2-(d/2-x_0)^4 \tag{2.77}$$

Rearranging and substituting in the equation for the Rayleigh ranges:

$$w_0=\sqrt{\frac{\lambda}{\pi}}\sqrt[4]{{x_0}^2-x_0d+\frac{d^2}{8}},\ \text{for } 0\le x_0<d\left(\frac{1}{2}-\frac{1}{\sqrt{8}}\right), \tag{2.78}$$

which is shown in Figure 2.16(a) by the black dotted line. Thus we can find the point at which the two lines cross by setting Equation 2.78 equal to Equation 2.74

$$x_0\ge\frac{d}{2}\left(1-\frac{\sqrt{3}}{2}\right)\approx 0.0670d, \tag{2.79}$$

which for our transport distance $d = 37.2\text{cm}$ gives $x_0 \ge 2.49\text{cm}$.

Putting it all together, for each value of the focus positions $x_0$ there exists a beam waist $w_0$, given by Equation 2.74, such that the axial depth at the edges of the transport is equal to the same value. This value is given by 2.75 and is independent of $x_0$ and $w_0$. Values of $x_0$ for which the axial depth is limited by the depth at the edges of the transport path is given by Equation 2.79. Combined these equations define the ridge of beam parameter values that yield the same optimum axial depth, shown by the dashed black line in Figure 2.16(a).

The variation in trap depth along the transport path for four different points along the optimum ridge is plotted in Figure 2.16(b). Point (1) shows the case for small $x_0$ where the beams are too close to the edges of the transport path and the minimum axial trap depth occurs at the centre of the transport path; point (2) shows the limiting case where the depth at the edges and centre are exactly equal; while points (3) and (4) show two examples for which the axial trap depth is limited only by the edges. The optimised minimum trap depth is indicated by the arrow

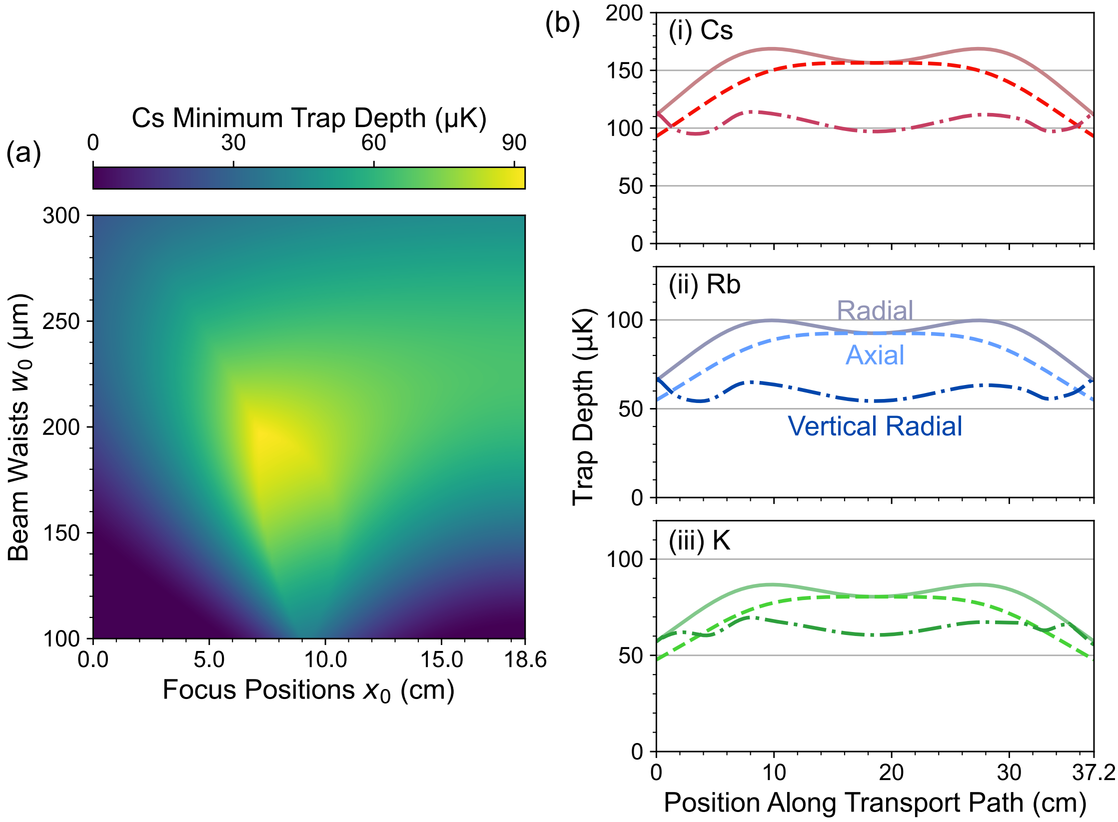

Figure 2.17: Optimising for the axial depth and vertical radial depth including levitation. (a) Shows a contour plot of the minimum trap depth for a range of focus positions and beam waists. Both the axial and vertical trap depths are considered. (b) Shows the variation of the trap depth for all three species with position along the transport path with the optimum beam parameters of $x_0 = 7.2$cm and $w_0 = 195\mu$m. The current through the MOT Chamber and Science Cell coils are set to give gradient fields that exactly compensate gravity for each species respectively.

and grey shaded region. Also shown is the variation in the horizontal radial trap depth along the transport path for the same beam parameters, which show greater the variation in minimum trap depth seen previously.

With the equations above, best achievable axial trap depth for any given species and beam powers can easily be calculated. This sets the upper limit on minimum overall trap depth achievable when compensating against gravity with magnetic levitation, which is considered in the next section.

### 2.5.3 Optimise with Levitation

With the insight gained into the axial trap depth, we now turn to re-optimising the vertical radial trap depth with magnetic levitation. As before $x_0$ and $w_0$ are varied and for each pair of values, the minimum trap depth is found. Unlike the optimisation without magnetic levitation, the trap depth across the entire transport path needs to be calculated. This is because the minimum trap depth may no longer occur at the edges or the centre of the transport path, as seen in Section 2.4.1. As before, the optimisation is performed for Cs, with the currents in the quadrupole coils set such that they produce the 31.1G/cm required to fully levitate Cs at the centre of the MOT Chamber and the Science Cell. Similarly the current through the bias coils is set to produce an offset field of 22G.

Figure 2.17(a) shows the resulting optimisation contour for Cs, again with yellow/bright regions signifying deeper traps and blue/dark regions shallow traps to no trap. Unlike previous optimisations, in this case both the axial and vertical radial trap depths were calculated throughout the transport path, and the global minimum of the two taken, resulting in a somewhat more complex optimisation contour. As before there are ridges where the trap depth between two or more points is equal. For waists above 200$\mu$m and focus positions below 7cm, the ridge occurs for beam parameters at which the vertical trap depth at the centre is equal to the depth at the trap depth minimum due to the drop-off in gradient field, close to the edge. For waists below 200$\mu$m the ridge splits in two. The ridge at smaller focus positions corresponding to equal trap depth between the central vertical trap depth and the axial depth at the edge, whereas the ridge at larger focus positions corresponds to equal trap depth between the central vertical trap depth and the local vertical depth minimum.

From these calculations, the new optimum beam parameters were found to be $x_0 = 7.2$cm and $w_0 = 195$cm. A larger value of $x_0$ can be understood intuitively, as the coils give rise to deeper traps close to the edges but do not affect the trap depths closer to the centre. The larger waist, at this increased value of $x_0$, ensures that the axial depth minimum remains close to its maximum, as calculated in Section 2.5.2.

The trap depths resulting from the new optimum are shown in Figure 2.17(b) for all three species. For each species the appropriate levitation gradient was used, see Section 2.3.5. The effect of using a different levitation gradient for each species is presented in Section 2.5.4. The minimum trap depths achieved are now 91.8$\mu$K for Cs, 51.9$\mu$K for Rb and 47.5$\mu$K for K. For Cs and Rb the minimum axial depth and the minimum vertical radial depth are almost identical with the axial slightly lower for Cs: 91.8$\mu$K compared to 93.4$\mu$K, but with the vertical radial slightly lower for Rb: 51.9$\mu$K compared to 52.5$\mu$K. For K on the other hand, the axial depth is by far the limiting depth: 47.5$\mu$K compared to 57.0$\mu$K. The reason for this is twofold, firstly K is much lighter than Cs and Rb leading to a smaller gravitational trap depth reduction and secondly due to its lower levitation gradient of 11G/cm. The latter means that the drop-off in gradient field away from the centre of the coils is less severe, as can be seen in Figure 2.9. In fact this drop off is slow enough that for the the first few cm (and last few cm) the trap depth *increases* when moving away from the coils' centre, as the intensity increase from moving closer to the focus position outcompetes the gradient field drop-off.

For the purposes of our implementation of optical conveyor-belt transport, further trap depth optimisation is not necessary for Cs or Rb. As will be shown later, using these beam parameters combined with magnetic levitation is sufficient. Moreover the axial depth is limiting (or nearly limiting) for all species and the minimum axial depth is close to the maximum achievable, as found in Section 2.5.2. Further optimisation past this point would therefore yield only slight increases in minimum trap depth.

### 2.5.4 Comparing Species

The calculations in Section 2.5.1 and Section 2.5.3 that gave the optimisation contours for Cs were re-done for both Rb and K. Figure 2.18 summarises the result with the contours enclosing the parameter space that yields a minimum trap depth above 98% (solid lines), 90% (dashed lines) and 75% (dotted lines) of the maximum achievable for that optimisation. Plots are shown both for the radial optimisation in panel (i) and the levitated optimisation in panel (ii). As the only difference between the species relevant to the axial optimisation is the polarisability, the contours for

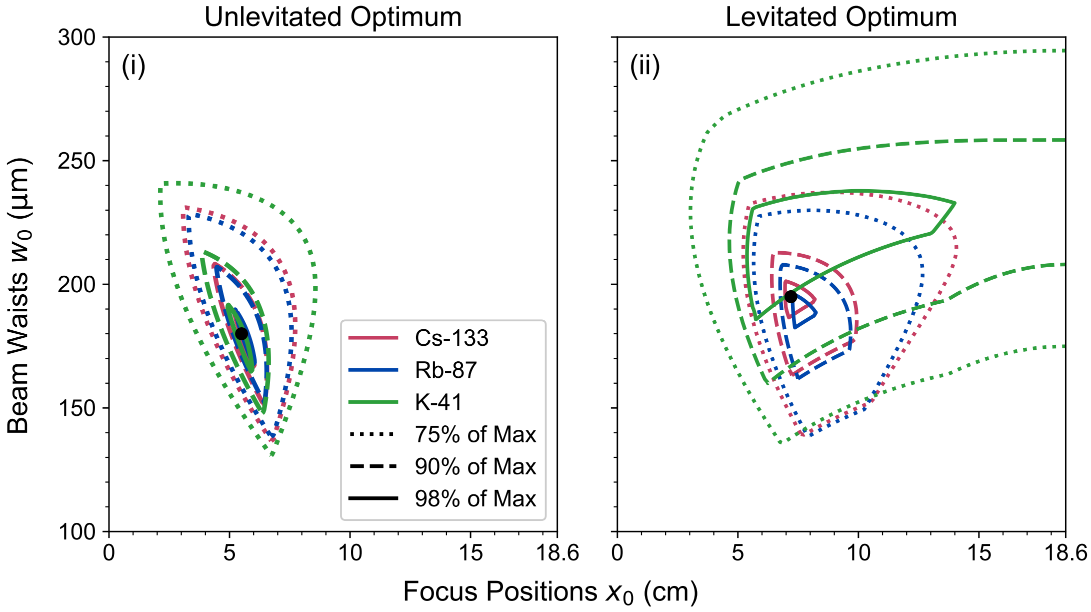

Figure 2.18: Comparing optima of Cs, Rb and K with contours for the three species shown in red, blue and green respectively. Panel (i) shows the optimisation without levitation, while panel (ii) take it into account. The optimum values of focus positions and beam waists are show with the black circles. Contours enclose the region where the minimum trap depth is at least 98% (solid lines), 90% (dashed lines) and 75% (dotted lines) of the maximum trap depth. Both axial and radial vertical trap depths are calculated.

all three species are identical.

For the optimisation without levitation differences between the three species are minimal, with all three contour having the same shape and a common optimum. The only difference evident is that, especially for the 75% contour, a broader range of beam parameters achieve the same trap depth for K than for Cs and Rb (and similarly for Cs compared to Rb). This can be explained entirely due to the difference in gravitational tilt shown in Figure 2.8.

On the other hand the levitated optimisation contours are noticeably different. For K the contours enclose a greater parameter space and shifted towards larger waists than the contours for Cs and Rb. This is due to the axial depth being limiting for K, as was found in Section 2.5.3. Its contour therefore mostly follows the axial ridge described by Equation 2.74, which explains its larger extent and location. The differences between the Cs and Rb contours are more subtle, with both having the same shape, but with slight shifts relative to each other. These shifts are due to difference in gravitational tilt, which changes at which points the axial trap depth is below the vertical trap depth. Despite these differences, it is still possible to find a pair of values of the beam waists and focus positions that give at least 98% of the maximum trap depth for each species. These are $x_0 = 7.2\text{cm}$ and $w_0 = 195\mu\text{m}$, indicated by the black dot and the values found previously. A difference between the species which is less easily overcome is that of the different required gradient field.

### Choosing Gradient Field

One significant difference between the three species is the different magnetic gradients they require for levitation. While the Cs and Rb levitation gradients are very similar at 31.1G/cm and 30.6G/cm respectively, the K levitation is far lower at 11G/cm. This lower gradient field is beneficial when dealing with K on its own as it means a larger effective coil range. However if K is to be transported at the same time as Cs or Rb, it poses a challenge, which is illustrated in Figure 2.19. The trap depths for all three species are shown using the optimum beam waist and focus positions found previously, Section 2.5.3 and Section 2.5.1. Shown is the vertical trap

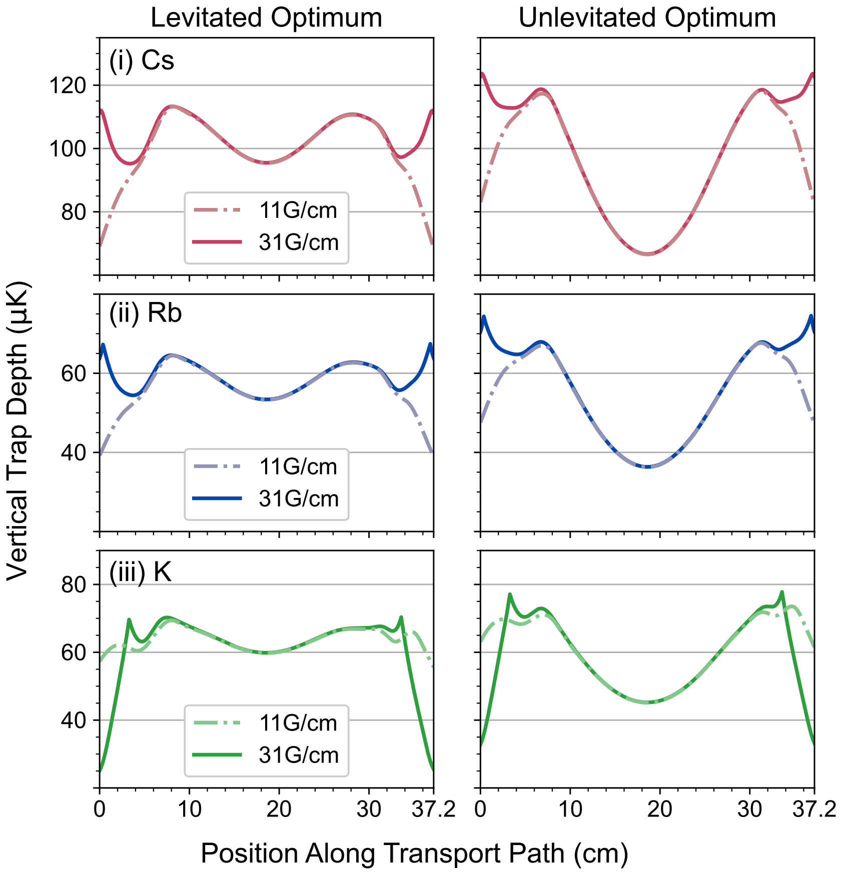

Figure 2.19: Comparing the vertical trap depth of Cs, Rb and K for two different central magnetic levitation gradients, 11G/cm (dash-dotted lines) and 31G/cm (solid lines). The former fully levitates K while the latter fully levitates Cs and Rb. The variation of the vertical trap depth along the transport path for the levitated optimum beam parameters, $x_0 = 7.2$cm and $w_0 = 195\mu$m, and the unlevitated optimum, $x_0 = 5.5$cm and $w_0 = 180\mu$m.

depth for two different gradient fields: 31G/cm to levitate Cs (and Rb) in dark solid lines and 11G/cm to levitate K in light dash-dotted. For the sake of comparison, both the beam shapes for the levitated and unlevitated optima are included.

For Cs and Rb, the lower gradient field of 11G/cm leads to significantly reduced vertical trap depth at the transport path edges as can be expected. The Cs minimum vertical depth is reduced from 93.6$\mu$K to 67.1$\mu$K, while for Rb the minimum depth is reduced from 51.8$\mu$K to 37.2$\mu$K. While these depths are still greater than those achieved with the unlevitated optimum beam shapes (even with the gradient field added), the reduction is nonetheless significant.

The inverse problem exists for K for the 31G/cm gradient field. As the gradient field exceeds that required to counteract gravity, the atoms are *over-levitated* with the trap tilted in the opposite direction. This has the same effect on the depth as an insufficient gradient field, with the minimum trap depth reduced from 56.9$\mu$K to 24.8$\mu$K. In the over-levitated case for K, there appear to be sharp, discontinuous changes in the trap depth, which are explained in the next section.

While the transport of K, and so also the transport of K with Cs or Rb, is outside the scope of this work, there are some possible ways of overcoming this challenge. One way to remedy this difference would be to pick a compromise gradient field, say $\sim$ 20G/cm, which is not ideal for any species but not catastrophic either. The dependence of the K levitation gradient on the magnetic offset field (see Section 2.3.5) could then also be accounted for. In such a case, the beam waists and focus positions could be re-optimised at the new gradient field.

Here too a compromise may need to be found between the K depths and Rb/Cs depths, possibly taking into account the atom number and temperature of each species achievable in the MOT Chamber. Alternatively, the problem could be circumvented by transporting K and Cs/Rb sequentially rather than simultaneously. This however would likely require a more complex set of dipole trap in the MOT Chamber and/or the Science Cell to implement.

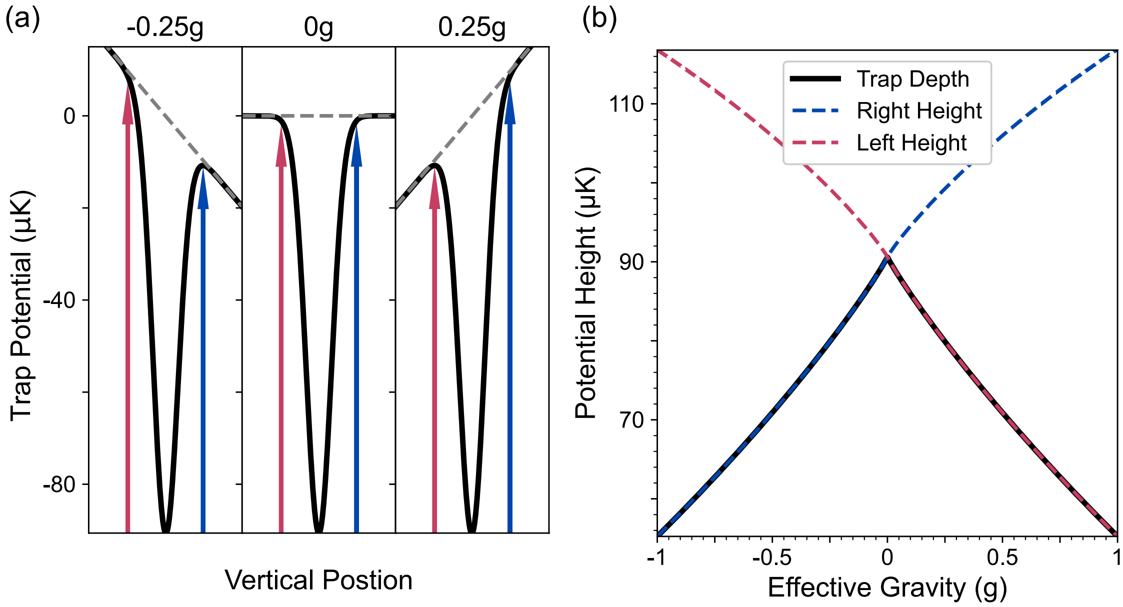

Figure 2.20: Origin of the discontinuity in vertical trap depth when over-levitating the atoms. (a) Shows the trap local maximum in the potential moving from one side of the local minimum to the other as the gradient crosses through the levitation gradient. The “height” of the potential on either side of the local minimum is indicated by the red and blue arrows. (b) Shows a plot of the height of the potential on the left (dashed red line) and right (dashed blue line) of the local minimum. The trap depth (solid black line) is then defined as the minimum of those two lines.

### Over-levitation subtlety

In cases where the atoms are over-levitated, where the central gradient field exceeds that needed to levitate the atoms, a discontinuity will appear in trap depth calculated when moving away from the coils' axis. While healthy suspicion towards such discontinuities is usually correct, in this case there is a physical reason for its existence. The discontinuity will occur exactly at the point where the gradient field crosses the levitation gradients and the atoms go from being over-levitated to under-levitated, and is shown in Figure 2.20. In the fully levitated case, or equivalently for the horizontal radial trap depth, the trap depth is given simply by the potential minimum's distance from the background, which we take to be equal to zero. Meanwhile, in both the under-levitated and over-levitated cases, there exists a local maximum in the potential which is below zero. The trap depth is thus defined as the difference between the local maximum and local minimum. For the over-levitated case (negative effective gravity) the local maximum occurs on the *right* of the local minimum, at larger z. On the other hand, for the under-levitated case (positive effective gravity) the local maximum occurs on the *left* of the local minimum, at smaller z. Therefore when the gradient field crosses between over-levitated to under-levitated, position where the local maximum discontinuously moves from the right to the the left of the local minimum, similarly giving rise to a discontinuous trap depth.

This can be further illustrated by considering the "height" of the potential an equal distance from either side of the local minimum, shown by the red and blue arrows in Figure 2.20(a). Plotting the height of the left and right side of the potential, Figure 2.20(b) shows two nearly straight lines with opposite sign gradients. For effective gravity, the trap depth is defined as the minimum of these two heights. The discontinuity occurs at the point where the two lines cross. The fact that these height of the potential is not a straight line with effective gravity is due to the Gaussian shape of the optical trapping potential and the location of the maximum changing with effective gravity.

|  |  | Simplest Case (Section 2.4) | Unlevitated (Section 2.5.1) | Levitated (Section 2.5.3) |
|---|---|---|---|---|
| Beam Parameters | $x_0$ (cm) | 18.6 | 5.5 | 7.2 |
|  | $w_0$ ($\mu$m) | 250 | 180 | 195 |
| Minimum Radial Depth | Cs | 30.5 | 66.5 | 95.3 |
|  | Rb | 15.2 | 36.3 | 53.4 |
|  | K | 26.3 | 43.8 | 55.7 |
| Minimum Axial Depth | Cs | 95.1 | 92.6 | 92.9 |
|  | Rb | 56.2 | 54.7 | 54.9 |
|  | K | 48.9 | 47.6 | 47.7 |

Table 2.3: Table summarising the beam waist and focus positions found to be optimum for each optimisation performed, and the minimum trap depths achieved for each species.

## 2.6 The Summary: Comparing Optima

The results of the calculations above are summarised in Figure 2.21. Initially two beams focused in the centre of the transport path were considered and their waist optimised, dotted blue-grey line in Figure 2.21(b). Adding in symmetric offset between the two beams yielded significantly increased minimum trap depth for all three species, dashed green line. The axial trap depth, due to its simpler mathematical form can be understood mathematically and it was found that a range of beam waists and focus positions pairs yield the same optimised axial trap depth. With this insight, the vertical trap depth was re-optimised, this time considering both magnetic levitation and the axial depth, solid blue line. After this optimisation it was found that the axial depth was limiting for Cs and K and very close to limiting for Rb, meaning that no further increases in the trap depth minimum could be gained with the current setup. The beam waist, focus positions and minimum trap depth values are summarised in Table 2.3.

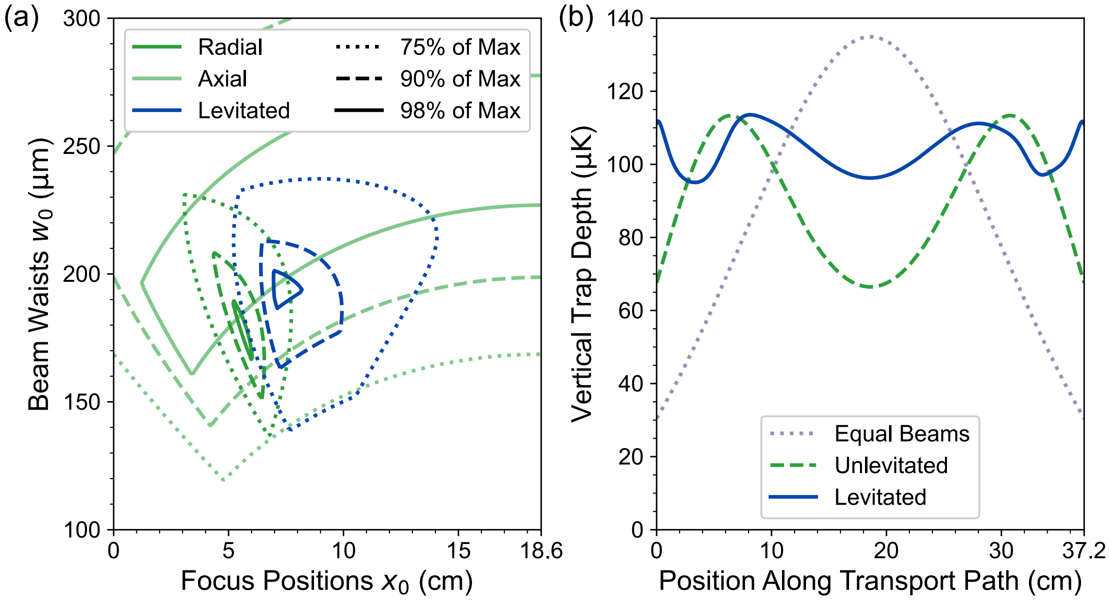

Figure 2.21: Comparing optima from different optimisations. (a) Shows the regions of the parameter space that optimise for vertical depth without levitation (green), axial depth (light green) and combined axial and vertical depth with levitation and axial. The lines enclose the regions where the minimum potential depth is at least 98% (solid lines), 90% (dashed lines) and 75% (dotted line) of the optimum minimum depth for that optimisation. (b) Shows the vertical trap depth along the transport path for three different optimisations: the basic configuration with equal identical beam shapes (blue-grey dotted line), symmetrical beams without levitation (green dashed line) and symmetrical beams including levitation.

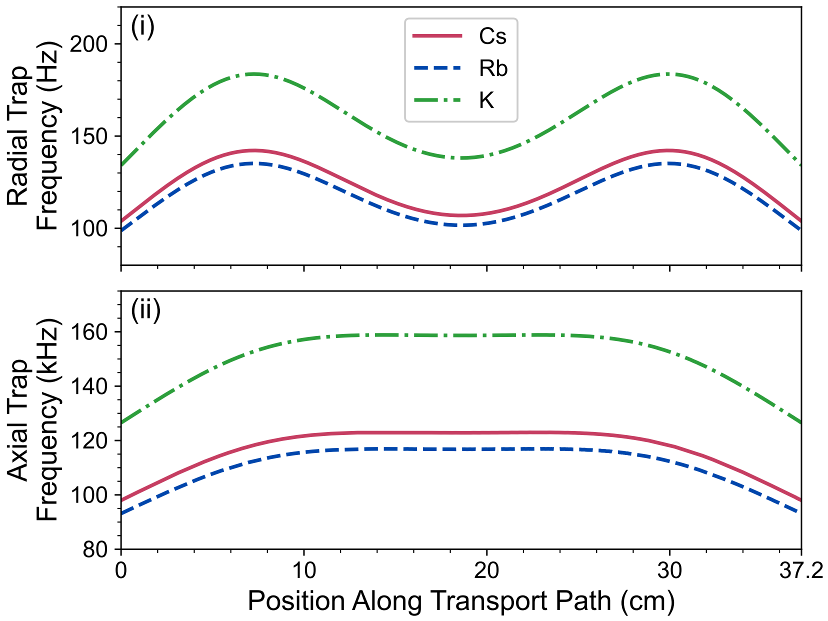

Figure 2.22: Variation of the predicted trap frequencies along the transport in the (i) radial direction and (ii) axial direction. Note that the radial frequencies are in Hz and the axial frequencies are in kHz. Cs is shown in the solid red line, Rb in the dashed blue line and K in the dash-dotted green line. The calculations are performed for the optimum beam parameters with levitation, $x_0 = 7.2$cm and $w_0 = 195\mu$m, and 1064nm light with 18W per beam.

## 2.7 Trap Frequencies

The predicted trap frequencies along the axis of the optical conveyor-belt are shown in Figure 2.22, in both the axial and the radial directions for all three species. They are calculated for the optimum beam parameters with levitation, $x_0 = 7.2$cm and $w_0 = 195\mu$m. For each point along the transport path, the trap frequencies are found by fitting a quadratic around the local minimum in the trapping potential in each direction. An equation of the form

$$U_{\mathrm{harmonic}} = \frac{1}{2}m\omega^2(y - y_0)^2, \tag{2.80}$$

is used where $m$ is the mass of the atom, $\omega$ is the angular trap frequency, $y$ is the coordinate along the appropriate axis and $y_0$ is the position of the local minimum in the trap potential. Using $\omega = 2\pi f$, the (ordinary, non-angular) trap frequency is then found. A quadratic fit to the potential is used to find the trap frequencies rather than a quadratic approximation of the potential, as in [135], due to the difficulty in defining a beam size when the lattice is formed from two beams with different focus positions.

The variation in trap frequency is approximately ±20% in the radial direction and ±10% axially for all three species. The differences between the species are due to the different polarisability-to-mass ratios. The high axial trap frequencies of $\sim 110$kHz for Rb and Cs allow fast accelerations of the atoms. For both Rb and Cs accelerations up to 38km/s$^2$ are possible, above which the axial trap depth is reduced to zero due to the accelerational tilting of the axial potential, see Section 4.1.4. It is anticipated that changes in the trap frequency over the course of the transport could cause parametric heating [114] if the time scale for the change approaches $(2f_{\mathrm{rad}})^{-1} \sim 5$ms. This would lead to a drop of transport efficiency at very high speeds. However the transport durations are limited to 14.9ms by the maximum detuning of the frequency control setup and, as shown in Section 4.1.5.

# CHAPTER 3

# Transport Setup

In this chapter the experimental setup is presented and discussed. Section 3.1 gives a brief overview of techniques used to prepare samples of cold atoms in the MOT chamber. Section 3.2 gives the details of the optical setup used for transport.

## 3.1 Preparation of Atoms in the MOT Chamber

This section briefly outlines the techniques used to cool Rb and Cs atoms. More detail can be found in the theses of Andrew Innes [154] and Jonathan Mortlock [155], as well as in [133]. Details of the cooling procedure for K can also be found in [154].

A schematic of the vacuum apparatus and the optical setup for cooling, trapping and transporting the atoms is show in Figure 3.1. Atomic samples are prepared in a 12-port stainless steel vacuum chamber, the MOT chamber. The experiment employs 2D$^+$ magneto-optical traps (MOTs) [156] as atomic sources. Two separate glass cell house atomic dispensers, one for Cs and one for Rb, situated on opposite sides of the MOT chamber. A push beam is used to provide a high-flux of atoms into the MOT chamber from the glass cells and the 2D$^+$ MOTs provide transverse cooling and confinement of the beams. Some of the push beam light is retro-reflected and

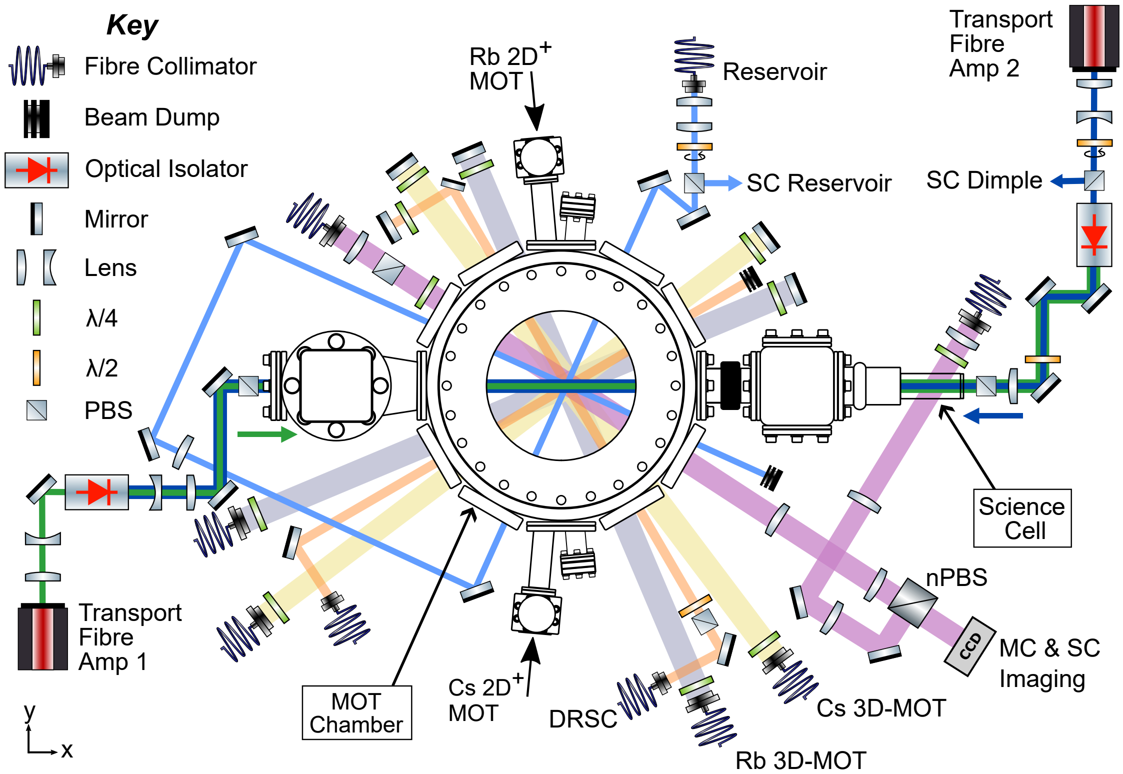

Figure 3.1: Schematic overview of the experimental apparatus. The vacuum apparatus and optical layout used to cool, trap, transport and image Rb and Cs atoms are shown. The transport beams are aligned to be overlapped and counter-propagating along $x$, the axis between the two chambers. Electromagnetic coils used to generate bias and gradient magnetic fields sit above and below both chambers, but are omitted for clarity. Similarly, the MOT and DRSC beams propagating through the MOT chamber in the $z$ direction are also omitted.

used as a slowing beam, providing some slowing along the third spatial dimension[1]

Atoms are loaded into the 3D MOT in the centre of the MOT Chamber from the two atomic beams. Separate optical fibres and beam paths are used for Rb and Cs. However light for the 3D MOT of K uses the same fibre and beam paths as Rb. As the $D_2$ lines for the two species are very similar, at 780nm for Rb and 766nm for K, this can be done without significant losses in beam power.

The atoms then undergo further sub-Doppler cooling using an optical molasses and degenerate Raman sideband cooling (DRSC) [157] for both Rb and Cs simultaneously. This cools the atoms to $\approx 1\mu$K and spin-polarizes them into the energetically lowest Zeeman state, namely $|F = 3, m_{\mathrm{F}} = 3\rangle$ for Cs and $|F = 1, m_{\mathrm{F}} = 1\rangle$ for Rb.

Subsequently, the atoms are magnetically levitated and loaded into a large volume crossed optical dipole trap, the "reservoir trap", made from two beams with $\approx 500\mu$m waists crossing at $\approx 90°$. The beams are derived from a 50W, 1070nm broadband Ytterbium fibre laser (IPG Photonics). The beams are set up in a "bow-tie" configuration wherein the light exiting the MOT Chamber is reused for the second beam. Following a hold time of 750ms to allow the atoms to thermalise in the reservoir trap, $1.0 \times 10^7$ Cs atoms or $1.0 \times 10^7$ Rb atoms typically remain at temperatures of $3.7\mu$K and $5.6\mu$K, respectively.

The optical conveyor belt is loaded from the reservoir trap. The power in each lattice beam is controlled by a $\lambda/2$ waveplate mounted onto a rotating, hollow-core stepper motor before a polarising beam splitter (PBS) [158] and can be smoothly ramped on/off in 100ms for transfer of atoms into/out of the lattice.

Absorption imaging is used to measure the number of atoms and their spatial distribution. This can be performed in either the MOT chamber or the Science Cell using the same CCD camera, as shown in Figure 3.1.

---

[1] This cooling along the third spatial dimension is why this technique is know as a $2D^+$ MOT.

## 3.2 Transport Lattice setup

Light for the transport lattice is provided by two 1064nm fibre amplifiers (Azurlight systems), one for each lattice beam, as shown in Figure 3.1. Using two different amplifiers is central to our transport scheme. Firstly, it increases the available amount of power (see also Section 3.2.1 and Section 3.2.2) and secondly, it enables the beams shapes of each lattice beam to be set independently (see Chapter 2 and Section 3.2.3). However using two independent beams also presents some challenges. The setup is sensitive to beam pointing noise, as discussed in Section 3.2.4, and the alignment of the transport beam is challenging, as discussed in Section 3.2.5.

### 3.2.1 Maximising Beam Power

The principle limitation for optical conveyor-belts is providing sufficient trap depth throughout the transport path, as discussed in Chapter 2. As the trap depth is directly proportional to the power in the lattice beams[2], maximising the amount of power in each lattice beam is crucial. However this maximisation is not as simple as using the highest power laser system possible. In particular, the implementation of the frequency control must be carefully considered.

Optical conveyor-belt transport requires two phase coherent beams of a single, controllable frequency. They must each be phase coherent to produce a lattice and single frequency to avoid creating multiple moving lattices with different speeds. Thus the two beams must have a common source. Additionally, the conveyor-belt must be stationary at the beginning and end of transport to enable efficient loading into and out of the lattice. Hence the two beams must have zero frequency detuning at the end points of the transport sequence. To transport the atoms with minimal loss, the frequency detuning must be ramped on and off smoothly. An acousto-optical modulator (AOM) is ideal for this application as it gives precise frequency control and the various diffracted orders are spatially separated according to their frequency, allowing only the desired frequency to be used and the rest discarded [159].

---

[2] This is a slight oversimplification as it is only true in cases, such as ours, where there is equal power in both beams. If there are significantly different powers in the two beams the dependence on power becomes more complicated.

However due to their finite bandwidth, a pair of AOMs must be used to enable smooth ramping of the detuning. Additionally, to avoid beam-pointing deflection with frequency, the AOMs must be double passed [160], requiring a total of four AOM passes. Even with high diffraction efficiencies into the desired order of 85% this constitutes a significant loss of power. Additionally, the diffraction efficiency of the AOMs decreases as the RF frequency supplied to the AOMs is shifted away from the AOM centre frequency.

For our implementation of optical conveyor-belt transport, we use two fibre amplifiers seeded from a common source to ensure phase coherence. Inspired by [128], both AOMs are placed in the seed path (see Section 3.2.2 and Figure 3.2 for more details). As long as a minimum power of 10mW is coupled into each fibre amplifier, they will output 30W. Hence, as long as there is sufficient power in the seed path, this configuration eliminates all losses in power on the atoms associated with the AOMs. A more detailed discussion of different transport configurations is found in Appendix B.

Our fibre amplifiers have a maximum output power of 30W. However due to the various optical components required, 20(1)W of light is incident onto the atoms. Losses are mainly due to the optical isolator and a pair of polarising beam splitters in each beam path, see Figure 3.1. The isolators prevent light, both from the other amplifier and due to back reflections, from entering back into the fibre amplifier and thereby causing damage to it. The pair of beam splitters are used in conjunction with a $\lambda/2$ waveplate attached to a rotation mount to dynamically switch light between the transport and the Science Cell dipole trap beam paths.

### 3.2.2 Transport Seed Setup

A schematic of the optical setup used to seed the fibre amplifier and control the relative frequency between the two lattice beams is shown in Figure 3.2(a). The seed light is provided by a 1064nm Mephisto-NPRO laser (InnoLight, Coherent) with a maximum power of 2W. Light is split off for each amplifier using a pair of $\lambda/2$ waveplates and polarising beam splitters (PBS). One AOM (Isomet M1080-T80L) is placed in each path and aligned such that both branches use the -1$^{\text{st}}$ diffraction

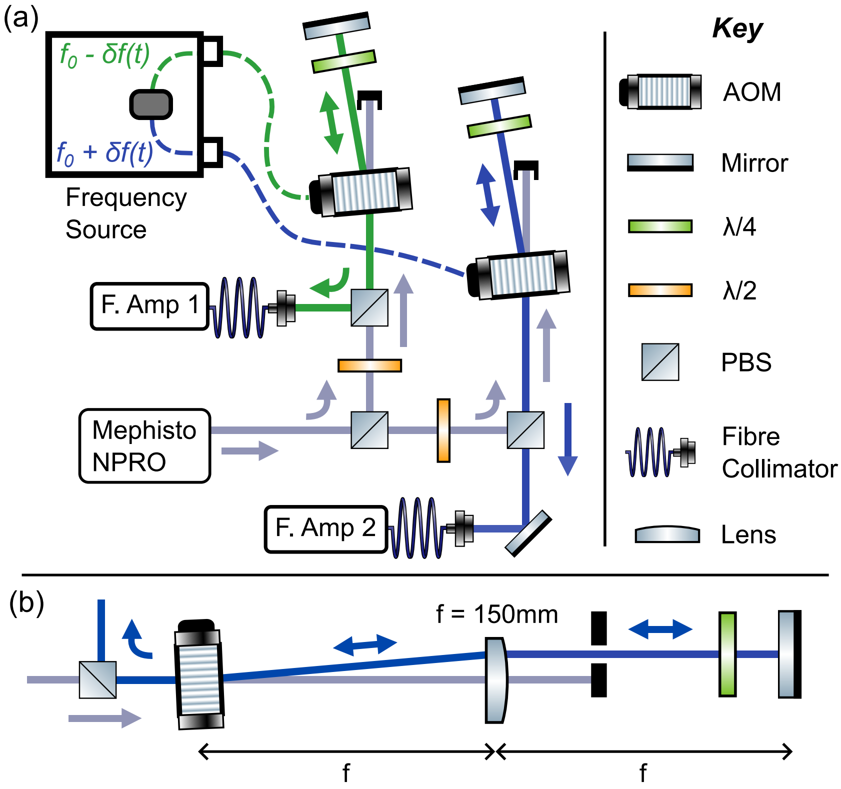

Figure 3.2: Schematic of the seed setup for the fibre amplifiers. (a) Shows the optical setup of the seed path. Two double-passed passed AOMs are used to control he frequency difference between the light seeding the amplifiers. Note that the AOMs are aligned to the -1$^{st}$ order and hence a decrease in the RF modulation frequency will result in an increase in the frequency of the diffracted light and vice versa. (b) A more detailed schematic of optics used to double-pass the AOMs. The lens and mirror in a "cat's-eye" configuration, described in detail in the main text. Different frequencies of light are shown in different colours.

order. The AOMs are set up in a double-pass configuration [160], meaning light is retro-reflected back through each AOM after the initial pass to be diffracted a second time. Both AOMs are operated at the same centre frequency $f_0 = 75$MHz. A time-dependent frequency shift $\delta f(t)$ is applied to both modulation frequencies simultaneously, but with opposite signs. As the AOMs are aligned to diffract light into the -1$^{\text{st}}$ diffraction order, the RF modulation frequency is *subtracted* from the frequency of the light, giving $f_{\text{final}} = f_{\text{initial}} - 2f_{\text{AOM}}$ for each branch. Hence the total relative lattice detuning is given by

$$\Delta f(t) = -4\delta f(t). \tag{3.1}$$

A $\lambda/4$ waveplate is placed before the retro-reflecting mirror which allows the diffracted beam to be separated from the initial beam using a PBS and subsequently coupled into an optical fibre. The beam path that seeds fibre amplifier 1 uses an additional $\lambda/2$ waveplate and PBS to ensure that no light from the fibre amplifier 2 path can enter fibre amplifier 1. When the optics were first set up, this additional PBS was not in place. Instead, light was coupled into fibre amplifier 1 from the transmission back through the first PBS (as is done for fibre amplifier 2). A small amount of light, the fraction that was still vertically polarised after the $\lambda/4$ waveplate was reflected by other two beam splitters and coupled into the optical fibre of amplifier 1. Thus, when the frequencies of the two AOMs was detuned, light of two different frequencies was entering the fibre amplifier. This resulted in a modulation of the fibre amplifier output power and enhanced atoms loss.

Operating the AOMs in a double-pass configuration ensures that the beam pointing of the diffracted beam does not vary with the AOM frequency [160]. Thus the coupling efficiency into the seed fibres remains constant with AOM frequency. However, operating the AOMs away from their centre frequency does still lead to a reduced diffraction efficiency into the -1$^{\text{st}}$ order. In order for the fibre amplifiers to operate, a minimum seed power of 10mW is required. The efficiency drop-off with frequency, along with the amount of power in each beam path, limits the maximum detuning achievable between the lattice beams. This, in turn, determines the maximum lattice velocity and hence the minimum transport duration.

The double-pass AOM is implemented using a "cat's eye" retro-reflector [161], see Figure 3.2(b). It consists of a lens and a mirror separated by a distance equal to the focal length of the lens $f = 150\text{mm}$. This focuses the beam onto the mirror and hence ensures that the size of the beam on the second pass matches the beams size on the first past. This avoids the beam clipping on the aperture of the AOM and hence maximises the overall diffraction efficiency. The distance between the AOM and the lens is also set to be equal to the focal length of the lens and the lens is centred on the $0^{\text{th}}$ (non-diffracted) order. The lens therefore parallelises the $-1^{\text{st}}$ order relative to the $0^{\text{th}}$ order regardless of the AOM frequency. This ensures that, after retro-reflection, the beam is sent back along the same beam path as the incident light and hence the angular shift with AOM frequency is avoided. An alternative to the cat's eye retro-reflector is to place the AOM at the focus of a 1:1 telescope formed by two converging lenses of equal focal length and separated by twice the focal length [160]. However, this scheme requires an additional optic and more space. Additionally, in the telescope configuration the AOMs are placed at the focus of the beam, whereas our AOMs diffract more efficiently at larger beam sizes. Hence the cat's eye configuration was preferred. The overall double-pass efficiency is 65(1)% for both branches.

If the atoms are only transported from the MOT Chamber to the Science cell, each AOM is only shifted in one direction, $\delta f$ is positive as defined in Figure 3.2(a). On the other hand, if round-trip transport is performed, the frequency shift $\delta f$ is both positive and negative for both AOMs. Adjusting the alignment of the AOMs relative to the incident beam adjusts the range of frequencies over which the AOMs diffract efficiently. Hence, in the scenario where only one-way transport is required the AOMs can be aligned to enable a large detuning of up to $\Delta f = 103\text{MHz}$. For two-way transport, where the AOM frequency shifts are symmetrical, the maximum achievable detuning was $\Delta f = \pm 82\text{MHz}$

To control the AOM frequencies, a direct digital synthesiser (DDS) dual-frequency generator (MOGLabs ARF) is used. More details on the setup and characterisation of the DDS are given in [155]. The DDS has two phase synchronized outputs,

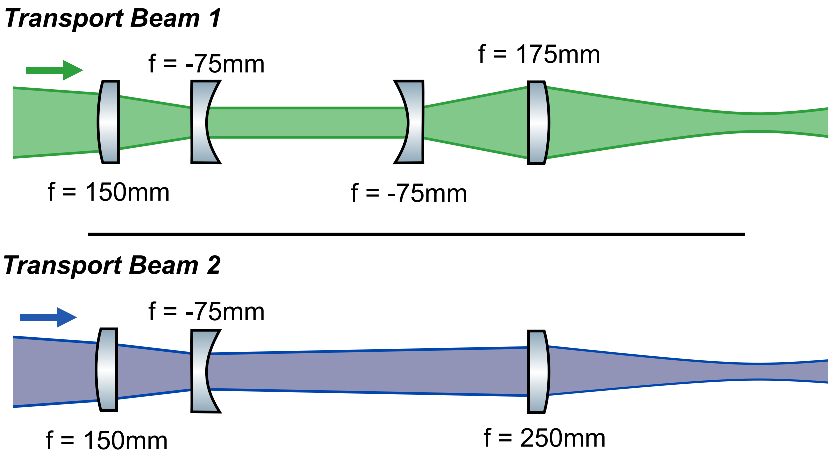

Figure 3.3: Schematic of the lenses used to control the beam shape of the two transport beams. Both beam paths have a telescope to shape the beam out of the fibre amplifier laser heads. A second pair of lenses is used to shape the beam to the required size and focus position for transport beam 1 while a single focussing lens is sufficient for transport beam 2.

which is crucial as relative phase noise around the lattice trap frequencies leads to heating [128, 162]. The memory size is of 8191 instructions which limits the AOM frequency update rate. For longer ramps, the update rate becomes comparable to the axial trap frequency, which is known to cause heating [61], see Section 4.1.5.

### 3.2.3 Beam Focussing

As described in Chapter 2, and specifically Section 2.5.3, the desired beam parameters for the lattice beams are a waist of 195$\mu$m and with transport beam 1 (transport beam 2) focussed 7.2cm from the MOT Chamber (Science Cell). The configuration of lenses used to achieve these beam shapes are shown in Figure 3.3. The beams out of the fibre amplifier laser heads are converging, measured to be focussing to a waist of 410(5)$\mu$m at a distance of 1.40(5)m from the laser head. For both transport beams, a telescope consisting of lenses with focal lengths 150mm and $-75$mm is used to reduce the beam size and (approximately) collimate the beams. This avoids any clipping of the beams on the apertures of the optical isolators in each beam path, see Figure 3.1. In an earlier implementation an additional AOM was placed in each beam path for fast switching of the beam power. This was later replaced by a waveplate mounted onto a hollow-core stepper motor and a PBS [158], as well as a high-power shutter. Subsequently, the beams are focused to the required 195$\mu$m waist using a pair of lenses for transport beam 1 and a single lens for transport beam 2. An additional lens had to be used for transport beam 1 due to the longer optical path length between the desired focus position and the end of the vacuum chamber, as can be seen in Figure 3.1.

The lenses for the transport beams were initially aligned to give the target beam profile, as measured by deflecting the beams onto a different path before the vacuum chamber. Typical uncertainties were $\approx 10\mu$m for the waist and $\approx$ 1cm for the focus position. The beams out of the fibre amplifiers had slightly elliptical profiles and showed some astigmatism. As a consequence, it was not possible to exactly match the desired beam sizes in both axes. Thus after the two transport beams were aligned and overlapped with each other, the lens positions were adjusted to maximise the measured transport efficiency.

### 3.2.4 Pointing Stability

The beam pointing stability is of great importance for any optical transport scheme but especially for our optical conveyor-belt transport [163, 164]. Drifts in the beam pointing over time can lead to drifts in the final position of the atoms. This in turn could lead to fluctuations in, for example, the number of atoms subsequently captured in trap and hence a decline in the performance of the transport. Beam pointing fluctuations can also lead to direct loss during transport. This is a concern particularly for optical conveyor-belts as any drifts comparable to the size of the beam waist would lead to significant reductions in trap depth. For schemes such as ours with two independent lattice beams are susceptible to drifts as they are not "self-correcting" in the way, say, a scheme using a retro-reflected lattice would be[3].

For both fibre amplifiers used for transport, the beam stability was measured using a CCD camera (Thorlabs DCC1545M) as shown in Figure 3.4. The measurement was performed with the amplifiers at full power and the beams attenuated

---

[3] This assumes the use of a re-collimating lens before the retro mirror

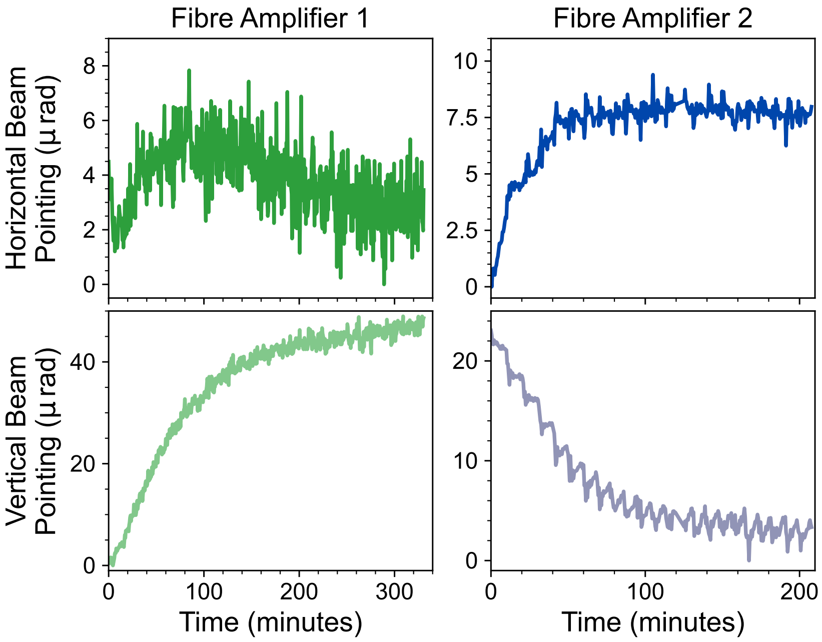

Figure 3.4: Warm-up behaviour of the fibre amplifiers. Variation of the beam pointing of the two transport fibre amplifiers is measured over time after turn-on and split into a horizontal component (top panels) and vertical component (bottom panels). Data for fibre amplifier 1 is shown on the left (green), data for fibre amplifier 2 is shown on the right (blue).

to avoid damaging the camera. This was done by using a pair of glass blanks for fibre amplifier 2 and the light transmitted through a back-polished mirror for fibre amplifier 1[4]. Images were taken at an interval of 30s for at least three hours. Each image was fitted to a Gaussian profile to extract the centre point of the beam. The variation in beam position was then converted into an angular pointing deviation by dividing by the optical path length between the laser head and the camera, equal to 1.5m and 2.4m for amplifier 1 and amplifier 2 respectively.

Both lattice beams exhibit a significant beam pointing drift over time when the amplifiers are switched on. This behaviour is associated with the fibre amplifiers warming up over a timescale of approximately two hours. The output power of the fibre amplifiers shows fluctuations over a similar timescale, as specified and measured by the manufacturer. The drifts in position were found to be consistent day-to-day. As a part of the daily experimental protocol, the fibre amplifiers are given appropriate time to settle before being used. After the warm-up period, the beam pointing is stable to $4\,\mu$rad, which corresponds to a drift of no more than $7\mu$m at the focus of the beam. The beam pointing exhibits an oscillatory behaviour, most clearly visible in the data for fibre amplifier 2. This oscillation has a period of approximately 10 minutes and was correlated to the air conditioning cycle of the lab. A beam pointing measurement was performed using light from the Mephisto NPRO coupled into an optical fibre and similar oscillatory behaviour was observed. Hence the oscillations are not unique to the fibre amplifiers and are likely due to variations in temperature and/or pressure affecting the optical path used for the measurement. Thus, the optomechanical components used for the final transport beam path were selected to maximise the passive stability of the setup.

### 3.2.5 Beam Alignment

The alignment of the two transport beams presented a challenge when first implementing transport. Both beams must be well overlapped throughout the transport

---

[4] A PBS and $\lambda/2$ waveplate could also be used to attenuate the beam. However this was found to give a poorer-quality attenuated beam with scattered light forming a greater fraction of the transmitted light.

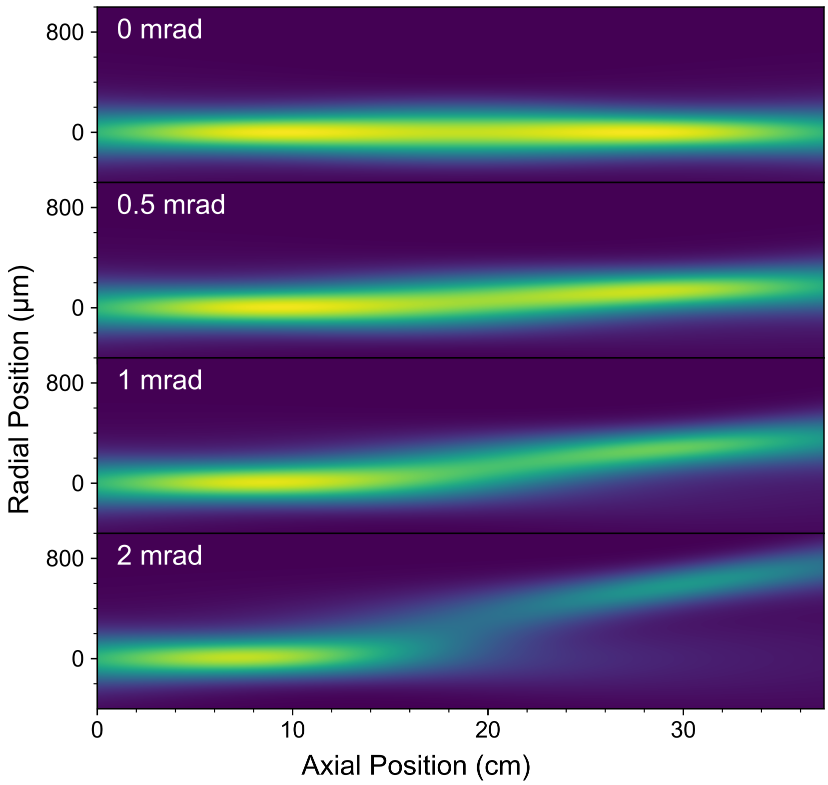

Figure 3.5: Radial trapping potential with the addition of an angular offset between the two lattice beams. The beam are taken to be overlapped in the MOT chamber and the angle of transport beam 2 is varied in the horizontal plane. Yellow regions shows regions with a deep trapping potential, while blue shows regions with a shallow or no trapping potential. For clarity the sinusoidal variation in the potential along the axial direction has been omitted.

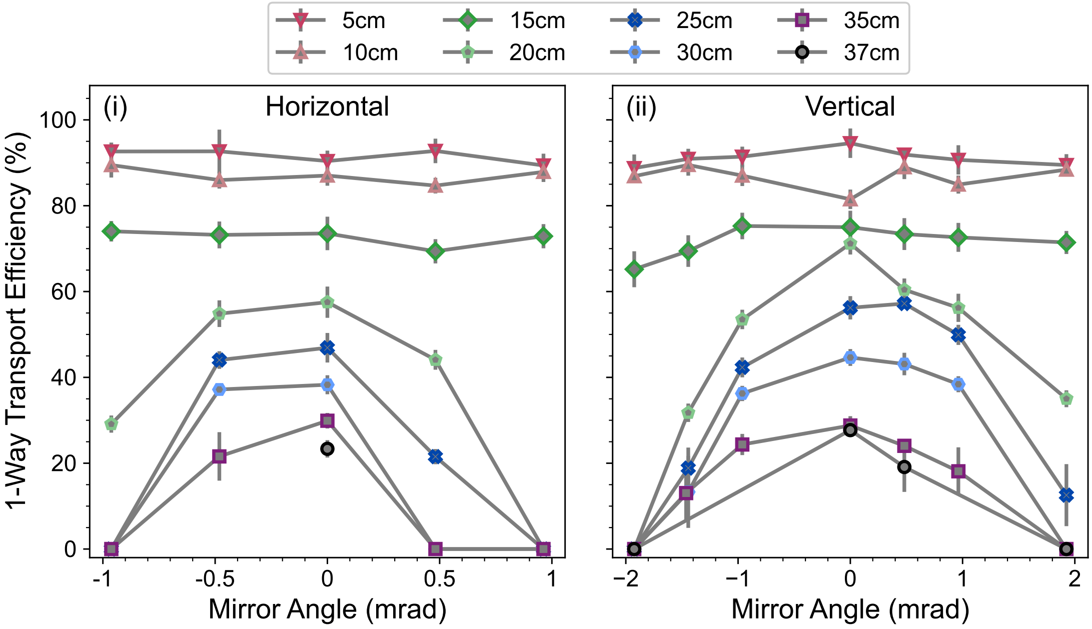

Figure 3.6: Alignment of the two transport lattice beams. The effective one-way transport efficiency measured as a function of mirror angle in (i) the horizontal direction and (ii) the vertical direction. This is done for a range of transport distances, shown by different markers and colours. For all distances, round trip transport is performed and losses are assumed to be equal for both legs.

path to ensure a high trap depth. Initially, the two beams were aligned such that, by eye, they appeared to be overlapped. However this proved to be insufficiently precise. Instead the atoms were used to provide a more sensitive metric. A dipole trap can be formed by crossing each transport beam in turn with another dipole trap beam in the MOT Chamber. The number of atoms or the optical density in this improvised trap provides a quantity to maximise. While it is relatively straightforward to overlap the beams in this way, it only guarantees that the beams are well aligned in the MOT chamber. An angular separation between the two beams can still persist.

To illustrate the significance of an angular separation between the two transport beams, Figure 3.5 shows the trapping potential for a range of such angular separations. Transport beam 1 is taken to be along the transport axis of all angles. The sinusoidal variation in the trapping potential is omitted for clarity, such that the potential is given by $I_{\mathrm{max}}$ as defined in Equation 2.39. Below 15cm, the angular separations has little effect on the trapping potential. At around 20cm and above, the region of maximum intensity is noticeable raised above the transport axis. In the case of 2mrad a noticeable "splitting" of the potential occurs, coinciding with the separation of the two beam exceeding the beam size at that point.

The approach taken to fully overlap the transport beams was iterative. As can be seen in Figure 3.1, each transport beam has two mirrors before the chamber to steer the beam. The two mirrors for transport beam 1 were iteratively adjusted to ensure that the beam exited the vacuum chamber centred on the Science Cell (using the final mirror) and aligned to the atoms in the MOT Chamber (using the second-to-last mirror). Once this process was complete, transport beam 1 was taken to define the transport axis. The final mirror for transport beam 2 was then used to align the beam to the atoms in the MOT Chamber, thereby overlapping it with transport beam 1 at that point. In order to find the correct angle for the second-to-last mirror, the transport efficiency as a function of transport distance was measured for a range of the mirror's angles. At each point, the final mirror was readjusted to ensure the two transport beams were aligned in the MOT Chamber. This was repeated for both the horizontal and vertical directions and the results are shown in Figure 3.6. As imaging of the atoms is only possible in the MOT Chamber (and later in the Science Cell), the atoms were transported the desired distances before being transported back to be imaged. The one-way transport efficiency was calculated by taking the square root of the round-trip efficiency, thereby assuming that losses are symmetrical for both legs of transport. One notable feature is the very weak angular dependence of the transport distance on mirror angle for short distances. For distances of 15cm and below, the mirror angle has almost no effect on the transport efficiency. This reproduces the phenomenon seen in Figure 3.5 and described above.

Using this iterative approach, transport to the Science Cell was first achieved. This allowed the Science Cell imaging setup to be aligned and transport to be further optimised and characterised. These characterisation measurements are discussed in the next chapter.

# CHAPTER 4

---

# Transport Characterisation

---

This chapter presents the characterisation and optimisation of our transport scheme. In Section 4.1 different transport trajectories are considered and their efficacy is compared both theoretically and experimentally. Further characterisation measurements are presented in Section 4.2. Section 4.3 discusses transport of both Rb and Cs simultaneously. Finally, the production of a Bose-Einstein condensate of either Rb or Cs is presented in Section 4.4.

## 4.1 Transport Trajectories

For optical conveyor-belts, transport is realised by dynamically varying the frequency difference $\Delta f$ between the two lattice beams. This varies the velocity of the lattice according to

$$v_{\text{lattice}} = \frac{\lambda \Delta f}{2} \tag{4.1}$$

where $\lambda$ is the wavelength. In this section different velocity profiles are investigated and compared. The equations of motion are derived for the Minimum Acceleration, Minimum Jerk and Minimum Snap trajectories, which minimise the integral of the square of the acceleration, jerk (rate of change of acceleration) and snap (rate of change of jerk) respectively. These ramps are compared to the Linear Trajectory, where the velocity is varied linearly.

### 4.1.1 Background

In previous implementations of optical conveyor-belt transport, the most commonly used velocity profile is a linear ramp, where the velocity is linearly increased from zero to a maximum value before being reduced back to zero at the same rate [63, 126, 128, 129]. To remain consistent with naming of other trajectories considered, this type of velocity ramp will be referred to as the "Linear Trajectory". This gives a trajectory with a position described by a pair of parabolas and piece-wise constant acceleration. A linear ramp can be preferable as it is relatively easy to implement with frequency control systems will often having it as an inbuilt feature. As the acceleration is piece-wise linear, it is discontinuously changed at the start, end and midpoint of the trajectory. These sudden perturbations can lead to large losses of atoms, especially for large accelerations [128].

Avoiding perturbations from discontinuous changes in acceleration motivates the use of more complex trajectories. These include sinusoidal trajectories [61, 165], trajectories piece-wise cubic in acceleration [127], and trajectories where the position is described by the hyperbolic tangent [135]. Transport schemes with low axial confinement have used a Blackman pulse, made from a sum of cosines, for tweezer transport [118] and time-varying magnetic field [166]. Trajectories based on the "Minimum Jerk Trajectory" have been used for moving atoms in a tweezer trap [167, 168].

However little systematic investigation into the effectiveness of different trajectories has been reported. The notable exception to this was the excellent 2020 paper by Hickman and Saffman [61]. It compared the measured transport efficiencies of $^{87}$Rb over a distance of 0.2mm in an optical conveyor-belt with Monte-Carlo simulations to compare two different trajectories. The first was a "triangle" profile, identical to the Linear Trajectory used in other conveyor-belt implementations, and the second was a sinusoidal profile. They found that the sinusoidal trajectory outperformed the Linear Trajectory, which they attributed to its smooth velocity profile.

We chose to investigate the Minimum Jerk Trajectory alongside the Linear Trajectory. The Minimum Jerk Trajectory minimises the square of the jerk, integrated over the trajectory [169]. Inspired by [170], we also investigate the related Minimum Acceleration and Minimum Snap trajectories which similarly minimise the square intergral of acceleration and snap respectively. These trajectories have a relatively straightforward analytical form, with each trajectory being described by a single polynomial, unlike other piece-wise profiles. The differences between the three trajectories, described in Section 4.1.4, allow insight to be gained about different loss mechanisms during transport.

### 4.1.2 Derivation

The equations of motion are derived by minimising an integral of the form:

$$J = \int_0^T \frac{1}{2} Q(t)^2 dt \tag{4.2}$$

where $T$ is the duration of the transport, $t$ is time and $Q(t) = x^{(n)}(t)$ is the quantity to be minimised. The notation

$$x^{(n)} = \frac{d^n x}{dt^n} \tag{4.3}$$

is used to denote the $n$th derivative of position with respect to time. The quantity $Q$ is squared to avoid unwanted cancellation between times when the quantity is positive and when it is negative (e.g. by the boundary conditions that the trajectory begins and ends at rest, the acceleration will always integrate to zero). Integrating the quantity over the trajectory ensures perturbations throughout the entire ramp are taken into account. The factor of $\frac{1}{2}$ is purely for mathematical convenience.

Minimising the integral can be done using the calculus of variations. An integral of the form

$$J = \int_a^b f\left(t, x(t), \dot{x}(t), ..., x^{(n)}(t)\right) dt \tag{4.4}$$

is minimised by a function, $x(t)$, such that $f$ obeys a generalised form of the Euler-

Lagrange equation [171, 172], sometimes known as the Euler-Poisson equation:

$$\frac{\partial f}{\partial t} - \frac{d}{dt}\left(\frac{\partial f}{\partial x^{(1)}}\right) + ... + (-1)^n \frac{d^n}{dt^n}\left(\frac{\partial f}{\partial x^{(n)}}\right) = 0. \tag{4.5}$$

For the case of the Minimum Jerk Trajectory, $Q = x^{(3)}$ giving

$$f = \frac{1}{2}\left(x^{(3)}\right)^2. \tag{4.6}$$

Hence, as $f$ only has an explicit dependence on $x^{(3)}$, there is exactly one non-zero term:

$$0 = \frac{d^3}{dt^3}\left(\frac{\partial f}{\partial x^{(3)}}\right) = \frac{d^3}{dt^3}\left(x^{(3)}\right) = x^{(6)} \tag{4.7}$$

and so the equation of motion is a fifth-order polynomial. The constants can then be found with appropriate boundary conditions. Here, the initial and final positions are given by $x_i$ and $x_f$, and we take the velocity $x^{(1)}(t)$ and acceleration $x^{(2)}(t)$ to be zero at the start and end, yielding a total of six constraints:

$$\begin{aligned} x(0) = x_{\mathrm{i}}, \quad x^{(1)}(0) = 0, \quad x^{(2)}(0) = 0, \\ x(T) = x_{\mathrm{f}}, \quad x^{(1)}(T) = 0, \quad x^{(2)}(T) = 0. \end{aligned} \tag{4.8}$$

Applying these conditions and solving the resultant simultaneous equations gives the equation:

$$x = x_i + (x_f - x_i)\left(10\left(\frac{t}{T}\right)^3 - 15\left(\frac{t}{T}\right)^4 + 6\left(\frac{t}{T}\right)^5\right). \tag{4.9}$$

Similarly, the equations of motion for the Minimum Acceleration and Minimum Snap trajectories can be derived by setting $Q = a = x^{(2)}$ and $Q = x^{(4)}$, giving 3rd and 7th order polynomials respectively. The coefficients for the Minimum Acceleration Trajectory are found by applying the same constraints on the initial and final positions and requiring zero velocity at the start and end:

$$
\begin{aligned}
x(0) &= x_\mathrm{i}, \quad x^{(1)}(0) = 0, \\
x(T) &= x_\mathrm{f}, \quad x^{(1)}(T) = 0.
\end{aligned}
\tag{4.10}
$$

The Minimum Snap Trajectory coefficients are derived by setting velocity, acceleration and jerk to zero at the start and end, as well as from the constraints on the initial and final positions:

$$
\begin{aligned}
x(0) &= x_\mathrm{i}, \quad x^{(1)}(0) = 0, \quad x^{(2)}(0) = 0, \quad x^{(3)}(0) = 0, \\
x(T) &= x_\mathrm{f}, \quad x^{(1)}(T) = 0, \quad x^{(2)}(T) = 0, \quad x^{(3)}(T) = 0.
\end{aligned}
\tag{4.11}
$$

The final trajectory considered is the "Linear Trajectory", consisting of a piecewise function which is linear in velocity. Like the Minimum Acceleration Trajectory, the Linear Trajectory is subject to the boundary conditions on the initial and final position as well as zero velocity at the start and end. To avoid jumps in detuning, the velocity of the two pieces is matched at $t = T/2$.

### 4.1.3 Equations of Motion

The equations of motion for the four different trajectories are presented below. For reference, the velocities and accelerations are also given. For all profiles the initial position is taken to be zero, $x_\mathrm{i} = 0$, and the distance moved is given by $d = x_\mathrm{f} - x_\mathrm{i} = x_\mathrm{f}$. As above, the duration of the trajectory is given by $T$. These two quantities, duration and distance, completely describe any frequency ramp and scale the $x$ and $y$ axes respectively.

**Position**

Minimum Acceleration Trajectory:

$$
x(t) = d\left[3\left(\frac{t}{T}\right)^2 - 2\left(\frac{t}{T}\right)^3\right]
\tag{4.12}
$$

Minimum Jerk Trajectory:

$$x(t) = d\left[10\left(\frac{t}{T}\right)^3 - 15\left(\frac{t}{T}\right)^4 + 6\left(\frac{t}{T}\right)^5\right] \tag{4.13}$$

Minimum Snap Trajectory:

$$x(t) = d\left[35\left(\frac{t}{T}\right)^4 - 84\left(\frac{t}{T}\right)^5 + 70\left(\frac{t}{T}\right)^6 - 20\left(\frac{t}{T}\right)^7\right] \tag{4.14}$$

Linear Trajectory:

$$x(t) = \begin{cases} d\left[2\left(\frac{t}{T}\right)^2\right] & \text{if } 0 \leq t/T \leq \frac{1}{2} \\ \\ d\left[-1 + 4\left(\frac{t}{T}\right) - 2\left(\frac{t}{T}\right)^2\right] & \text{if } \frac{1}{2} < t/T \leq 1 \end{cases} \tag{4.15}$$

**Velocity**

Minimum Acceleration Trajectory:

$$x^{(1)}(t) = 6\frac{d}{T}\left[\left(\frac{t}{T}\right) - \left(\frac{t}{T}\right)^2\right] \tag{4.16}$$

Minimum Jerk Trajectory:

$$x^{(1)}(t) = 30\frac{d}{T}\left[\left(\frac{t}{T}\right)^2 - 2\left(\frac{t}{T}\right)^3 + \left(\frac{t}{T}\right)^4\right] \tag{4.17}$$

Minimum Snap Trajectory:

$$x^{(1)}(t) = 140\frac{d}{T}\left[\left(\frac{t}{T}\right)^3 - 3\left(\frac{t}{T}\right)^4 + 3\left(\frac{t}{T}\right)^5 - \left(\frac{t}{T}\right)^6\right] \tag{4.18}$$

Linear Trajectory:

$$x^{(1)}(t) = \begin{cases} 4\frac{d}{T}\left[\left(\frac{t}{T}\right)\right] & \text{if } 0 \leq t/T \leq \frac{1}{2} \\ \\ 4\frac{d}{T}\left[1-\left(\frac{t}{T}\right)\right] & \text{if } \frac{1}{2} < t/T \leq 1 \end{cases} \tag{4.19}$$

### Acceleration

Minimum Acceleration Trajectory:

$$x^{(2)}(t) = 6\frac{d}{T^2}\left[1-2\left(\frac{t}{T}\right)\right] \tag{4.20}$$

Minimum Jerk Trajectory:

$$x^{(2)}(t) = 60\frac{d}{T^2}\left[\left(\frac{t}{T}\right)-3\left(\frac{t}{T}\right)^2+2\left(\frac{t}{T}\right)^3\right] \tag{4.21}$$

Minimum Snap Trajectory:

$$x^{(2)}(t) = 420\frac{d}{T^2}\left[\left(\frac{t}{T}\right)^2-4\left(\frac{t}{T}\right)^3+5\left(\frac{t}{T}\right)^4-2\left(\frac{t}{T}\right)^5\right] \tag{4.22}$$

Linear Trajectory:

$$x^{(2)}(t) = \begin{cases} 4\frac{d}{T^2} & \text{if } 0 \leq t/T \leq \frac{1}{2} \\ \\ -4\frac{d}{T^2} & \text{if } \frac{1}{2} < t/T \leq 1 \end{cases} \tag{4.23}$$

### Bonus Trajectories

To complete the set of trajectories that minimise a named derivative of displacement, the equations of motion for the Minimum Crackle Trajectory and Minimum Pop Trajectory are given below. Crackle is the rate of change of snap and pop is the rate of change crackle, or the fifth and sixth derivatives of displacement respectively. These trajectories' appeal is entirely their excellent names and *pleasing* coefficients. Any attempts by the reader to find a use for them are highly encouraged. Any attempts by the reader to derive them by hand are highly discouraged.

Minimum Crackle Trajectory:

$$x(t) = d\left[126\left(\frac{t}{T}\right)^5 - 420\left(\frac{t}{T}\right)^6 + 540\left(\frac{t}{T}\right)^7 - 315\left(\frac{t}{T}\right)^8 + 70\left(\frac{t}{T}\right)^9\right], \quad (4.24)$$

Minimum Pop Trajectory:

$$\begin{aligned} x(t) =& d\left[462\left(\frac{t}{T}\right)^6 - 1980\left(\frac{t}{T}\right)^7 + 3465\left(\frac{t}{T}\right)^8\right. \\ & \left. - 3080\left(\frac{t}{T}\right)^9 + 1386\left(\frac{t}{T}\right)^{10} - 252\left(\frac{t}{T}\right)^{11}\right], \end{aligned} \quad (4.25)$$

where $d$ is the transport distance and $T$ is the transport duration as before.

### 4.1.4 Theoretical Comparison

Plots of the position, velocity, acceleration and jerk for the different trajectories considered are shown in Figure 4.1. The position dependence, shown in Figure 4.1(a), is “s-shaped” for all four trajectories. The steepness of the central part of the curve increases going from the Minimum Acceleration Trajectory to the Minimum Jerk Trajectory. This is due to the latter trajectory being slower at the start and end, as the Minimum Jerk Trajectory has zero acceleration at the end points whereas the Minimum Acceleration trajectory does not, see Equation 4.10 and Equation 4.8. The same applies when comparing the Minimum Jerk Trajectory to the Minimum Snap Trajectory. The central part of the position curve of the latter is steeper due to the additional boundary condition of zero jerk at the start and end of the trajectory, see Equation 4.11. The Linear Trajectory sits between the Minimum Acceleration and Minimum Jerk trajectories. The gentler start and end of higher order trajectories also leads to greater peak velocities, as shown in Figure 4.1(b).

One key distinction between the different trajectories is the continuity of the acceleration. As shown in Figure 4.1(c), the acceleration of both the Linear and Minimum Acceleration trajectories is non-zero at the start and end, leading to a discontinuity. The Linear Trajectory’s acceleration has an additional discontinuity

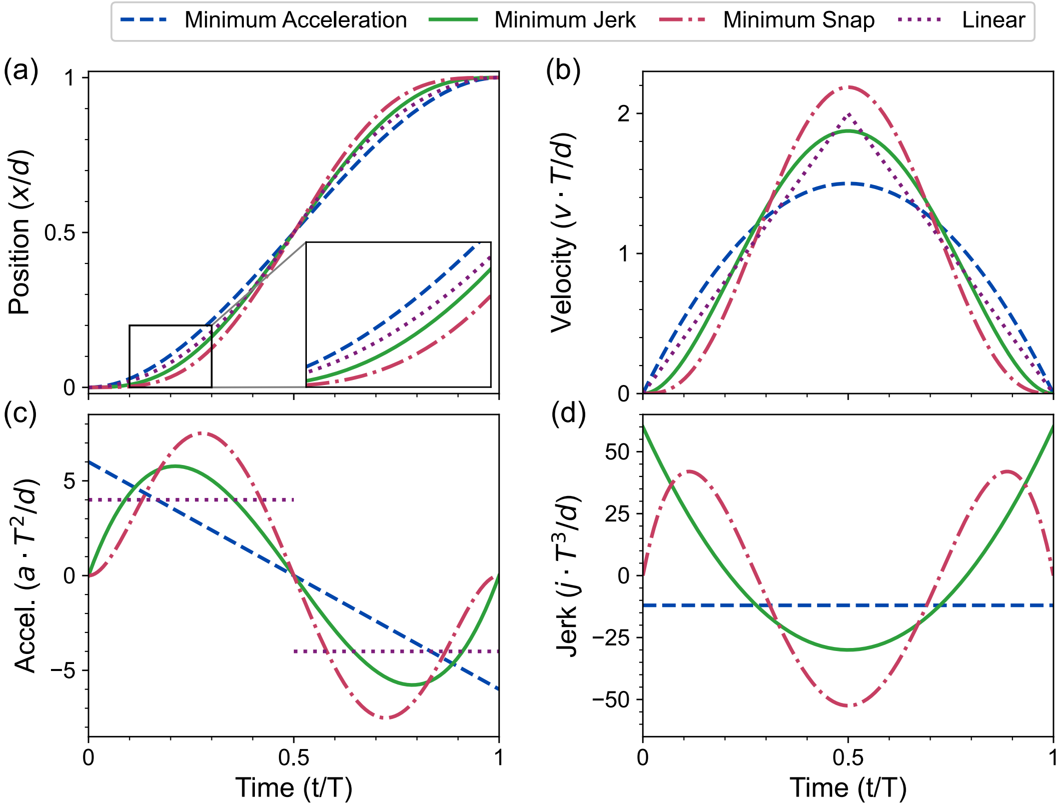

Figure 4.1: Plots of (a) position, (b) velocity, (c) acceleration and (d) jerk varying with time for four different trajectories: Minimum Acceleration in shown by the dashed blue lines, Minimum Jerk by the solid green lines, Minimum Snap in the dash-dotted red lines and the Linear Trajectory in the purple dotted lines. As described in the main text, the Linear Trajectory is taken to be piece-wise linear in velocity. All quantities are appropriately normalised to the distance $d$ and duration $T$. The jerk for the Linear Trajectory is omitted as it consists of 3 Dirac-delta peaks at $t/T = 0$, 0.5 and 1.

| Trajectory | Max Velocity<br>A $= v_{\text{max}} \times {}^{T}\!/_{d}$ | Max Acceleration<br>B $= a_{\text{max}} \times {}^{T^2}\!/_{d}$ |
|---|---|---|
| Minimum Acceleration | $\frac{3}{2} = 1.5$ | 6 |
| Minimum Jerk | $\frac{15}{8} = 1.875$ | $\frac{10}{\sqrt{3}} \approx 5.77$ |
| Minimum Snap | $\frac{35}{16} = 2.1875$ | $\frac{84}{5\sqrt{5}} \approx 7.51$ |
| Linear | 2 | 4 |

Table 4.1: Calculated values of the maximum velocities and accelerations for the four different trajectories given in terms of the distance $d$ and duration $T$.

at its midpoint. Only for the Minimum Snap Trajectory is the jerk continuous throughout. For the Minimum Acceleration and Minimum Jerk trajectories, the jerk is discontinuous at the start and end (see Figure 4.1(d)).

For optical conveyor-belt transport, the transport trajectories are implemented by appropriately varying the lattice velocity $v_{\text{lattice}}$ which is determined by the frequency detuning between the two lattice beams $\Delta f$ according to $v_{\text{lattice}} = \lambda \Delta f/2$. The frequency control setup determines the maximum frequency detuning achievable, which for our setup is $\Delta f = 103$MHz. As we are working with 1064nm light, this gives a maximum achievable velocity of 54.7m/s [1]. The maximum velocity of the lattice during transport is given by

$$v_{\text{max}} = A\frac{d}{T} = Av_{\text{avrg}} \tag{4.26}$$

where $d$ is the transport distance, $T$ is the transport duration, $v_{\text{avrg}}$ is average transport velocity and $A$ is a constant dependent on the trajectory. Table 4.1 gives the values $A$ for the four trajectories.

### Axial Trap Tilt

The acceleration of the lattice tilts the axial trapping potential in the same way as gravity does for the vertical potential, see Section 2.3.4. The axial trap extent

---

[1] To put this in everyday terms, this is equal to peak velocity 197km/h or 122mph. As far as I was able to determine this significantly exceeds the national speed limit in all but one country.

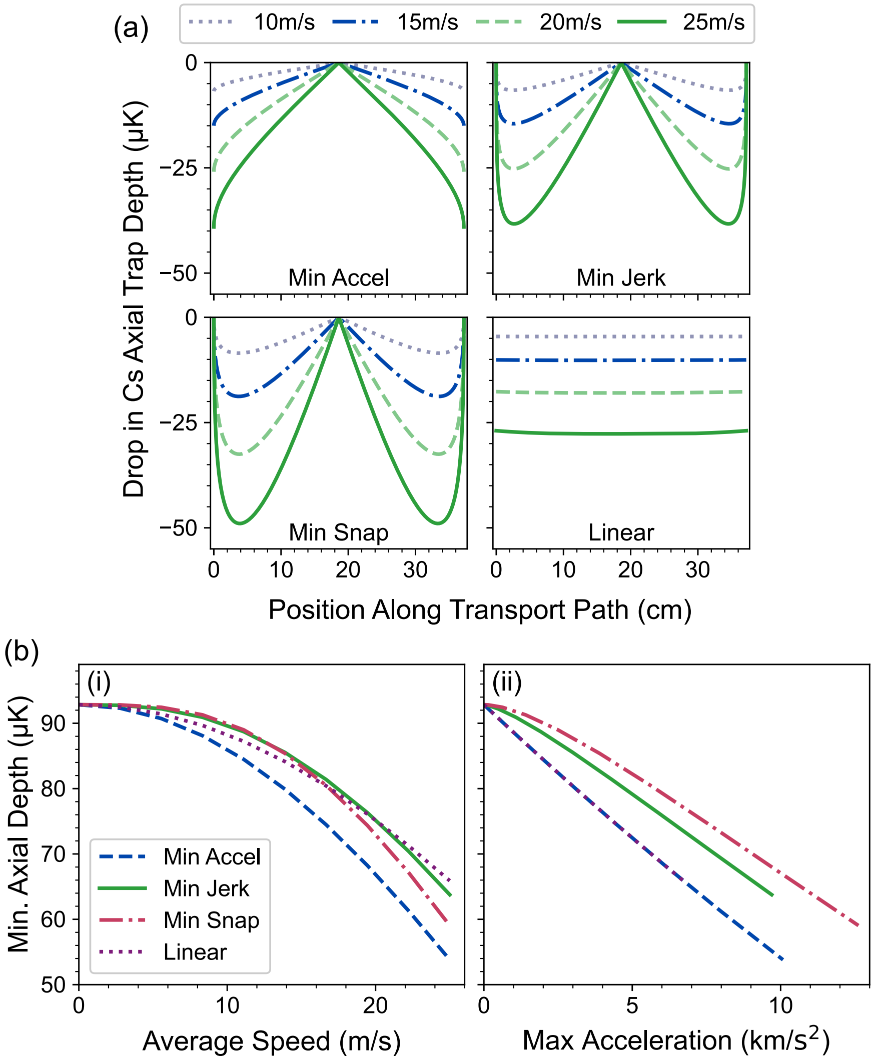

Figure 4.2: Drop in axial trap depth due to accelerational tilt. (a) Shows the decrease in axial trap depth along the transport path due to the acceleration of each trajectory for four different speeds. (b) Shows the minimum axial trap depth for each trajectory, given as a function of average speed in panel (i) and as a function of maximum acceleration in (ii). The trap depth reductions are calculated for Cs using the optimised beam parameters of $x_0 = 7.3\text{cm}$ and $w_0 = 195\mu\text{m}$. The Minimum Acceleration Trajectory is shown by the dashed blue lines, the Minimum Jerk Trajectory is shown by the solid green lines, the Minimum Snap Trajectory by the dash-dotted red line and the Linear Trajectory by the dotted purple line.

is given by half the wavelength, $\lambda/2 = 0.532\mu$m of the trapping light which is much smaller than the radial size of the beams, $w \approx 200\mu$m. Hence, as shown in Section 2.3.4, the axial decrease in trap depth from acceleration tilting is much smaller than the radial decrease for the same acceleration. However the maximum axial accelerations experienced by the atoms is up to 1280 times greater than the acceleration due to gravity. The maximum acceleration experienced by the atoms during transport is given by

$$a_{\mathrm{max}} = B\frac{d}{T^2} = B\frac{{v_{\mathrm{avrg}}}^2}{d}, \tag{4.27}$$

where $B$ is a constant dependent on the trajectory used, given in Table 4.1. For the fastest frequency ramps of 25m/s average speed investigated, the maximum acceleration experienced by the atoms is 12.6km/s$^2$ for the Minimum Snap Trajectory.

Figure 4.2(a) shows the decrease in Cs axial trap depth for each trajectory. Four different average transport speeds are shown. For the optimised beam shapes used, the minimum axial trap depth for Cs is $92\mu$K. At higher average speeds, the accelerational trap depth decreases therefore represent a significant decrease in trap depth. As can be expected, the decrease in trap depths are largest at the points where the greatest accelerations occur: at the start and end of the transport path for the Minimum Acceleration Trajectory and $\approx$ 4cm from the edges for the Minimum Jerk and Minimum Snap trajectories. The shapes of the trap depth drop curves in this figure are different to the acceleration curves shown in Figure 4.1(c) as they are shown as a function of distance rather than time. This is clearest from the Minimum Acceleration Trajectory panel.

The reduction in the minimum axial trap depth is shown in Figure 4.2(b). The trap depth throughout the transport path is calculated, as for Figure 4.2(a) and the minimum is taken. The minimum axial depth is plotted against the average transport speed in panel (i) over a range of 0m/s to 25m/s. Panel (ii) shows the same values plotted against the maximum acceleration for the same range of average speeds, converted using Equation 4.27. Somewhat ironically, the Minimum Acceleration Trajectory suffers from the heaviest reduction in trap depth, even though the

Minimum Snap Trajectory has the greater maximum acceleration. The reason for the difference is the variation in axial trap depth with position along the transport path and where the maximum acceleration occurs for each trajectory. The Minimum Acceleration's greatest acceleration occurs at the edges of the transport path, coinciding with the point where the axial confinement is weakest. For the Minimum Snap and Minimum Jerk trajectories on the other hand, the points of greatest acceleration occur away from the edges of the transport path, where the axial trap depth is greater. Hence the axial trap depth reduction is higher for the Minimum Acceleration Trajectory even for the same maximum acceleration, as seen in panel (ii). The differences between the Minimum Jerk and the Minimum Snap trajectories can similarly be explained. The points of greatest acceleration occur closer to the centre of the transport for the latter trajectory, where the axial depth is higher. This difference is most easily seen in Figure 4.1(c). The Linear Trajectory also has a large acceleration at the edges of the transport path, similar to the Minimum Acceleration Trajectory. The lower $B$ factor (see Equation 4.27 and Table 4.1) for the Linear Trajectory compared to the Linear Trajectory means a less severe decrease in minimum axial depth decrease with average speed, see Figure 4.2(b)(i). However, when accounting for the differences in maximum acceleration in panel (ii) the drop-off is identical for the two ramps.

Unfortunately there is no practical way to counteract the axial trap tilt using magnetic gradients, in a way comparable to the way gravity can be counteracted. As the accelerations involved are up to three orders of magnitude larger, the magnetic gradients would need to be increased by the same amount. Instead, the effect of the axial tilt on the transport was characterised by measuring the transport efficiency for a range of average speeds for each trajectory.

### 4.1.5 Experimental Comparison

#### Transport Efficiency

The trajectories are experimentally compared by measuring the transport efficiencies for each trajectory as a function of the average transport speed, or equivalently the

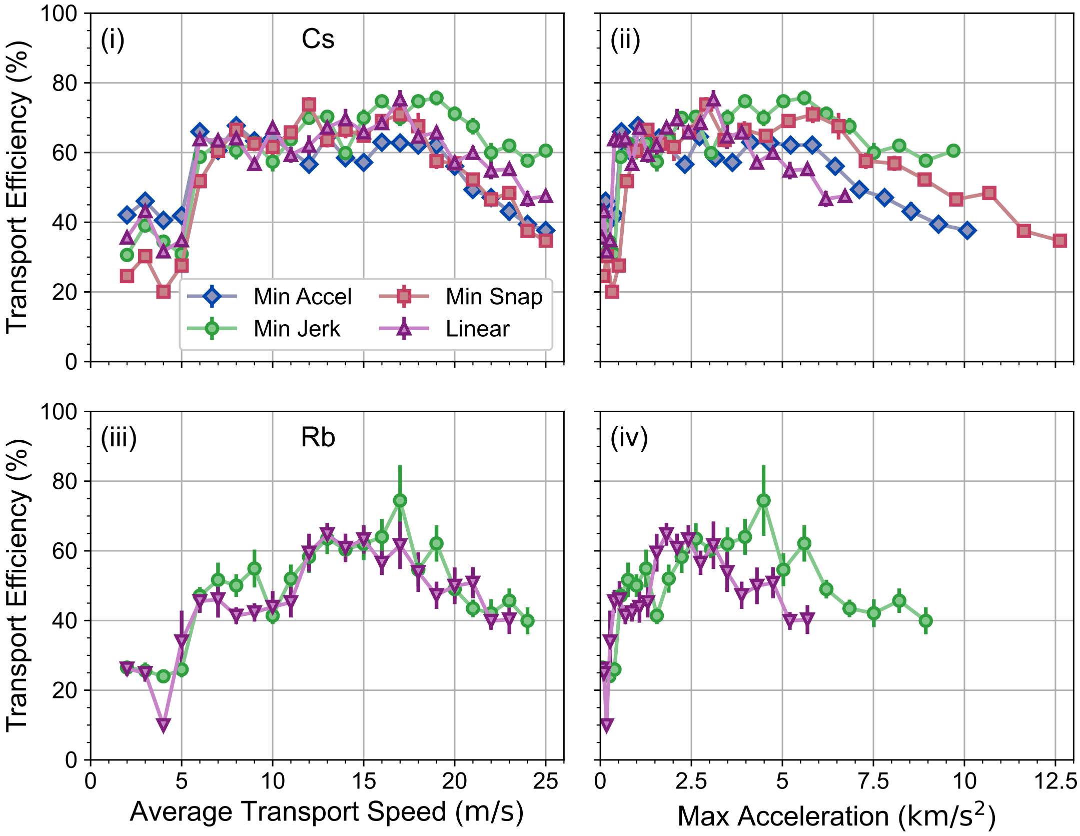

Figure 4.3: Transport efficiencies for different trajectories. The Cs transport efficiencies for all four ramps are shown in (i) and (ii), plotted against the average transport speed and maximum acceleration respectively. The Rb transport efficiencies for the Minimum Jerk and Linear trajectories are shown in (iii) and (iv), plotted against the average transport speed and maximum acceleration respectively. The efficiencies are calculated from the ratio between the number of atoms that arrive in the Science Cell and the number of atoms loaded into the optical conveyor-belt in the MOT Chamber. Lines between the data points are included as a guide to the eye.

transport duration, as shown in Figure 4.3. For each speed the number of atoms arriving in the Science Cell is measured and normalised against the number of atoms loaded into the optical conveyor-belt in the MOT Chamber to obtain the transport efficiency. The atoms are held in the MOT Chamber for the same duration as the transport to account for any losses due to the finite lifetime in the lattice. For each species the entire dataset was taken on the same day and the order of ramps and speeds fully randomised to minimise the effect of long-term drifts in the experiment. To account for shot-to-shot variation, the experimental cycle was run ten times for each point to obtain five measurements in the MOT Chamber and five measurements in the Science Cell. The standard deviation in the two measurements was used to estimate the error in the transport efficiency.

The largest average velocity investigated was 25m/s at the full transport distance of 37.2cm, corresponding to a transport duration of 14.9ms. This is limited by the maximum total detuning of 103MHz achievable in our seed setup. Increasing the power to the seed path could increase the maximum achievable detuning, enabling faster ramps. However, as seen in Figure 4.3, in panel (i) for Cs and panel (iii) for Rb, the transport efficiency declines significantly above average speeds of 18m/s for all ramps and both species. Optimum transport efficiencies of up to 75% are achieved between 6m/s and 18m/s for Cs. The Minimum Jerk Trajectory shows the clearest and broadest peak in efficiency between 15m/s and 21m/s for Cs. For Rb only the Minimum Jerk and Linear trajectories were investigated. The results were largely similar to those for Cs, albeit with a narrower central peak between 11m/s and 19m/s. A maximum efficiency of 75% was achieved with the Minimum Jerk Trajectory at 17m/s.

Insight into the efficiency decline at high speeds can be gained by calculating the maximum acceleration using Equation 4.27 and rescaling the x-axis accordingly. The dependence of the transport efficiency on maximum acceleration is shown in panel (ii) for Cs and panel (iv) for Rb in Figure 4.3. In panel (ii), the drop-off in efficiency occurs above maximum accelerations of 6km/s$^2$ for all ramps. This drop-off is attributed to the accelerational tilting of the axial trapping potential described in Section 4.1.4. At higher accelerations the difference between the trajectories becomes clearer, the Minimum Jerk Trajectory performing the best, closely followed by the Minimum Snap Trajectory. The Minimum Acceleration and Linear trajectories both show substantial reductions in efficiency. This difference may be explained by steeper decrease in axial trap with maximum acceleration for the Maximum Acceleration and Linear trajectories shown in Figure 4.2(b)(ii) and discussed in Section 4.1.4.

Another significant difference between the ramps is that the former two trajectories are continuous in acceleration, while the latter two have discontinuities in the acceleration, as shown in Figure 4.1(c). Both have discontinuities at the start and end, but the Linear Trajectory also has a discontinuity at the midpoint, $t = T/2$. This difference may explain the slight difference between the Linear and Minimum Acceleration Trajectory observed. The combination of the different axial trap depth reductions and the discontinuities in acceleration likely account for the differences in performance observed.

All trajectories experience a sharp decrease in transport efficiency for average transport speeds $v_{\mathrm{avrg}} \leq 5\mathrm{m/s}$ for both Rb and Cs. This drop-off can be attributed to the limited update rate of the RF generator used to control the difference in the lattice frequencies. As the ramp speed decreases, the update frequency must also be decreased in order to be able to store the entire ramp in the limited memory of the RF generator. When the average is $\leq 5\mathrm{m/s}$ (equivalent to a duration $\geq 74\mathrm{ms}$), the update frequency becomes comparable to the axial trap frequency at $\approx 110\mathrm{kHz}$. This leads to parametric heating and loss [61]. Note that the fastest usable update rate depends on the distance and duration of the transport, but not on the trajectory used.

### Update Frequency

In Figure 4.4 the dependence of transport efficiency on the update frequency of the frequency source is explicitly investigated. The efficiency of Cs transported to the Science Cell using the Minimum Jerk Trajectory is measured. Three different average speeds (maximum accelerations) are investigated. The figure shows the importance of using update rates significantly above the axial trap frequency, $\approx 110\,\mathrm{kHz}$ in this case. As an example, we see that for a maximum acceleration of

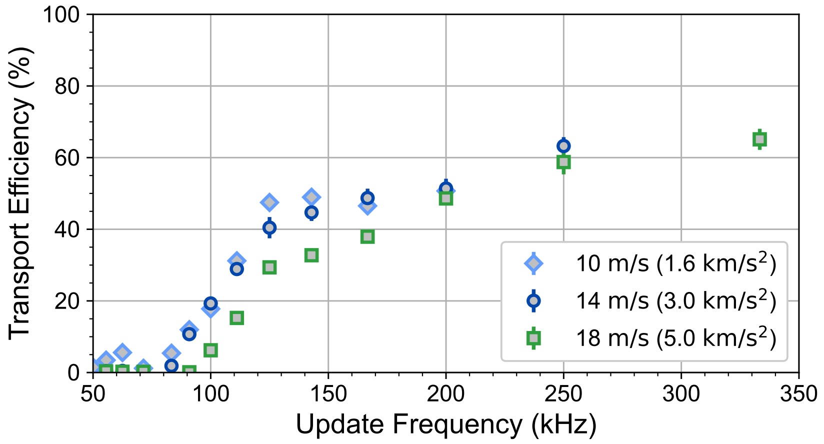

Figure 4.4: The dependence of the transport efficiency on the update frequency. Data for Cs transport to the Science Cell using the Minimum Jerk Trajectory for three different ramp speeds (maximum accelerations).

5km/s$^2$, reducing the update rate from 333kHz to 167kHz leads to a drop in efficiency from 66% to 38%.

### Temperature after Transport

The number of atoms transported to the Science Cell is not the only figure of merit when evaluating transport, the other important quantity is the temperature of atoms. However the temperature is much more challenging to measure. The standard method is a “time-of-flight” (TOF) measurement where the trap is rapidly turned off and the atoms allowed to expand ballistically for a short time before being imaged. This is done for several different expansion times. From a measurement of cloud size as a function of expansion time, the average velocity and hence temperature of the atoms can be inferred.

However in our experiment we are unable to rapidly turn off the transport lattice. This is because the time scale set by the axial trap frequency is of the order of 0.1ms whereas we are only able to shutter our transport beams within a few ms. The atoms therefore experience adiabatic expansion into a much shallower trap and are hence cooled, thereby making a time-of-flight an unreliable measure of temperature. A TOF measurement was nonetheless still performed to try and extract a radial temperature from the vertical expansion of the cloud. This yielded a slight increase

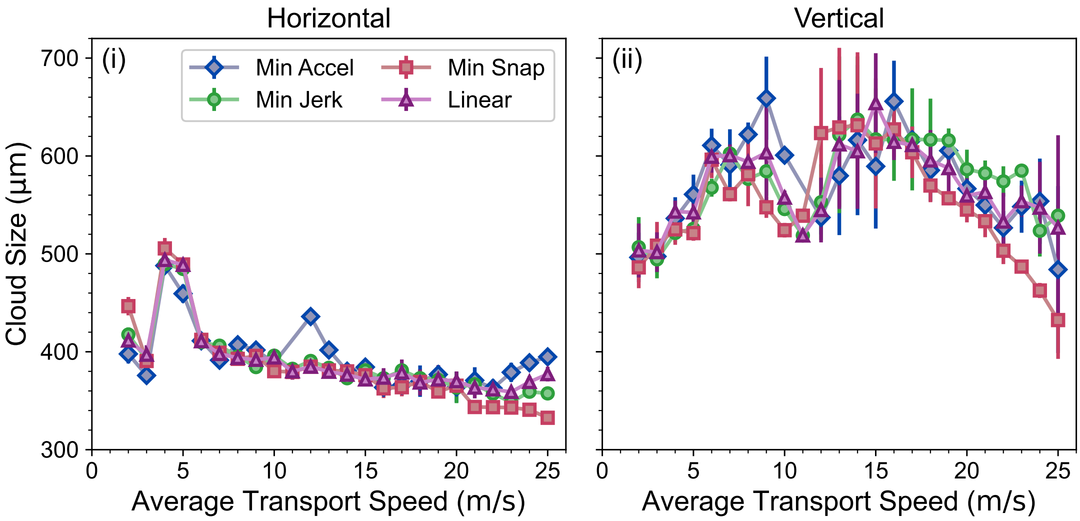

Figure 4.5: Size of the atomic cloud after transport in the Science Cell for different trajectories . (i) Shows the horizontal cloud size, which is mostly determined by the axial extent of the cloud. (ii) Shows the vertical cloud size, which is determined entirely by the vertical radial extent of the cloud.

in temperature increase from 17.7(5)$\mu$K in the MOT chamber to 21(1)$\mu$K for Cs.

Additionally the data from Figure 4.3 was re-analysed to look for changes in cloud size with transport ramp and average speed, as shown in Figure 4.5. As all measurements were taken at the same time of flight, any large sources of heating may be seen as an increase in cloud size. Horizontally, a clear increase in the cloud size can been seen for all trajectories for 4m/s and 5m/s average speed. This corresponds to the point at which the update frequency becomes comparable to the axial trap frequency, see above. Vertically, there is some variation in the cloud size but no distinct features. The gradual drop-off in size at large and small speeds could be mostly due to a reduction in the number of atoms transported.

Instead of trying to measure the temperature directly, the number of atoms loaded into a dipole trap after transport can be measured. If given enough time, the atoms will thermalise to a temperature set by the trap depth. At that point the temperature of the atoms is given by the trap depth. Any heating will then be seen as atom loss [2].

---

[2] As a side-note, similar principle is at play during transport. Heating mechanism that cause

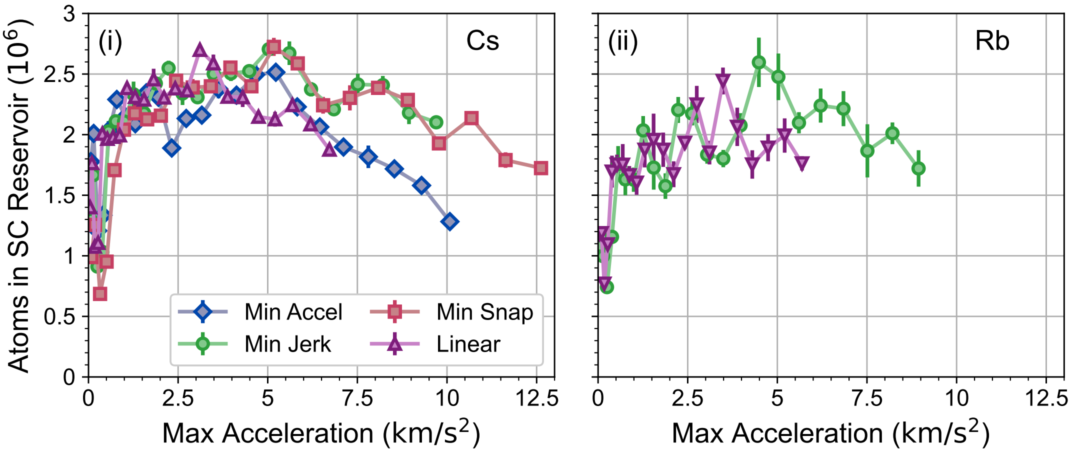

Figure 4.6: Number of atoms loaded into the Science Cell reservoir trap for different trajectories. (i) Shows the number of Cs atoms loaded while (ii) shows the number of Rb atoms loaded. Both are plotted against the trajectory's maximum acceleration.

### Loading into a Dipole Trap

The number of atoms loaded into the Science Cell reservoir trap was measured for all four trajectories at different average speeds (maximum accelerations). This crudely probes the temperature of the transported atoms, as described above.

The crossed optical dipole trap has a depth that was $\approx$ 50% lower than the transport lattice. The dependence of the number of atoms loaded on the maximum acceleration is shown in Figure 4.6, for Cs in panel (i) and for Rb in panel (ii). It is broadly similar to the dependence of the transport efficiency on the maximum acceleration, shown in Figure 4.3. The number of atoms drops off sharply at low accelerations due to the update rate, and declines more gradually at high accelerations due to the axial tilting. One notable difference is that for Cs, above 6km/s$^2$ the difference in performance of the Minimum Jerk and Minimum Snap trajectories becomes indiscernible. This suggests that the additional atoms transported by the Minimum Jerk Trajectory evident in Figure 4.3 are in the high energy tail of the distribution. Up to $2.70(5) \times 10^6$ Cs atoms and $2.6(2) \times 10^6$ Rb atoms were loaded into the Science Cell reservoir, corresponding to loading efficiencies of 37.0(1.1)%

---

atoms loss are not easily distinguishable from other atom loss mechanism.

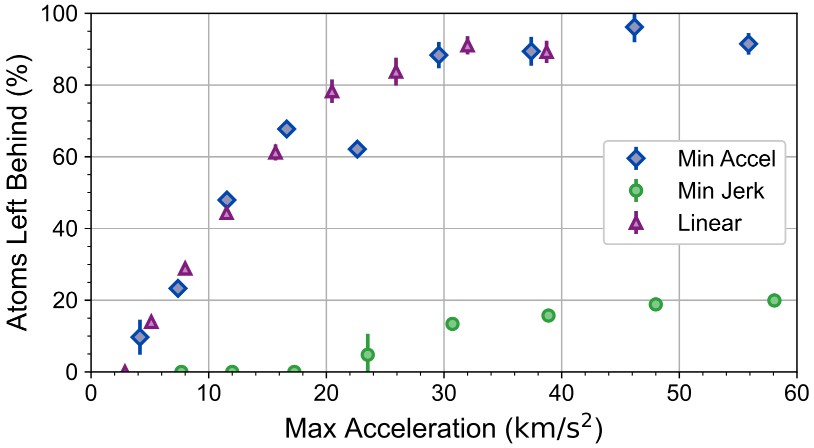

Figure 4.7: Atoms left behind in the MOT Chamber due to axial tilting, measured as a function of maximum acceleration. The measurement is performed for three different trajectories: the Minimum Acceleration and Linear Trajectories, which have large accelerations at the very start of the ramp and the Minimum Jerk Trajectory which has zero initial acceleration. Error bars show the standard deviation from five repeated measurements.

and 44(6)% respectively.

### Atoms Left Behind

To further investigate the differences between the trajectories, the number of atoms left behind in the MOT Chamber was measured as a function of maximum acceleration for three different trajectories, see Figure 4.7. The Linear and Maximum Acceleration trajectories were investigated as they both subject the atoms to large initial accelerations. The atoms left behind by the Minimum Jerk Trajectory were also measured for comparison. As can be seen from the figure, both the Linear and Minimum Acceleration Trajectories result in a large number of atoms left behind in the MOT Chamber when the maximum acceleration exceeds 10km/s$^2$. Above 30km/s$^2$ nearly all of the atoms are lost from the optical conveyor-belt. Below maximum accelerations of 20km/s$^2$, there was no detectable signal of atoms left behind by the Minimum Jerk Trajectory. However it is important to note that at these high accelerations virtually all atoms will be lost for the Minimum Jerk Trajectory, see Figure 4.3(ii), but this loss will occur further into the transport path.

The measurement was performed by applying a one-way ramp to the lattice and subsequently imaging in the MOT Chamber. Similarly to the transport efficiency measurements, the number of atoms left behind was normalised against a measurement of the number of atoms loaded into the optical conveyor-belt. The order in which the data points were taken was also randomised. A transport distance of 5cm was used which enabled large accelerations to be investigated (which would not be possible for the full transport distance due to the limitation on the lattice detuning). However this distance was large enough to ensure that all atoms transported were firmly outside of the field of view of the MOT Chamber imaging system.

### 4.1.6 Trajectories Summary

Based upon these measurements, the Minimum Jerk Trajectory is found to be optimal in our application. Comparing the transport efficiency of the Minimum Jerk Trajectory in Figure 4.3 it shows a clear advantage over the Linear and Minimum Acceleration Trajectories and a slight advantage over the Minimum Snap Trajectory. When measuring the number of atoms loaded into the Science Cell reservoir trap, the differences between the Minimum Jerk and Minimum Snap trajectories became negligible. Nonetheless, we slightly favour the Minimum Jerk Trajectory as it transports the atoms faster than the Minimum Snap Trajectory for the same maximum acceleration.

## 4.2 Further Characterisation

In between the measurements presented above comparing transport trajectories and the additional characterisation measurements presented below, one of the lattice beams required realigning. This was due to an issue with the fibre amplifier, which resulted in the lenses in that beam path needing to be adjusted and the beams needing to be walked to overlap them again. After realignment, the number of atoms that reached the Science Cell remained unchanged with up to $7 \times 10^6$ atoms of either species. However the number of atoms loaded into the optical conveyor-belt in the Main Chamber increased from $\approx 9 \times 10^6$ to $\approx 1.1 \times 10^7$ for both species, and hence the transport efficiencies are lower. As the number of atoms transported and

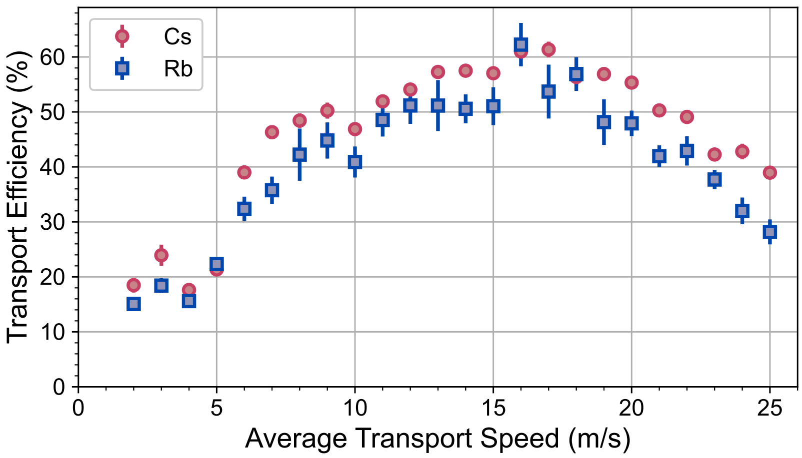

Figure 4.8: Comparing the transport efficiency dependence on average transport speed. Cs is shown in red circles and Rb in blue squares. Data was taken for each species separately using the Minimum Jerk Trajectory.

the number subsequently loaded into the Science Cell reservoir trap were unchanged, the quality of our transport remained the same. The differences are likely due to slight changes in beam waists, focus positions and/or beam overlap which lead to a slightly deeper trap in the Main Chamber at the cost of enhanced losses during transport.

### 4.2.1 Transport Speed

Figure 4.8 shows the dependence of the transport efficiency on the average transport speed for both Cs and Rb, after the fibre amplifier 2 beam was realigned. Both species show the same behaviour as before, with the drop-off in efficiency at low speeds due to the update rate and the decline at high speeds due to accelerational tilting. The figure also highlights the similarity between the two species. Despite the significantly lower polarisability, and hence trap depth, for Rb the achievable transport efficiency is equal to the efficiency for Cs, with both species having a maximum in transport efficiency of 60% for speeds of 16m/s. This corresponds to $7.3(3) \times 10^6$ Rb atoms and $6.88(5) \times 10^6$ Cs atoms transported. Around the maximum, between 14m/s and 18m/s the transport efficiency remains above 50% with an average of 6.37(13) Rb atoms and $6.43(5) \times 10^6$ Cs atoms transported to

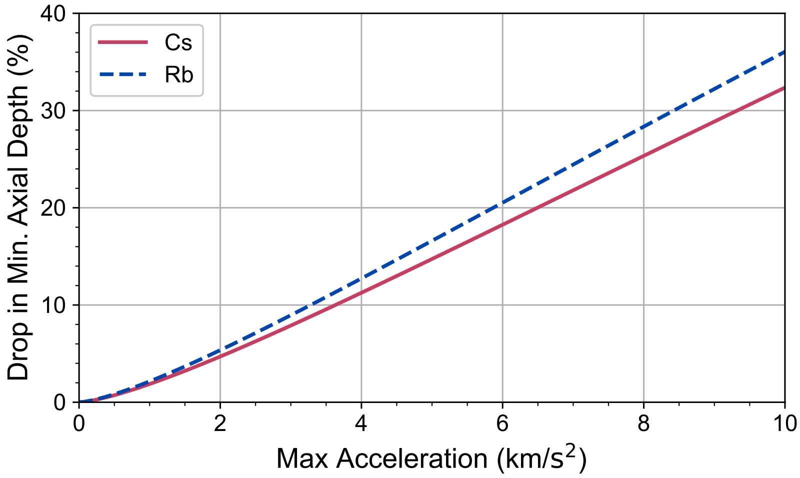

Figure 4.9: Comparing the effect of the acceleration tilt on Cs (solid red line) and Rb (dashed blue line). The drop in the minimum axial trap depth is plotted as function of the maximum acceleration for the Minimum Jerk Trajectory.

the Science Cell.

The drop-off in transport efficiency at high speeds (accelerations) is slightly more pronounced for Rb than for Cs. This is likely due to the lower polarisability of Rb, leading to a greater reduction in axial trap depth due to accelerational tilting, as shown in Figure 4.9. For an average speed of 25m/s the maximum acceleration from the Minimum Jerk Trajectory is 9.7km/s$^2$ which leads to a reduction in the minimum axial depth of 31.3% for Cs and 34.9% for Rb.

At low speeds the transport efficiency drop-off due to the update rate is very similar for the two species. While there is a slight difference in the axial trap frequencies between the two species (see Section 2.7) they are smaller than the difference in axial tilt. However in Figure 4.8 the drop-off appears smoother than in Figure 4.3, especially noticeable for Rb. This indicates that the axial trap frequencies changed as result of the transport lattice realignment changing the beam shape of transport amplifier 2.

### 4.2.2 Beam Power

After atoms were loaded into the reservoir trap in the Main Chamber, both transport lattice beams were ramped on to some power and the number of atoms transported

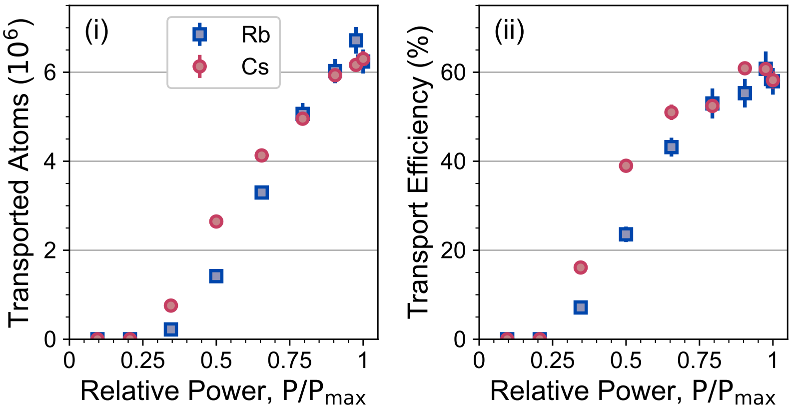

Figure 4.10: The effect of varying the power in the transport lattice beams. The number of atoms that reach the Science Cell is shown in panel (i) and the transport efficiency is shown in panel (ii). For these data $P_{\text{max}} = 20(1)$W in each beam. Cs is shown in red circles and Rb in blue squares. Data was taken for each species separately using the Minimum Jerk Trajectory.

to the Science Cell measured. At each power, the number of atoms loaded into the transport lattice in the Main Chamber was also measured and the transport efficiency calculated. Figure 4.10 shows both the number of atoms transported and the transport efficiency for Rb and Cs as a function of the power used to form the lattice, up to a maximum of $P_{\text{max}} = 20(1)$W in each beam. Both the atom number and the efficiency increase approximately linearly above a threshold of $P/P_{\text{max}} \approx 0.3$. The number of atoms transported shows a fairly linear increase with power for both species. Meanwhile the transport efficiency starts to plateau above $P/P_{\text{max}} \approx 0.8$, suggesting that the number of atoms transported is limited by the number loaded into the transport lattice rather than insufficient trap depth leading to loss during the transport. This indicates that more atoms could be delivered to the Science Cell by further increasing the laser power. One relatively straightforward way of doing this would be to replace the existing fibre amplifiers with higher power amplifiers.

## 4.3 Dual Species Transport

In Figure 4.11 simultaneous dual-species transport of Cs and Rb is presented. For comparison transport efficiencies are also presented without the second species. All

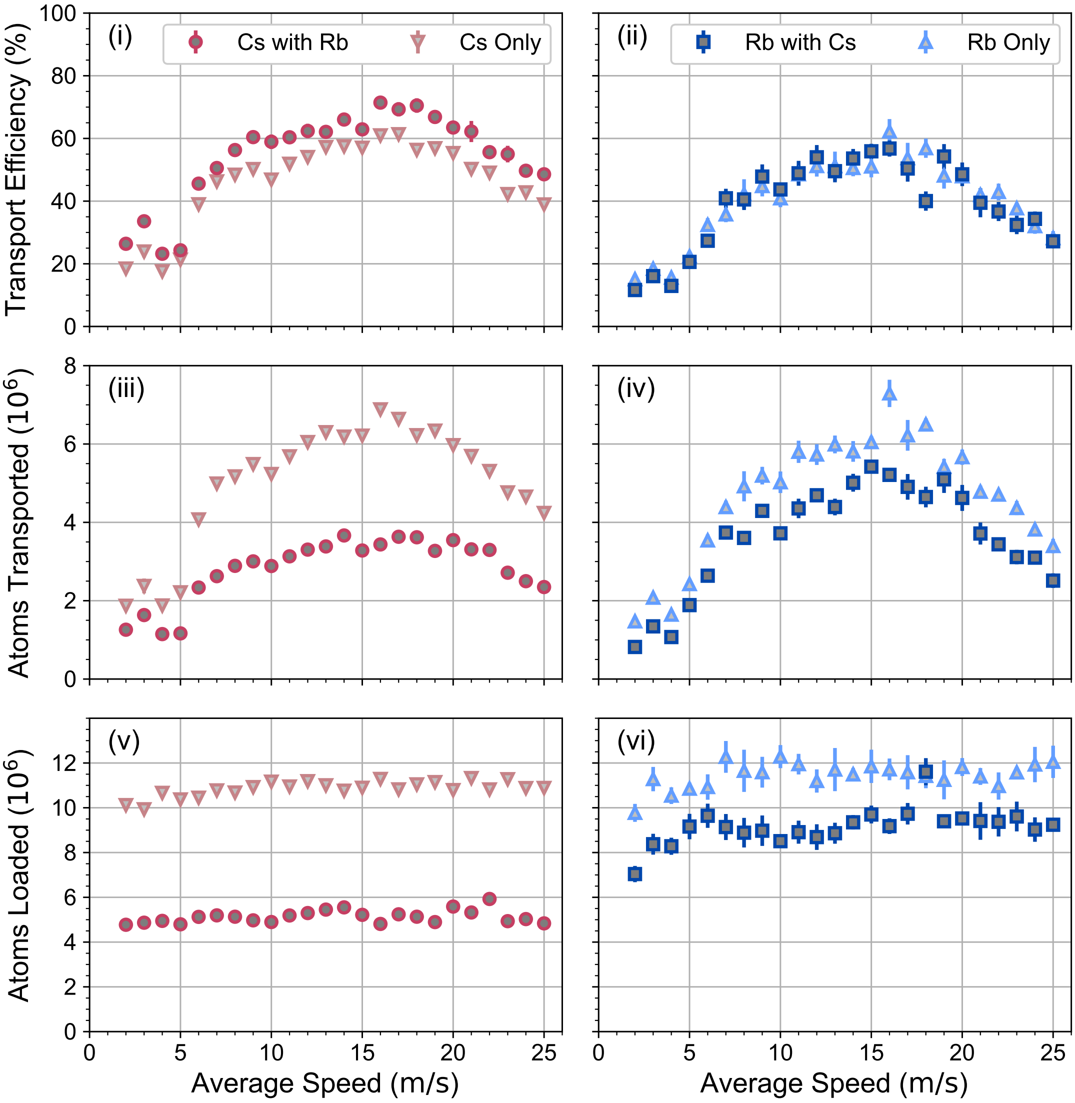

Figure 4.11: Characterising dual-species transport of Rb and Cs. The dependence of the efficiency on the average speed is presented for both dual-species and single-species transport. Different laser cooling routines are used for the dual-species and single species measurements resulting in different initial atom numbers (see text for details). (i) Shows the Cs transport efficiencies for a single-species sequence and for a dual-species routine, while (ii) shows the same for Rb. In (iii) and (iv) the number of Cs and Rb atoms transported to the Science Cell are shown respectively. Finally, (v) and (vi) show the number of atoms loaded into the optical conveyor-belt in the MOT Chamber, for Cs and Rb respectively.

the measurements were taken on the same day for consistency. The transport efficiency of both Cs and Rb is not negatively affected by the presence of the other species, as shown in panels (i) and (ii) respectively. In fact for Cs there is actually a slight increase in the transport efficiency. This probably results from thermalisation with Rb prior to and during the optical conveyor-belt loading. This is a consequence of the large interspecies scattering length of $\approx 650a_0$ [173] and the fact that Rb gas experiences shallower traps than Cs throughout and is therefore expected to be colder. However, the interpretation is complicated by the fact that the routine we use to simultaneously cool and load both species results in significantly fewer atoms in the transport lattice initially.

However the number of atoms transported is reduced for both Cs and Rb when both species are loaded, shown in panels (iii) and (iv) respectively. Cs suffers the greater reduction of around a factor of two. This drop can however be explained entirely by the number of atoms loaded into the optical conveyor-belt in the MOT chamber, shown in panel (v) for Cs and panel (vi) for Rb, which shows an equivalent drop in atoms loaded with both species present.

The main cause of the decrease in the number of atoms loaded into the conveyor-belt is the sequence used to prepare dual species samples in the MOT chamber. For the dual-species routine, the initial cooling steps (MOT, compressed MOT and DRSC) were performed simultaneously. The two species were loaded into the MOT chamber reservoir trap before being transferred into the conveyor-belt. The two species must therefore share some parameters and the timing of each stage can no longer be independently optimised for the two species and a compromise must be found. In particular, for the DRSC stage we find that a duration of 15ms is optimum for Rb alone, whereas 5ms is optimum for Cs alone. Additionally, the two MOTs loaded optimally at different gradient fields. For the measurements shown in Figure 4.11 we used a routine that favoured Rb, leading to a $\approx 50\%$ reduction in the number of Cs atoms loaded into the lattice from $\approx 1.0 \times 10^7$ to $\approx 5 \times 10^6$, whereas the number of Rb atoms was $9 \times 10^6$ compared to $\approx 1.0 \times 10^7$ for the single species routine.

Modifications to the laser systems used for DRSC and adjustments to the dual-

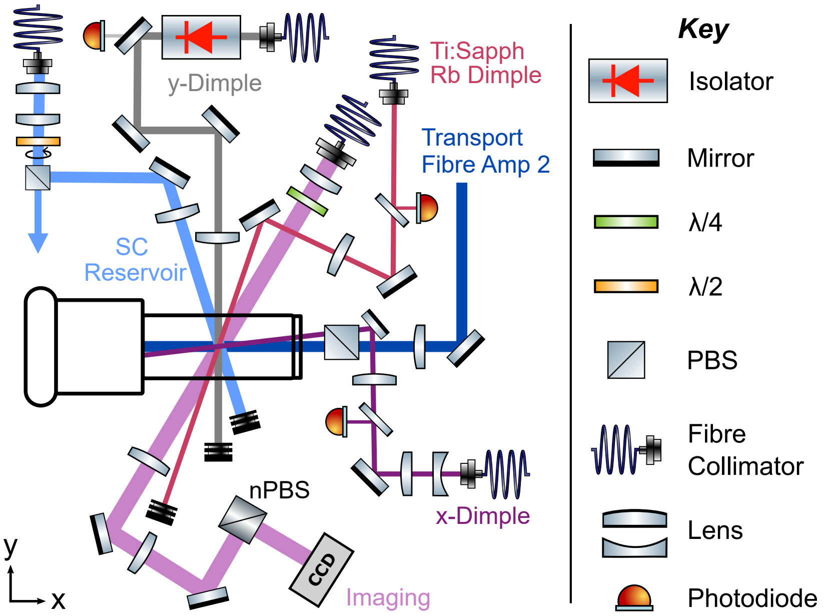

Figure 4.12: Optical setup of the dipole traps in the Science Cell that are used to produce Bose-Einstein Condensates of Cs or Rb. Photodiodes are used to servo the power in the dimple paths by controlling the RF power to an AOM before the respective optical fibre.

species cooling routine will allow better simultaneous preparation of Rb and Cs in the MOT chamber. This will lead to the transport of a greater number of atoms to the Science Cell and enable future experiments. Nevertheless, the current results clearly demonstrate that efficient dual-species transport of Rb and Cs is possible using a relatively simple optical conveyor-belt setup, as no additional losses are incurred from the transport with the second species present.

## 4.4 Evaporation to Bose-Einstein Condensate

This sections briefly discusses the production of a Bose-Einstein condensate (BEC) of Rb or Cs. A more in-depth description can be found in Jonathan Mortlock's thesis [155].

Following the transport to the Science Cell, the atoms are transferred into the optical dipole traps and evaporatively cooled to reach the BEC condensation transition. This is done using an all-optical evaporation scheme. We use the established approach for Cs [148] based upon initial loading into a large volume reservoir trap,

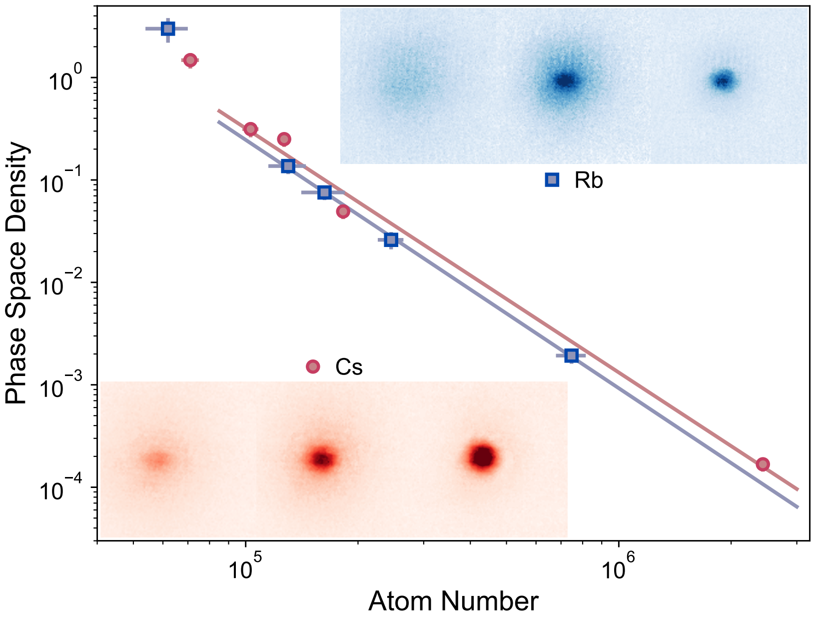

Figure 4.13: Production of a Bose-Einstein condensate (BEC) for Cs (red circles) and Rb (blue squares). The evaporation trajectories are shown with the phase space density plotted as a function of the atom number. Linear fits yield evaporation efficiencies of 2.4(5) for Rb and 2.38(15) for Cs. The insets show, from left to right, optical depth images of the clouds as they are cooled through the BEC transition.

followed by transfer into a tighter dimple trap. A similar approach is employed for Rb. This approach has been used for Rb-Cs mixtures [174].

The setup for the optical dipole traps used is found in Figure 4.12. The reservoir trap is formed from two beams. Transport beam 2, the lattice beam focused closest to the Science Cell, is retained while the other beam is ramped off to remove the lattice. Confinement along the transport axis is provided by an elliptical 1064nm beam with a horizontal waist of 510$\mu$m, a vertical waist of 200$\mu$m and a maximum power of 40W. These beam shapes are chosen to spatially mode match to the elongated shape of the cloud following transport, to maximise the number of atoms captured. Around $2.3(1) \times 10^6$ Cs and $2.1(1) \times 10^6$ Rb atoms are captured in the reservoir trap, at temperatures $\approx 5\mu$K. The Science Cell magnetic coils provide a gradient field of 31G/cm and a bias field of 40G to compensate for gravitational tilting.

The dimple trap is formed by a pair of more tightly focused 1064nm beams. The $x$-dimple has a waist of 45$\mu$m and the $y$-dimple has a waist of 100$\mu$m. These relatively large dimple waists are chosen to limit the three-body loss for Cs in the final stages of evaporation [148]. To avoid forming accidental lattices, all 1064nm beams used in evaporation are mutually detuned by at least 80MHz. The dimple trap is loaded by ramping on the beams to depth to around 10$\mu$K in 100ms. Effective loading of the dimple trap requires a high collision rate in the gas and fast thermalisation. For Cs this is achieved via the high s-wave length to $\approxeq 870\,a_0$ at the applied bias field of 40G. For Rb evaporation, an additional 50$\mu$m dipole trap at 830nm, derived from a Ti:Sapphire laser, is used. This beam is used to achieve higher trap frequencies and hence an increased collision rate.

After loading into the dimple trap, the atoms are cooled to degeneracy using forced evaporation. This proceeds by first ramping off the reservoir trap in 2s. For Rb the 830nm beam is also ramped off in this step to reduce heating from near-resonant photon scattering. Then the power in the dimple is ramped down linearly in two 2s steps. During these steps the magnetic gradient field is reduced to slightly tilt the trap in the vertical direction. During the final step the tilt of the trap is increased to maintain sufficiently high trap frequencies and collision rate for efficient cooling [175]. For each step the levitation field and dipole trap powers are optimised to maximise the evaporation efficiency. For Cs it is important to lower the magnetic field to the 3-body loss minimum at 22G during the final two steps of evaporation.

Figure 4.13 shows the evaporation trajectory to BEC for both Rb and Cs independently. The atom number and temperature are measured using absorption imaging following time-of-flight expansion. The trap frequencies are calibrated by measuring centre-of-mass oscillations for various trap powers. These quantities are combined to calculate the phase space density for each point. The evaporation efficiency is defined by

$$\gamma = \frac{d(\ln \rho)}{d(\ln N)} \tag{4.28}$$

where $\rho$ is the phase space density and $N$ the number of atoms. From fits to the data in the non-degenerate regime, the efficiencies are found to be 2.4(5) for Rb and 2.38(15) Cs.

The BEC transition is typically crossed with $4 \times 10^4$ Cs atoms or $5 \times 10^4$ Rb atoms. The insets to Figure 4.13 show representative absorption images taken after 45ms time-of-flight expansion. The ability to produce a BEC of either species in the Science Cell demonstrates the effectiveness of our transport scheme and is the starting point for future experiments.

# CHAPTER 5

# Conclusions

## 5.1 Summary

In this thesis the fast and efficient transport of Caesium and Rubidium atoms using an optical conveyor-belt has been demonstrated. Up to $7 \times 10^7$ atoms of either species can be transported across the 37.2cm gap between the MOT Chamber and the Science Cell in under 25ms. Once in the Science Cell, either species can be evaporatively cooled to form a Bose-Einstein condensate. Simultaneously loading both species into the optical-conveyor belt did not lead to a reduction in the transport efficiency of either species.

Our transport scheme was able to avoid the use of more complicated Bessel beams or variable-focus lenses by carefully choosing the the waists and focus positions. To that end detailed calculations of the trapping potential were performed to find the optimum beam parameters. It was found that separating the focus positions of the two transport beams can lead to dramatic increases in the minimum trap depth, as compared to the simplest case of both beams focussed at the centre of the transport path. The use of magnetic coils at the start and end of the transport path to compensate for the effect of gravity was also found to be highly beneficial. The differing effect of varying the beam parameters on the trap depths in the axial and radial directions was carefully balanced. Insight was gained into the axial trap depth via analytic optimisation of the beam parameters. Ultimately, beam waists of 195$\mu$m and focus positions 7.2cm from each end of the transport paths were found to be optimum.

The equations of motion of several different transport trajectories were derived. Trajectories were compared both theoretically and experimentally. The performance of the Minimum Jerk Trajectory was found to be the best, with that of the Minimum Snap Trajectory a close second. Further characterisation measurements were performed that allowed insight to be gained into different loss mechanism during transport.

## 5.2 Transport Improvements

Further improving the minimum trap depth is challenging, however there are a few different approaches that will be described here. Some of them are not applicable for our experiment but could prove useful for other experiments. After the optimisation of the trap depth in Section 2.5.3, the axial trap depth is limiting for all species. From analytic considerations of the axial depth it is also evident that only very marginal gains in the minimum trap depth are possible.

The primary way to increase the trap depth is to swap the current laser system for one with greater output power. For example, the manufacturer of our fibre amplifiers also produces 1064nm fibre amplifiers with 45W of output power, rather than 30W. If both fibre amplifiers were to be swapped out, the trap depth could thus be increased by 50%. However, replacing one of the two fibre amplifiers could also increase the achievable trap depth. In that case, the beam parameters need to be re-optimised to account for the asymmetry in beam powers. An example is shown in Figure 5.1(a), where fibre amplifier 1 has been upgraded.

The magnetic coils could be replaced. The range over which they are effective at counteracting gravity is determined by their radii. Replacing the existing coils with larger radius coils would increase the effectiveness of the levitation. In our

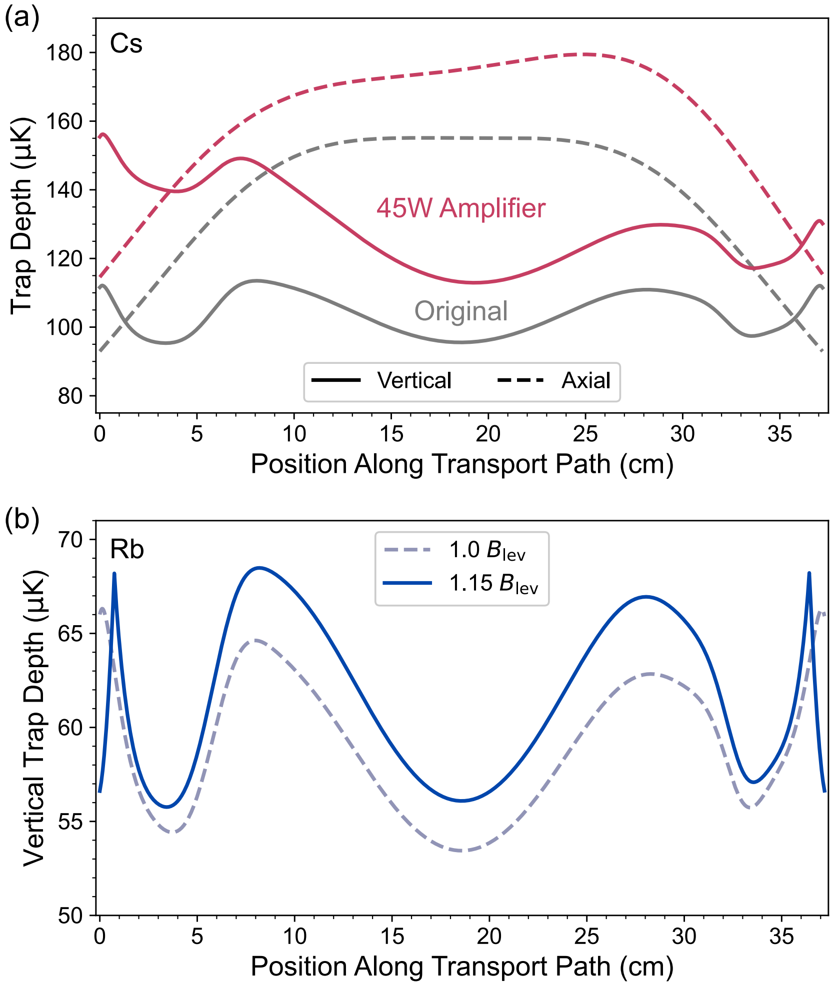

Figure 5.1: Possible improvements to the optical conveyor-belt trap depth. In both cases the new trap depths are compared against the original optimum beam parameters of 195$\mu$m and focus positions 7.2cm from the ends of the transport path. (a) Shows the effect on the Cs trap depths if fibre amplifier 1 were to be replaced with a higher power 45W amplifier. The beam parameters are re-optimised: transport beam 1 has waist of 202$\mu$m and focus position of 5.8cm while transport beam 2 has a waist of 192$\mu$m and a focus position of 30.5cm. (b) Shows the effect of overlevitating the atoms on the Rb trap depth in the vertical direction. The levitation gradient was optimised alongside the beam parameters. The optimum found to be 115% of the levitation gradient with beam waists 190$\mu$m and focus positions 7.5cm from each end of the transport path.

| $d$ (cm) | $x_0$ (cm) | $w_0$ ($\mu$m) | $\mathcal{U}_{\mathrm{Cs}}$ ($\mu$K) | $\mathcal{U}_{\mathrm{Rb}}$ ($\mu$K) |
|---|---|---|---|---|
| 30 | 4.5 | 157 | 98 | 55 |
| 35 | 5.1 | 177 | 75 | 41 |
| 37.2 | 5.5 | 180 | 66 | 36 |
| 40 | 6.0 | 185 | 57 | 31 |

Table 5.1: Comparison of the optimum beam parameters and trap depths achievable for different transport distances $d$ using 18W per beam and 1064nm. Magnetic levitation is not considered and the vertical depth is limiting for all distances.

experiment all four coil pairs were designed and made before optical conveyor-belt transport was investigated. For other experiments, the coils could be designed taking transport into account. However the sizes of coils used are often subject to space constraints. Additionally, larger radius coils will require greater currents to produce the same central gradient field. Alternatively, additional coil pairs could be added, although this could restrict the optical access of the experiment in the same way magnetic transport schemes can.

Another aspect that could be considered in more detail is the levitation gradient. The current through the coils could deliberately be set to produce on-axis gradient fields greater than the levitation gradient. This would partially counteract the drop-off of the gradient field. In such a scenario the beam shapes would also need to be re-optimised. An example of this is shown in Figure 5.1(b).

### 5.2.1 Different Transport Distances

In order to assess the dependence of the minimum trap depths achievable on the transport distance, the beam parameter optimisation was repeated for several different distances. The results are summarised in Table 5.1. The vertical and axial trap depths were optimised simultaneously, but magnetic levitation was excluded. As for the other calculations, the beams were taken to have symmetric waists and focus positions and 18W of power was assumed. For longer transport distances, longer Rayleigh ranges and hence larger waists are required, as can be expected intuitively. The optimum focus positions also increase, moving further from the ends of the transport path. The minimum trap depth falls off with distance but still remains above 50$\mu$K for Cs and above 30$\mu$K for Rb at a transport distance of 40cm.

## 5.3 Experimental Outlook

Fast and efficient dual-species transport of Rb and Cs lays a groundwork for the study of RbCs molecules in a quantum gas microscope. An important next step is to implement separate optical traps for Rb and Cs in the Science Cell, to enable the production of dual-species condensates [174]. The protocol for the preparation of heteronuclear atom pairs in a 3D optical lattice is established [78] and a compatible association sequence for the production of ground-state molecules has recently been demonstrated [176].

Single site resolved imaging of the molecules may be achieved by reversing the association sequence and detecting the resulting atoms using standard atomic quantum gas microscopy techniques [47, 48]. RbCs molecules are especially attractive in this regard as microscopy has been demonstrated for both atomic species using simple cooling techniques [66, 177]. Moreover, magic wavelength trapping has been demonstrated for rotational states in RbCs molecules [46,178] leading to second-scale rotational coherence and new opportunities for the simulation of models relating to quantum magnetism [18, 27, 179, 180].

# Bibliography

[1] I. Georgescu, S. Ashhab, and F. Nori, “Quantum simulation,” *Rev. Mod. Phys.*, vol. 86, pp. 153–185, Mar. 2014. 1, 1.1

[2] C. Gross and I. Bloch, “Quantum simulations with ultracold atoms in optical lattices,” *Science*, vol. 357, pp. 995–1001, Sept. 2017. 1, 1.1

[3] F. Schäfer, T. Fukuhara, S. Sugawa, Y. Takasu, and Y. Takahashi, “Tools for quantum simulation with ultracold atoms in optical lattices,” *Nature Reviews Physics*, vol. 2, pp. 411–425, Aug. 2020. 1, 1.1

[4] A. Browaeys and T. Lahaye, “Many-body physics with individually controlled Rydberg atoms,” *Nat. Phys.*, vol. 16, pp. 132–142, Feb. 2020. 1

[5] L. Henriet, L. Beguin, A. Signoles, T. Lahaye, A. Browaeys, G.-O. Reymond, and C. Jurczak, “Quantum computing with neutral atoms,” *Quantum*, vol. 4, p. 327, Sept. 2020. 1

[6] C. Degen, F. Reinhard, and P. Cappellaro, “Quantum sensing,” *Rev. Mod. Phys.*, vol. 89, p. 035002, July 2017. 1

[7] A. D. Ludlow, M. M. Boyd, J. Ye, E. Peik, and P. Schmidt, “Optical atomic clocks,” *Rev. Mod. Phys.*, vol. 87, pp. 637–701, June 2015. 1

[8] L. D. Carr, D. DeMille, R. V. Krems, and J. Ye, “Cold and ultracold molecules: science, technology and applications,” *New J. Phys.*, vol. 11, p. 055049, May 2009. 1

[9] W. D. Phillips, “Nobel Lecture: Laser cooling and trapping of neutral atoms,” *Rev. Mod. Phys.*, vol. 70, pp. 721–741, July 1998. 1

[10] S. Chu, “Nobel Lecture: The manipulation of neutral particles,” *Rev. Mod. Phys.*, vol. 70, pp. 685–706, July 1998. 1

[11] C. N. Cohen-Tannoudji, “Nobel Lecture: Manipulating atoms with photons,” *Rev. Mod. Phys.*, vol. 70, pp. 707–719, July 1998. 1

[12] H. J. Metcalf and P. van der Straten, *Laser Trapping and Cooling.* Springer, 1999. 1

[13] E. A. Cornell and C. E. Wieman, “Nobel Lecture: Bose-Einstein condensation in a dilute gas, the first 70 years and some recent experiments,” *Rev. Mod. Phys.*, vol. 74, pp. 875–893, Aug. 2002. 1

[14] W. Ketterle, “Nobel lecture: When atoms behave as waves: Bose-Einstein condensation and the atom laser,” *Rev. Mod. Phys.*, vol. 74, pp. 1131–1151, Nov. 2002. 1

[15] C. J. Foot, *Atomic Physics.* Oxford University Press, 2005. 1, 2.3.5, 2.3.5

[16] C. Cohen-Tannoudji and D. Guéry-Odelin, *Advances in Atomic Phyics.* World Scientific, 2011. 1

[17] G. Nemova, *Field Guide to Laser Cooling Methods.* SPIE Press, 2019. 1, 2.3.5

[18] R. Barnett, D. Petrov, M. Lukin, and E. Demler, “Quantum Magnetism with Multicomponent Dipolar Molecules in an Optical Lattice,” *Phys. Rev. Lett.*, vol. 96, p. 190401, May 2006. 1, 5.3

[19] A. Micheli, G. K. Brennen, and P. Zoller, “A toolbox for lattice-spin models with polar molecules,” *Nat. Phys.*, vol. 2, pp. 341–347, May 2006. 1

[20] H. P. Büchler, E. Demler, M. Lukin, A. Micheli, N. Prokof’ev, G. Pupillo, and P. Zoller, “Strongly Correlated 2D Quantum Phases with Cold Polar Molecules: Controlling the Shape of the Interaction Potential,” *Phys. Rev. Lett.*, vol. 98, p. 060404, Feb. 2007. 1

[21] A. V. Gorshkov, S. R. Manmana, G. Chen, E. Demler, M. D. Lukin, and A. M. Rey, “Quantum magnetism with polar alkali-metal dimers,” *Phys. Rev. A*, vol. 84, p. 033619, Sept. 2011. 1

[22] M. A. Baranov, M. Dalmonte, G. Pupillo, and P. Zoller, “Condensed Matter Theory of Dipolar Quantum Gases,” *Chem. Rev.*, vol. 112, pp. 5012–5061, Sept. 2012. 1

[23] I. Bloch, J. Dalibard, and S. Nascimbène, “Quantum simulations with ultracold quantum gases,” *Nat. Phys.*, vol. 8, pp. 267–276, Apr. 2012. 1

[24] A. Macia, D. Hufnagl, F. Mazzanti, J. Boronat, and R. E. Zillich, “Excitations and Stripe Phase Formation in a Two-Dimensional Dipolar Bose Gas with Tilted Polarization,” *Phys. Rev. Lett.*, vol. 109, p. 235307, Dec. 2012. 1

[25] S. R. Manmana, E. M. Stoudenmire, K. R. A. Hazzard, A. M. Rey, and A. V. Gorshkov, “Topological phases in ultracold polar-molecule quantum magnets,” *Phys. Rev. B*, vol. 87, p. 081106, Feb. 2013. 1

[26] A. V. Gorshkov, K. R. Hazzard, and A. M. Rey, “Kitaev honeycomb and other exotic spin models with polar molecules,” *Mol. Phys.*, vol. 111, pp. 1908–1916, July 2013. 1

[27] J. A. Blackmore, L. Caldwell, P. D. Gregory, E. M. Bridge, R. Sawant, J. Aldegunde, J. Mur-Petit, D. Jaksch, J. M. Hutson, B. E. Sauer, M. R. Tarbutt, and S. L. Cornish, "Ultracold molecules for quantum simulation: rotational coherences in CaF and RbCs," *Quantum Sci. Technol.*, vol. 4, p. 014010, Dec. 2018. 1, 5.3

[28] D. DeMille, "Quantum Computation with Trapped Polar Molecules," *Phys. Rev. Lett.*, vol. 88, p. 067901, Jan. 2002. 1

[29] S. F. Yelin, K. Kirby, and R. Côté, "Schemes for robust quantum computation with polar molecules," *Phys. Rev. A*, vol. 74, p. 050301, Nov. 2006. 1

[30] J. Zhu, S. Kais, Q. Wei, D. Herschbach, and B. Friedrich, "Implementation of quantum logic gates using polar molecules in pendular states," *J. Chem. Phys.*, vol. 138, p. 024104, Jan. 2013. 1

[31] F. Herrera, Y. Cao, S. Kais, and K. B. Whaley, "Infrared-dressed entanglement of cold open-shell polar molecules for universal matchgate quantum computing," *New J. Phys.*, vol. 16, p. 075001, July 2014. 1

[32] K.-K. Ni, T. Rosenband, and D. D. Grimes, "Dipolar exchange quantum logic gate with polar molecules," *Chem. Sci.*, vol. 9, pp. 6830–6838, Aug. 2018. 1

[33] M. Hughes, M. D. Frye, R. Sawant, G. Bhole, J. A. Jones, S. L. Cornish, M. R. Tarbutt, J. M. Hutson, D. Jaksch, and J. Mur-Petit, "Robust entangling gate for polar molecules using magnetic and microwave fields," *Phys. Rev. A*, vol. 101, p. 062308, June 2020. 1

[34] R. Sawant, J. A. Blackmore, P. D. Gregory, J. Mur-Petit, D. Jaksch, J. Aldegunde, J. M. Hutson, M. R. Tarbutt, and S. L. Cornish, "Ultracold polar molecules as qudits," *New J. Phys.*, vol. 22, p. 013027, Jan. 2020. 1

[35] V. V. Flambaum and M. G. Kozlov, "Enhanced Sensitivity to the Time Variation of the Fine-Structure Constant and $m_p/m_e$ in Diatomic Molecules," *Phys. Rev. Lett.*, vol. 99, p. 150801, Oct. 2007. 1

[36] T. A. Isaev, S. Hoekstra, and R. Berger, "Laser-cooled RaF as a promising candidate to measure molecular parity violation," *Phys. Rev. A*, vol. 82, p. 052521, Nov. 2010. 1

[37] J. J. Hudson, D. M. Kara, I. J. Smallman, B. E. Sauer, M. R. Tarbutt, and E. A. Hinds, "Improved measurement of the shape of the electron," *Nature*, vol. 473, pp. 493–496, May 2011. 1

[38] THE ACME COLLABORATION, J. Baron, W. C. Campbell, D. DeMille, J. M. Doyle, G. Gabrielse, Y. V. Gurevich, P. W. Hess, N. R. Hutzler, E. Kirilov, I. Kozyryev, B. R. O'Leary, C. D. Panda, M. F. Parsons, E. S. Petrik, B. Spaun, A. C. Vutha, and A. D. West, "Order of Magnitude Smaller Limit on the Electric Dipole Moment of the Electron," *Science*, vol. 343, pp. 269–272, Jan. 2014. 1

[39] B. Gadway and B. Yan, “Strongly interacting ultracold polar molecules,” *J. Phys. B: At., Mol. Opt. Phys.*, vol. 49, p. 152002, June 2016. 1

[40] S. A. Moses, J. P. Covey, M. T. Miecnikowski, D. S. Jin, and J. Ye, “New frontiers for quantum gases of polar molecules,” *Nat. Phys.*, vol. 13, pp. 13–20, Jan. 2017. 1

[41] J. W. Park, Z. Z. Yan, H. Loh, S. A. Will, and M. W. Zwierlein, “Second-scale nuclear spin coherence time of ultracold 23Na40K molecules,” *Science*, vol. 357, pp. 372–375, July 2017. 1

[42] L. Caldwell, H. Williams, N. Fitch, J. Aldegunde, J. M. Hutson, B. Sauer, and M. Tarbutt, “Long Rotational Coherence Times of Molecules in a Magnetic Trap,” *Phys. Rev. Lett.*, vol. 124, p. 063001, Feb. 2020. 1

[43] P. D. Gregory, J. A. Blackmore, S. L. Bromley, J. M. Hutson, and S. L. Cornish, “Robust storage qubits in ultracold polar molecules,” *Nat. Phys.*, vol. 17, pp. 1149–1153, Oct. 2021. 1

[44] S. Burchesky, L. Anderegg, Y. Bao, S. S. Yu, E. Chae, W. Ketterle, K.-K. Ni, and J. M. Doyle, “Rotational Coherence Times of Polar Molecules in Optical Tweezers,” *Phys. Rev. Lett.*, vol. 127, p. 123202, Sept. 2021. 1

[45] J. Lin, J. He, M. Jin, G. Chen, and D. Wang, “Seconds-Scale Coherence on Nuclear Spin Transitions of Ultracold Polar Molecules in 3D Optical Lattices,” *Phys. Rev. Lett.*, vol. 128, p. 223201, June 2022. 1

[46] P. D. Gregory, L. Fernley, A. L. Tao, S. L. Bromley, J. Stepp, Z. Zhang, S. Kotochigova, K. R. A. Hazzard, and S. L. Cornish, “Second-scale rotational coherence and dipolar interactions in a gas of ultracold polar molecules.” Preprint, 2023. 1, 5.3

[47] J. S. Rosenberg, L. Christakis, E. Guardado-Sanchez, Z. Z. Yan, and W. S. Bakr, “Observation of the Hanbury Brown–Twiss effect with ultracold molecules,” *Nat. Phys.*, vol. 18, pp. 1062–1066, Sept. 2022. 1, 1.1, 5.3

[48] L. Christakis, J. S. Rosenberg, R. Raj, S. Chi, A. Morningstar, D. A. Huse, Z. Z. Yan, and W. S. Bakr, “Probing site-resolved correlations in a spin system of ultracold molecules,” *Nature*, vol. 614, pp. 64–69, Feb. 2023. 1, 5.3

[49] D. Leibfried, B. DeMarco, V. Meyer, M. Rowe, A. Ben-Kish, J. Britton, W. M. Itano, B. Jelenković, C. Langer, T. Rosenband, and D. J. Wineland, “Trapped-Ion Quantum Simulator: Experimental Application to Nonlinear Interferometers,” *Phys. Rev. Lett.*, vol. 89, p. 247901, Nov. 2002. 1

[50] A. Friedenauer, H. Schmitz, J. T. Glueckert, D. Porras, and T. Schaetz, “Simulating a quantum magnet with trapped ions,” *Nat. Phys.*, vol. 4, pp. 757–761, Oct. 2008. 1

[51] R. Blatt and C. F. Roos, “Quantum simulations with trapped ions,” *Nat. Phys.*, vol. 8, pp. 277–284, Apr. 2012. 1

[52] M. Neeley, M. Ansmann, R. C. Bialczak, M. Hofheinz, E. Lucero, A. D. O'Connell, D. Sank, H. Wang, J. Wenner, A. N. Cleland, M. R. Geller, and J. M. Martinis, "Emulation of a Quantum Spin with a Superconducting Phase Qudit," *Science*, vol. 325, pp. 722–725, Aug. 2009. 1

[53] A. A. Houck, H. E. Türeci, and J. Koch, "On-chip quantum simulation with superconducting circuits," *Nat. Phys.*, vol. 8, pp. 292–299, Apr. 2012. 1

[54] A. Griesmaier, J. Werner, S. Hensler, J. Stuhler, and T. Pfau, "Bose-Einstein Condensation of Chromium," *Phys. Rev. Lett.*, vol. 94, p. 160401, Apr. 2005. 1

[55] M. Lu, N. Q. Burdick, S. H. Youn, and B. L. Lev, "Strongly Dipolar Bose-Einstein Condensate of Dysprosium," *Phys. Rev. Lett.*, vol. 107, p. 190401, Oct. 2011. 1

[56] K. Aikawa, A. Frisch, M. Mark, S. Baier, A. Rietzler, R. Grimm, and F. Ferlaino, "Bose-Einstein Condensation of Erbium," *Phys. Rev. Lett.*, vol. 108, p. 210401, May 2012. 1

[57] S. Baier, M. J. Mark, D. Petter, K. Aikawa, L. Chomaz, Z. Cai, M. Baranov, P. Zoller, and F. Ferlaino, "Extended Bose-Hubbard models with ultracold magnetic atoms," *Science*, vol. 352, pp. 201–205, Apr. 2016. 1

[58] H. Weimer, M. Müller, I. Lesanovsky, P. Zoller, and H. P. Büchler, "A Rydberg quantum simulator," *Nat. Phys.*, vol. 6, pp. 382–388, May 2010. 1

[59] P. Scholl, M. Schuler, H. J. Williams, A. A. Eberharter, D. Barredo, K.-N. Schymik, V. Lienhard, L.-P. Henry, T. C. Lang, T. Lahaye, A. M. Läuchli, and A. Browaeys, "Quantum simulation of 2D antiferromagnets with hundreds of Rydberg atoms," *Nature*, vol. 595, pp. 233–238, July 2021. 1

[60] J. A. Sauer, K. M. Fortier, M. S. Chang, C. D. Hamley, and M. S. Chapman, "Cavity QED with optically transported atoms," *Phys. Rev. A*, vol. 69, no. 5, p. 051804, 2004. 1.1

[61] G. T. Hickman and M. Saffman, "Speed, retention loss, and motional heating of atoms in an optical conveyor belt," *Phys. Rev. A*, vol. 101, p. 063411, June 2020. 1.1, 3.2.2, 4.1.1, 4.1.5

[62] S. Okaba, T. Takano, F. Benabid, T. Bradley, L. Vincetti, Z. Maizelis, V. Yampol'skii, F. Nori, and H. Katori, "Lamb-Dicke spectroscopy of atoms in a hollow-core photonic crystal fibre," *Nat. Commun.*, vol. 5, p. 4096, June 2014. 1.1

[63] M. Langbecker, R. Wirtz, F. Knoch, M. Noaman, T. Speck, and P. Windpassinger, "Highly controlled optical transport of cold atoms into a hollow-core fiber," *New J. Phys.*, vol. 20, p. 083038, Aug. 2018. 1.1, 4.1.1

[64] P. Schneeweiss, S. T. Dawkins, R. Mitsch, D. Reitz, E. Vetsch, and A. Rauschenbeutel, “A nanofiber-based optical conveyor belt for cold atoms,” *Appl. Phys. B*, vol. 110, pp. 279–283, Mar. 2013. 1.1

[65] S. Schmid, A. Härter, and J. H. Denschlag, “Dynamics of a Cold Trapped Ion in a Bose-Einstein Condensate,” *Phys. Rev. Lett.*, vol. 105, p. 133202, Sept. 2010. 1.1, 2.1

[66] W. S. Bakr, J. I. Gillen, A. Peng, S. Fölling, and M. Greiner, “A quantum gas microscope for detecting single atoms in a Hubbard-regime optical lattice,” *Nature*, vol. 462, pp. 74–77, Nov. 2009. 1.1, 5.3

[67] J. F. Sherson, C. Weitenberg, M. Endres, M. Cheneau, I. Bloch, and S. Kuhr, “Single-atom-resolved fluorescence imaging of an atomic Mott insulator,” *Nature*, vol. 467, pp. 68–72, Sept. 2010. 1.1

[68] L. W. Cheuk, M. A. Nichols, M. Okan, T. Gersdorf, V. V. Ramasesh, W. S. Bakr, T. Lompe, and M. W. Zwierlein, “Quantum-Gas Microscope for Fermionic Atoms,” *Phys. Rev. Lett.*, vol. 114, p. 193001, May 2015. 1.1

[69] G. J. A. Edge, R. Anderson, D. Jervis, D. C. McKay, R. Day, S. Trotzky, and J. H. Thywissen, “Imaging and addressing of individual fermionic atoms in an optical lattice,” *Phys. Rev. A*, vol. 92, p. 063406, Dec. 2015. 1.1

[70] E. Haller, J. Hudson, A. Kelly, D. A. Cotta, B. Peaudecerf, G. D. Bruce, and S. Kuhr, “Single-atom imaging of fermions in a quantum-gas microscope,” *Nat. Phys.*, vol. 11, pp. 738–742, Sept. 2015. 1.1

[71] M. F. Parsons, F. Huber, A. Mazurenko, C. S. Chiu, W. Setiawan, K. Wooley-Brown, S. Blatt, and M. Greiner, “Site-Resolved Imaging of Fermionic $^6$li in an Optical Lattice,” *Phys. Rev. Lett.*, vol. 114, p. 213002, May 2015. 1.1

[72] A. Omran, M. Boll, T. A. Hilker, K. Kleinlein, G. Salomon, I. Bloch, and C. Gross, “Microscopic Observation of Pauli Blocking in Degenerate Fermionic Lattice Gases,” *Phys. Rev. Lett.*, vol. 115, p. 263001, Dec. 2015. 1.1

[73] R. Yamamoto, J. Kobayashi, T. Kuno, K. Kato, and Y. Takahashi, “An ytterbium quantum gas microscope with narrow-line laser cooling,” *New J. Phys.*, vol. 18, p. 023016, Feb. 2016. 1.1

[74] Z. Hadzibabic, C. A. Stan, K. Dieckmann, S. Gupta, M. W. Zwierlein, A. Görlitz, and W. Ketterle, “Two-Species Mixture of Quantum Degenerate Bose and Fermi Gases,” *Phys. Rev. Lett.*, vol. 88, p. 160401, Apr. 2002. 1.1

[75] C. Silber, S. Günther, C. Marzok, B. Deh, P. W. Courteille, and C. Zimmermann, “Quantum-Degenerate Mixture of Fermionic Lithium and Bosonic Rubidium Gases,” *Phys. Rev. Lett.*, vol. 95, p. 170408, Oct. 2005. 1.1

[76] F. Wang, X. Li, D. Xiong, and D. Wang, "A double species 23Na and 87Rb Bose–Einstein condensate with tunable miscibility via an interspecies Feshbach resonance," *J. Phys. B: At., Mol. Opt. Phys.*, vol. 49, p. 015302, Nov. 2015. 1.1

[77] B. DeSalvo, K. Patel, J. Johansen, and C. Chin, "Observation of a Degenerate Fermi Gas Trapped by a Bose-Einstein Condensate," *Phys. Rev. Lett.*, vol. 119, p. 233401, Dec. 2017. 1.1

[78] L. Reichsöllner, A. Schindewolf, T. Takekoshi, R. Grimm, and H.-C. Nägerl, "Quantum Engineering of a Low-Entropy Gas of Heteronuclear Bosonic Molecules in an Optical Lattice," *Phys. Rev. Lett.*, vol. 118, p. 073201, Feb. 2017. 1.1, 5.3

[79] A. Burchianti, C. D'Errico, S. Rosi, A. Simoni, M. Modugno, C. Fort, and F. Minardi, "Dual-species Bose-Einstein condensate of $^{41}$K and $^{87}$Rb in a hybrid trap," *Phys. Rev. A*, vol. 98, p. 063616, Dec. 2018. 1.1

[80] B. J. DeSalvo, K. Patel, G. Cai, and C. Chin, "Observation of fermion-mediated interactions between bosonic atoms," *Nature*, vol. 568, pp. 61–64, Apr. 2019. 1.1

[81] S.-K. Tung, K. Jiménez-García, J. Johansen, C. V. Parker, and C. Chin, "Geometric Scaling of Efimov States in a $^{6}$ Li - $^{133}$Cs Mixture," *Phys. Rev. Lett.*, vol. 113, p. 240402, Dec. 2014. 1.1

[82] R. Maier, M. Eisele, E. Tiemann, and C. Zimmermann, "Efimov Resonance and Three-Body Parameter in a Lithium-Rubidium Mixture," *Phys. Rev. Lett.*, vol. 115, p. 043201, July 2015. 1.1

[83] J. Ulmanis, S. Häfner, R. Pires, E. D. Kuhnle, Y. Wang, C. H. Greene, and M. Weidemüller, "Heteronuclear Efimov Scenario with Positive Intraspecies Scattering Length," *Phys. Rev. Lett.*, vol. 117, p. 153201, Oct. 2016. 1.1

[84] J. Johansen, B. J. DeSalvo, K. Patel, and C. Chin, "Testing universality of Efimov physics across broad and narrow Feshbach resonances," *Nat. Phys.*, vol. 13, pp. 731–735, Aug. 2017. 1.1

[85] M. Cetina, M. Jag, R. S. Lous, I. Fritsche, J. T. M. Walraven, R. Grimm, J. Levinsen, M. M. Parish, R. Schmidt, M. Knap, and E. Demler, "Ultrafast many-body interferometry of impurities coupled to a Fermi sea," *Science*, vol. 354, pp. 96–99, Oct. 2016. 1.1

[86] M. Gröbner, P. Weinmann, F. Meinert, K. Lauber, E. Kirilov, and H.-C. Nägerl, "A new quantum gas apparatus for ultracold mixtures of K and Cs and KCs ground-state molecules," *J. Mod. Opt.*, vol. 63, pp. 1829–1839, Oct. 2016. 1.1, 1.3

[87] K.-K. Ni, S. Ospelkaus, M. H. G. de Miranda, A. Pe'er, B. Neyenhuis, J. J. Zirbel, S. Kotochigova, P. S. Julienne, D. S. Jin, and J. Ye, "A High Phase-Space-Density Gas of Polar Molecules," *Science*, vol. 322, pp. 231–235, Oct. 2008. 1.1

[88] T. Takekoshi, L. Reichsöllner, A. Schindewolf, J. M. Hutson, C. R. Le Sueur, O. Dulieu, F. Ferlaino, R. Grimm, and H.-C. Nägerl, "Ultracold Dense Samples of Dipolar RbCs Molecules in the Rovibrational and Hyperfine Ground State," *Phys. Rev. Lett.*, vol. 113, p. 205301, Nov. 2014. 1.1

[89] P. K. Molony, P. D. Gregory, Z. Ji, B. Lu, M. P. Köppinger, C. R. Le Sueur, C. L. Blackley, J. M. Hutson, and S. L. Cornish, "Creation of Ultracold $^{87}$rb$^{133}$cs Molecules in the Rovibrational Ground State," *Phys. Rev. Lett.*, vol. 113, p. 255301, Dec. 2014. 1.1

[90] J. W. Park, S. A. Will, and M. W. Zwierlein, "Ultracold Dipolar Gas of Fermionic $^{23}$na$^{40}$k Molecules in Their Absolute Ground State," *Phys. Rev. Lett.*, vol. 114, p. 205302, May 2015. 1.1

[91] P. K. Molony, P. D. Gregory, A. Kumar, C. R. Le Sueur, J. M. Hutson, and S. L. Cornish, "Production of Ultracold 87Rb133Cs in the Absolute Ground State: Complete Characterisation of the Stimulated Raman Adiabatic Passage Transfer," *ChemPhysChem*, vol. 17, no. 22, pp. 3811–3817, 2016. 1.1

[92] M. Guo, B. Zhu, B. Lu, X. Ye, F. Wang, R. Vexiau, N. Bouloufa-Maafa, G. Quéméner, O. Dulieu, and D. Wang, "Creation of an Ultracold Gas of Ground-State Dipolar $^{23}$na$^{87}$rb Molecules," *Phys. Rev. Lett.*, vol. 116, p. 205303, May 2016. 1.1

[93] T. M. Rvachov, H. Son, A. T. Sommer, S. Ebadi, J. J. Park, M. W. Zwierlein, W. Ketterle, and A. O. Jamison, "Long-Lived Ultracold Molecules with Electric and Magnetic Dipole Moments," *Phys. Rev. Lett.*, vol. 119, p. 143001, Oct. 2017. 1.1

[94] F. Seeßelberg, N. Buchheim, Z.-K. Lu, T. Schneider, X.-Y. Luo, E. Tiemann, I. Bloch, and C. Gohle, "Modeling the adiabatic creation of ultracold polar $^{23}$na$^{40}$k molecules," *Phys. Rev. A*, vol. 97, p. 013405, Jan. 2018. 1.1

[95] L. De Marco, G. Valtolina, K. Matsuda, W. G. Tobias, J. P. Covey, and J. Ye, "A degenerate Fermi gas of polar molecules," *Science*, vol. 363, pp. 853–856, Feb. 2019. 1.1

[96] K. K. Voges, P. Gersema, M. Meyer zum Alten Borgloh, T. A. Schulze, T. Hartmann, A. Zenesini, and S. Ospelkaus, "Ultracold gas of bosonic $^{23}$na$^{39}$k ground-state molecules," *Phys. Rev. Lett.*, vol. 125, p. 083401, Aug. 2020. 1.1

[97] H. Son, J. J. Park, W. Ketterle, and A. O. Jamison, "Collisional cooling of ultracold molecules," *Nature*, vol. 580, pp. 197–200, Apr. 2020. 1.1

[98] W. B. Cairncross, J. T. Zhang, L. R. Picard, Y. Yu, K. Wang, and K.-K. Ni, "Assembly of a Rovibrational Ground State Molecule in an Optical Tweezer," *Phys. Rev. Lett.*, vol. 126, p. 123402, Mar. 2021. 1.1

[99] A. Schindewolf, R. Bause, X.-Y. Chen, M. Duda, T. Karman, I. Bloch, and X.-Y. Luo, "Evaporation of microwave-shielded polar molecules to quantum degeneracy," *Nature*, vol. 607, pp. 677–681, July 2022. 1.1

[100] I. Stevenson, A. Z. Lam, N. Bigagli, C. Warner, W. Yuan, S. Zhang, and S. Will, "Ultracold Gas of Dipolar NaCs Ground State Molecules," *Phys. Rev. Lett.*, vol. 130, p. 113002, Mar. 2023. 1.1

[101] M. L. Wall, K. Maeda, and L. D. Carr, "Simulating quantum magnets with symmetric top molecules," *Ann. Phys.*, vol. 525, no. 10-11, pp. 845–865, 2013. 1.1

[102] J. F. Barry, D. J. McCarron, E. B. Norrgard, M. H. Steinecker, and D. DeMille, "Magneto-optical trapping of a diatomic molecule," *Nature*, vol. 512, pp. 286–289, Aug. 2014. 1.1

[103] M. L. Wall, K. Maeda, and L. D. Carr, "Realizing unconventional quantum magnetism with symmetric top molecules," *New J. Phys.*, vol. 17, p. 025001, Feb. 2015. 1.1

[104] S. Truppe, H. J. Williams, M. Hambach, L. Caldwell, N. J. Fitch, E. A. Hinds, B. E. Sauer, and M. R. Tarbutt, "Molecules cooled below the Doppler limit," *Nat. Phys.*, vol. 13, pp. 1173–1176, Dec. 2017. 1.1

[105] L. Anderegg, B. L. Augenbraun, E. Chae, B. Hemmerling, N. R. Hutzler, A. Ravi, A. Collopy, J. Ye, W. Ketterle, and J. M. Doyle, "Radio Frequency Magneto-Optical Trapping of CaF with High Density," *Phys. Rev. Lett.*, vol. 119, p. 103201, Sept. 2017. 1.1

[106] A. L. Collopy, S. Ding, Y. Wu, I. A. Finneran, L. Anderegg, B. L. Augenbraun, J. M. Doyle, and J. Ye, "3D Magneto-Optical Trap of Yttrium Monoxide," *Phys. Rev. Lett.*, vol. 121, p. 213201, Nov. 2018. 1.1

[107] P. Yu, L. W. Cheuk, I. Kozyryev, and J. M. Doyle, "A scalable quantum computing platform using symmetric-top molecules," *New J. Phys.*, vol. 21, p. 093049, Sept. 2019. 1.1

[108] L. Anderegg, L. W. Cheuk, Y. Bao, S. Burchesky, W. Ketterle, K.-K. Ni, and J. M. Doyle, "An optical tweezer array of ultracold molecules," *Science*, vol. 365, pp. 1156–1158, Sept. 2019. 1.1

[109] N. B. Vilas, C. Hallas, L. Anderegg, P. Robichaud, A. Winnicki, D. Mitra, and J. M. Doyle, "Magneto-optical trapping and sub-Doppler cooling of a polyatomic molecule," *Nature*, vol. 606, pp. 70–74, June 2022. 1.1

[110] H. J. Lewandowski, D. M. Harber, D. L. Whitaker, and E. A. Cornell, "Observation of Anomalous Spin-State Segregation in a Trapped Ultracold Vapor," *Phys. Rev. Lett.*, vol. 88, p. 070403, Jan. 2002. 1.2

[111] K. Nakagawa, Y. Suzuki, M. Horikoshi, and J. Kim, "Simple and efficient magnetic transport of cold atoms using moving coils for the production of Bose–Einstein condensation," *Appl. Phys. B*, vol. 81, pp. 791–794, Oct. 2005. 1.2

[112] D. Pertot, D. Greif, S. Albert, B. Gadway, and D. Schneble, "Versatile transporter apparatus for experiments with optically trapped Bose–Einstein condensates," *J. Phys. B: At., Mol. Opt. Phys.*, vol. 42, no. 21, p. 215305, 2009. 1.2

[113] S. Händel, T. P. Wiles, A. L. Marchant, S. A. Hopkins, C. S. Adams, and S. L. Cornish, "Magnetic merging of ultracold atomic gases of $^{85}$rb and $^{87}$rb," *Phys. Rev. A*, vol. 83, p. 053633, May 2011. 1.2

[114] M. Greiner, I. Bloch, T. W. Hänsch, and T. Esslinger, "Magnetic transport of trapped cold atoms over a large distance," *Phys. Rev. A*, vol. 63, no. 3, p. 031401, 2001. 1.2, 2.7

[115] W. Hänsel, J. Reichel, P. Hommelhoff, and T. W. Hänsch, "Magnetic conveyor belt for transporting and merging trapped atom clouds," *Phys. Rev. Lett.*, vol. 86, no. 4, pp. 608–611, 2001. 1.2

[116] S. Minniberger, F. Diorico, S. Haslinger, C. Hufnagel, C. Novotny, N. Lippok, J. Majer, C. Koller, S. Schneider, and J. Schmiedmayer, "Magnetic conveyor belt transport of ultracold atoms to a superconducting atomchip," *Appl. Phys. B*, vol. 116, pp. 1017–1021, Sept. 2014. 1.2

[117] T. L. Gustavson, A. P. Chikkatur, A. E. Leanhardt, A. Görlitz, S. Gupta, D. E. Pritchard, and W. Ketterle, "Transport of Bose-Einstein Condensates with optical tweezers," *Phys. Rev. Lett.*, vol. 88, no. 2, p. 020401, 2001. 1.2

[118] A. Couvert, T. Kawalec, G. Reinaudi, and D. Guéry-Odelin, "Optimal transport of ultracold atoms in the non-adiabatic regime," *EPL*, vol. 83, no. 1, p. 13001, 2008. 1.2, 4.1.1

[119] M. A. Naides, R. W. Turner, R. A. Lai, J. M. DiSciacca, and B. L. Lev, "Trapping ultracold gases near cryogenic materials with rapid reconfigurability," *Appl. Phys. Lett.*, vol. 103, p. 251112, Dec. 2013. 1.2

[120] C. Gross, H. C. J. Gan, and K. Dieckmann, "All-optical production and transport of a large $^{6}$Li quantum gas in a crossed optical dipole trap," *Phys. Rev. A*, vol. 93, p. 053424, May 2016. 1.2

[121] T. Middelmann, S. Falke, C. Lisdat, and U. Sterr, "Long-range transport of ultracold atoms in a far-detuned one-dimensional optical lattice," *New J. Phys.*, vol. 14, p. 073020, July 2012. 1.2

[122] J. Léonard, M. Lee, A. Morales, T. M. Karg, T. Esslinger, and T. Donner, "Optical transport and manipulation of an ultracold atomic cloud using focus-tunable lenses," *New J. Phys.*, vol. 16, no. 9, p. 093028, 2014. 1.2

[123] G. Unnikrishnan, C. Beulenkamp, D. Zhang, K. P. Zamarski, M. Landini, and H.-C. Nägerl, "Long distance optical transport of ultracold atoms: A compact setup using a Moiré lens," *Rev. Sci. Instrum.*, vol. 92, p. 063205, June 2021. 1.2

[124] M. J. Pritchard, A. S. Arnold, S. L. Cornish, D. W. Hallwood, C. V. S. Pleasant, and I. G. Hughes, "Transport of launched cold atoms with a laser guide and pulsed magnetic fields," *New J. Phys.*, vol. 8, no. 12, pp. 309–309, 2006. 1.2

[125] A. L. Marchant, S. Händel, T. P. Wiles, S. A. Hopkins, and S. L. Cornish, "Guided transport of ultracold gases of rubidium up to a room-temperature dielectric surface," *New J. Phys.*, vol. 13, p. 125003, Dec. 2011. 1.2

[126] D. Schrader, S. Kuhr, W. Alt, M. Müller, V. Gomer, and D. Meschede, "An optical conveyor belt for single neutral atoms," *Appl. Phys. B*, vol. 73, no. 8, pp. 819–824, 2001. 1.2, 2.1, 4.1.1, B

[127] S. Schmid, G. Thalhammer, K. Winkler, F. Lang, and J. H. Denschlag, "Long distance transport of ultracold atoms using a 1D optical lattice," *New J. Phys.*, vol. 8, no. 8, pp. 159–159, 2006. 1.2, 2.1, 4.1.1

[128] T. Klostermann, C. R. Cabrera, H. von Raven, J. F. Wienand, C. Schweizer, I. Bloch, and M. Aidelsburger, "Fast long-distance transport of cold cesium atoms," *Phys. Rev. A*, vol. 105, p. 043319, Apr. 2022. 1.2, 2.1, 3.2.1, 3.2.2, 4.1.1

[129] Y. Bao, S. S. Yu, L. Anderegg, S. Burchesky, D. Gonzalez-Acevedo, E. Chae, W. Ketterle, K.-K. Ni, and J. M. Doyle, "Fast optical transport of ultracold molecules over long distances," *New J. Phys.*, vol. 24, p. 093028, Sept. 2022. 1.2, 2.1, 4.1.1

[130] J. Trisnadi, M. Zhang, L. Weiss, and C. Chin, "Design and construction of a quantum matter synthesizer," *Rev. Sci. Instrum.*, vol. 93, p. 083203, Aug. 2022. 1.2, 2.1, B

[131] H. J. Patel, C. L. Blackley, S. L. Cornish, and J. M. Hutson, "Feshbach resonances, molecular bound states, and prospects of ultracold-molecule formation in mixtures of ultracold K and Cs," *Phys. Rev. A*, vol. 90, p. 032716, Sept. 2014. 1.3

[132] M. Gröbner, P. Weinmann, E. Kirilov, H.-C. Nägerl, P. S. Julienne, C. R. Le Sueur, and J. M. Hutson, "Observation of interspecies Feshbach resonances in an ultracold $^{39}$K-$^{133}$Cs mixture and refinement of interaction potentials," *Phys. Rev. A*, vol. 95, p. 022715, Feb. 2017. 1.3

[133] A. Ratkata, P. D. Gregory, A. D. Innes, A. J. Matthies, L. A. McArd, J. M. Mortlock, M. S. Safronova, S. L. Bromley, and S. L. Cornish, "Measurement of the tune-out wavelength for $^{133}$Cs at 880 nm," *Phys. Rev. A*, vol. 104, p. 052813, Nov. 2021. 1.6, 2.3.1, 3.1

[134] S. Schmid, "Long distance transport of ultracold atoms using a 1D optical lattice," Master's thesis, Leopold-Franzens-Universität Innsbruck, 2006. 2.1

[135] S. Schmid, *Dynamics of a cold tapped ion in a Bose-Einstein condenstate.* PhD thesis, Universität Ulm, 2011. 2.1, 2.7, 4.1.1

[136] R. Grimm, M. Weidemüller, and Y. B. Ovchinnikov, "Optical dipole traps for neutral atoms," vol. 42 of *Advances In Atomic, Molecular, and Optical Physics*, pp. 95–170, Academic Press, 2000. 2.3.1, 2.3.1

[137] F. Schmidt, D. Mayer, M. Hohmann, T. Lausch, F. Kindermann, and A. Widera, "Precision measurement of the $^{87}$Rb tune-out wavelength in the hyperfine ground state $F = 1$ at 790 nm," *Phys. Rev. A*, vol. 93, p. 022507, Feb. 2016. 2.3.1

[138] J. Mitroy, M. S. Safronova, and C. W. Clark, "Theory and applications of atomic and ionic polarizabilities," *J. Phys. B: At., Mol. Opt. Phys.*, vol. 43, p. 202001, Oct. 2010. 2.3.1

[139] F. Le Kien, P. Schneeweiss, and A. Rauschenbeutel, "Dynamical polarizability of atoms in arbitrary light fields: general theory and application to cesium," *Eur. Phys. J. D*, vol. 67, p. 92, May 2013. 2.3.1

[140] M. S. Safronova, B. Arora, and C. W. Clark, "Frequency-dependent polarizabilities of alkali-metal atoms from ultraviolet through infrared spectral regions," *Phys. Rev. A*, vol. 73, p. 022505, Feb. 2006. 2.3.1, 2.3.1

[141] J. E. Sansonetti, "Wavelengths, transition probabilities, and energy levels for the spectra of potassium," *J. Phys. Chem. Ref. Data*, vol. 37, pp. 7–96, Jan. 2008. 2.3.1

[142] J. E. Sansonetti, "Wavelengths, transition probabilities, and energy levels for the spectra of rubidium," *J. Phys. Chem. Ref. Data*, vol. 35, pp. 301–421, Feb. 2006. 2.3.1

[143] J. E. Sansonetti, "Wavelengths, transition probabilities, and energy levels for the spectra of cesium," *J. Phys. Chem. Ref. Data*, vol. 38, pp. 761–923, Oct. 2009. 2.3.1

[144] R. W. Boyd, "Intuitive explanation of the phase anomaly of focused light beams," *J. Opt. Soc. Am.*, vol. 70, pp. 877–880, July 1980. 2.3.2

[145] S. Feng and H. G. Winful, "Physical origin of the gouy phase shift," *Opt. Lett.*, vol. 26, pp. 485–487, Apr. 2001. 2.3.2

[146] D. A. Steck, "Cesium D Line Data." Version 2.2.1, Nov. 2019. 2.3.5

[147] D. A. Steck, “Rubidium 87 D Line Data.” Version 2.2.2, July 2021. 2.3.5

[148] T. Weber, J. Herbig, M. Mark, H.-C. Nägerl, and R. Grimm, “Bose-Einstein Condensation of Cesium,” *Science*, vol. 299, pp. 232–235, Jan. 2003. 2.3.5, 4.4

[149] T. G. Tiecke, “Properties of Potassium.” Version 1.03, June 2019. 2.3.5

[150] W. R. Smythe, *Static and Dynamic Electricity.* McGraw-Hill Book Company, third ed., 1968. 2.3.5

[151] D. J. DeTroye and R. J. Chase, “The Calculation and Measurement of Helmholtz Coil Fields,” tech. rep., Nov. 1994. 2.3.5

[152] Y. Li, G. Feng, R. Xu, X. Wang, J. Wu, G. Chen, X. Dai, J. Ma, L. Xiao, and S. Jia, “Magnetic levitation for effective loading of cold cesium atoms in a crossed dipole trap,” *Phys. Rev. A*, vol. 91, p. 053604, May 2015. 2.3.5

[153] A. Guttridge, *Photoassociation of Ultracold CsYb Molecules and Determination of Interspecies Scattering Lengths.* PhD thesis, Durham University, 2018. 2.3.5

[154] A. D. Innes, *Towards a novel platform for imaging molecules in an optical lattice.* PhD thesis, Durham University, 2023. Unpublished at time of writing. 3.1

[155] J. Mortlock, *Towards Quantum Gas Microscopy of Ultracold Molecules.* PhD thesis, Durham University, 2023. Unpublished at time of writing. 3.1, 3.2.2, 4.4

[156] K. Dieckmann, R. J. C. Spreeuw, M. Weidemüller, and J. T. M. Walraven, “Two-dimensional magneto-optical trap as a source of slow atoms,” *Phys. Rev. A*, vol. 58, pp. 3891–3895, Nov. 1998. 3.1

[157] A. J. Kerman, V. Vuletić, C. Chin, and S. Chu, “Beyond Optical Molasses: 3D Raman Sideband Cooling of Atomic Cesium to High Phase-Space Density,” *Phys. Rev. Lett.*, vol. 84, pp. 439–442, Jan. 2000. 3.1

[158] A. P. Raghuram, J. M. Mortlock, S. L. Bromley, and S. L. Cornish, “A motorized rotation mount for the switching of an optical beam path in under 20 ms using polarization control,” *Rev. Sci. Instrum.*, vol. 94, p. 063201, June 2023. 3.1, 3.2.3

[159] B. E. A. Saleh and M. C. Teich, *Fundementals of Photonics.* John Wiley and Sons, 1991. 3.2.1

[160] D. McCarron, “A Guide to Acousto-Optic Modulators,” July 2007. 3.2.1, 3.2.2, 3.2.2

[161] E. A. Donley, T. P. Heavner, F. Levi, M. O. Tataw, and S. R. Jefferts, “Double-pass acousto-optic modulator system,” *Rev. Sci. Instrum.*, vol. 76, p. 063112, June 2005. 3.2.2

[162] X.-J. Lu, A. Ruschhaupt, S. Martínez-Garaot, and J. G. Muga, "Noise Sensitivities for an Atom Shuttled by a Moving Optical Lattice via Shortcuts to Adiabaticity," *Entropy*, vol. 22, p. 262, Mar. 2020. 3.2.2

[163] G. A. Phelps, *A dipolar quantum gas microscope.* PhD thesis, Harvard University, 2019. 3.2.4

[164] T. M. Klostermann, *Construction of a Caesium Quantum Gas Microscope.* PhD thesis, Ludwig-Maximilians-Universität München, 2021. 3.2.4

[165] F. Brennecke, T. Donner, S. Ritter, T. Bourdel, M. Köhl, and T. Esslinger, "Cavity QED with a Bose–Einstein condensate," *Nature*, vol. 450, pp. 268–271, Nov. 2007. 4.1.1

[166] P. Hommelhoff, W. Hänsel, T. Steinmetz, T. W. Hänsch, and J. Reichel, "Transporting, splitting and merging of atomic ensembles in a chip trap," *New J. Phys.*, vol. 7, p. 3, Jan. 2005. 4.1.1

[167] L. R. Liu, J. D. Hood, Y. Yu, J. T. Zhang, K. Wang, Y.-W. Lin, T. Rosenband, and K.-K. Ni, "Molecular assembly of ground-state cooled single atoms," *Phys. Rev. X*, vol. 9, p. 021039, May 2019. 4.1.1, A.0.1, A.0.1

[168] S. Spence, R. V. Brooks, D. K. Ruttley, A. Guttridge, and S. L. Cornish, "Preparation of 87Rb and 133Cs in the motional ground state of a single optical tweezer," *New J. Phys.*, vol. 24, p. 103022, Oct. 2022. 4.1.1, A.0.1, A.0.1

[169] N. Hogan, "An organizing principle for a class of voluntary movements," *J. Neurosci.*, vol. 4, pp. 2745–2754, Nov. 1984. 4.1.1, A.0.1, A.0.2

[170] M. J. E. Richardson and T. Flash, "Comparing Smooth Arm Movements with the Two-Thirds Power Law and the Related Segmented-Control Hypothesis," *J. Neurosci.*, vol. 22, pp. 8201–8211, Sept. 2002. 4.1.1, A.0.1

[171] M. Kot, *A first course in the calculus of variations.* American Mathematical Society, 2014. 4.1.2, A.0.2

[172] L. D. Elsgolc, *Calculus of variations.* Dover Publications, 2007. 4.1.2, A.0.2

[173] T. Takekoshi, M. Debatin, R. Rameshan, F. Ferlaino, R. Grimm, H.-C. Nägerl, C. R. Le Sueur, J. M. Hutson, P. S. Julienne, S. Kotochigova, and E. Tiemann, "Towards the production of ultracold ground-state RbCs molecules: Feshbach resonances, weakly bound states, and the coupled-channel model," *Phys. Rev. A*, vol. 85, p. 032506, Mar. 2012. 4.3

[174] A. D. Lercher, T. Takekoshi, M. Debatin, B. Schuster, R. Rameshan, F. Ferlaino, R. Grimm, and H. C. Nägerl, "Production of a dual-species Bose-Einstein condensate of Rb and Cs atoms," *Eur. Phys. J. D*, vol. 65, pp. 3–9, Nov. 2011. 4.4, 5.3

[175] C.-L. Hung, X. Zhang, N. Gemelke, and C. Chin, "Accelerating evaporative cooling of atoms into Bose-Einstein condensation in optical traps," *Phys. Rev. A*, vol. 78, p. 011604, July 2008. 4.4

[176] A. Das, P. D. Gregory, T. Takekoshi, L. Fernley, M. Landini, J. M. Hutson, S. L. Cornish, and H. C. Nägerl, "An association sequence suitable for producing ground-state rbcs molecules in optical lattices." Pre-print, 2023. 5.3

[177] A. Impertro, J. F. Wienand, S. Häfele, H. von Raven, S. Hubele, T. Klostermann, C. R. Cabrera, I. Bloch, and M. Aidelsburger, "An unsupervised deep learning algorithm for single-site reconstruction in quantum gas microscopes," *Communications Physics*, vol. 6, pp. 1–8, July 2023. 5.3

[178] Q. Guan, S. L. Cornish, and S. Kotochigova, "Magic conditions for multiple rotational states of bialkali molecules in optical lattices," *Phys. Rev. A*, vol. 103, p. 043311, Apr. 2021. 5.3

[179] B. Capogrosso-Sansone, C. Trefzger, M. Lewenstein, P. Zoller, and G. Pupillo, "Quantum Phases of Cold Polar Molecules in 2D Optical Lattices," *Phys. Rev. Lett.*, vol. 104, p. 125301, Mar. 2010. 5.3

[180] K. R. A. Hazzard, S. R. Manmana, M. Foss-Feig, and A. M. Rey, "Far-from-Equilibrium Quantum Magnetism with Ultracold Polar Molecules," *Phys. Rev. Lett.*, vol. 110, p. 075301, Feb. 2013. 5.3

[181] Mika, "Trajectory generation with a minimum jerk trajectory." `https://mika-s.github.io/python/control-theory/trajectory-generation/2017/12/06/trajectory-generation-with-a-minimum-jerk-trajectory.html`, Dec. 2017. Accessed: 2023-06-12. A.0.1

[182] R. Shadmehr and S. Wise, *Supplementary Documents for Computational Neurobiology of Reaching and Pointing.* Cambridge, MA: MIT Press, 2005. A.0.1

[183] I. M. Gelfand and S. V. Fomin, *Calculus of variations.* Prentice-Hall, INC., 1963. A.0.2

[184] M. Stone, *Mathematics for physics.* Cambridge University Press, 2009. A.0.2

[185] E. T. Copson, *Partial differential equations.* Cambridge University Press, 1975. A.0.2

[186] S. Engelberg, H. Liu, and E. Tadmor, "Critical Thresholds in Euler-Poisson Equations," *Indiana Univ. Math. J.*, vol. 50, pp. 109–157, 2001. A.0.2

[187] Y. Deng, J. Xiang, and T. Yang, "Blowup phenomena of solutions to Euler–Poisson equations," *J. Math. Anal. Appl.*, vol. 286, pp. 295–306, Oct. 2003. A.0.2

# APPENDIX A

# Two Not-So-Brief Anecdotes on the Woes of Wondering: “Where does this come from?”

### A.0.1 Selecting a Trajectory

In the face of a wide range of transport trajectories and little to distinguish them, we turned to our colleagues in our neighbouring lab working on creating RbCs ground-state molecules in optical tweezers. They had implemented a modified version of the Minimum Jerk Trajectory to merge two tweezers [168]. This was based on an equivalent trajectory used by tweezer experiment in Harvard [167]. In both experiments the trajectories were modified to avoid parametric heating from an etaloning effect inside the acousto-optic deflectors used to move the tweezers. This effect was not relevant for conveyor-belt transport where the frequency of the acousto-optic modulators used determines the velocity of a lattice rather than the position of tweezer. Hence we used the unmodified Minimum Jerk Trajectory

$$x = x_i + (x_f - x_i)\left(10\left(\frac{t}{T}\right)^3 - 15\left(\frac{t}{T}\right)^4 + 6\left(\frac{t}{T}\right)^5\right), \tag{A.1}$$

where $x$ is position, $t$ is time, $x_i$ and $x_f$ are the initial and final positions and $T$ is the transport duration.

Using this trajectory, we successfully realised conveyor-belt transport. Satisfied that the trajectory was suitable, we too subsequently ignored the question of why use this particular trajectory over the ones used in other experiments. That is until doing analysis on data taken to characterise the effect of average speed on transport efficiency. Wanting to calculate the maximum acceleration on the atoms for a given average speed, I returned to the equation for the Minimum Jerk Trajectory. This prompted the question "I wonder where this equation comes from?" and lead to a lengthy but productive rabbit-hole of citations.

Tracing back history the Minimum Jerk Trajectory came to be used in the transport of cold atoms reveals an interesting and somewhat bizarre chain of citations. Starting with a basic internet search, the first useful result was an entry in "Mika's Tech Blog" [181] from 2017 which gave the by-now familiar equation for the Minimum Jerk Trajectory. The author recounts their own internet search for a fast and easy-to-implement trajectory for unspecified control systems. During this search they found the supplementary documents of the 2005 book "Computational Neurobiology of Reaching and Pointing" by Shadmehr and Wise [182]. Both the 2019 paper from the Harvard group [167], and the 2022 paper from Durham [168] cite the same source.

They present a somewhat lengthy derivation of a Minimum Jerk Trajectory for a specific distance and duration, partly from the first principles of calculus of variations and using integration by parts three times. However they do offer a citation for the general equation of the Minimum Jerk Trajectory, presented later. This finally leads to the start of the citation chain, the 1984 paper "An Organising Principle for a Class of Voluntary Movements" by Hogan [169]. This paper presents a mathematical model to describe the limb movements in primates. A notably directer derivation of the Minimum Jerk Trajectory is presented in the paper using an extension of the Euler-Lagrange equation, which the paper calls the "Euler-Poisson equation".

With this very unexpected discovery, my original question of "I wonder where these equations comes come from?" was answered. The primate-limb-movement paper also clarified exactly what the Minimum Jerk Trajectory minimises for, namely the jerk squared integrated over the whole trajectory. The square of the jerk is used as the limb (atoms) are stationary, thus are both accelerated and decelerated during the movement (transport). Taking the square avoids any unwanted cancellations between points where the jerk is positive and points where it is negative. The integral is used to take the total amount of jerk into account, rather than minimising the maximum jerk experienced.

The reasoning for selecting the Minimum Jerk Trajectory is however somewhat tenuous in the original paper. Hogan states that the natural limb movements of primates appear smooth and graceful and then assumes, without further elaboration that maximising smoothness is equivalent to minimising the total square jerk. Heuristically it does nonetheless make some sense to use this trajectory for transport. If jerk leads to heating and atom loss then the total jerk needs to be minimised as opposed to the maximum jerk. A later paper considered trajectories which minimise the square-integral of acceleration and snap (the rate of change of jerk) [170]. Their criteria for selecting among the trajectories was to calculate the ratio between the maximum and average velocities of the trajectories and compare those values to measured ratios. Based on this the Minimum Jerk Trajectory was found to be the best model for limb movements. However, to our knowledge, measurements directly comparing the Minimum Jerk Trajectory to other trajectories had so far not been reported in the context of cold atom transport. This led to the investigation of different trajectories presented in the main text.

### A.0.2 The “Euler-Poisson Equation”

After the ordeal of tracking down the origin, derivation and justification for the Minimum Jerk Trajectory, I thought everything was finished. However when writing up the derivation for the trajectory equations, this turned out not to be the case. Not unlike before this was the result of trying to find the origin of an equation, this time a reference for the calculus of variation equation used in the derivation.

It is presented, under the name “Euler-Poisson equation” in the appendix of the original 1984 Hogan paper [169] without citation. Although the derivation of this higher-order derivative generalisation is a straightforward extension of the same method used for the standard Euler-Lagrange equation, it rarely presented in standard text books. In fact, of the physical books available in the Durham University Library, both in 530.15 (Physics - Mathematics for Physics and Engineering) and in 515.64 (Mathematics - Analysis - Calculus of Variations), the only book to present is the Soviet-era "Calculus of Variations' by I. M. Gelfand and S. V. Fomin (1963, page 42, translated by R. A. Silverman, based on lectures given at Moscow State University) [183] which referred to it simply as the "Euler equation". Few others, e.g. "Mathematics for Physics: A Guided Tour for Graduate Students" by M. Stone and P. Goldbart [184] show the 2nd-order derivative case but not the nth order case nor do they give it any specific name.

Curiously, the Wikipedia article for Calculus of Variations does present the generalisation as the "Euler-Poisson equation" and references the above cited "A First Course in the Calculus of Variations" by M. Kot. (2014, page 71) [171] which does name the equation but leaves the derivation as an exercise to the reader (note this was published over 30 years after the Hogan paper). After a more extensive search of online databases, the only other reference I was able to find was in "Calculus of Variations" by L. D. Elsgole (1961, republished 2007, page 44) [172] which finally presented a full derivation of this Euler-Poisson equation. The provenance of the name is however still mysterious, but in the interests of time and sanity further investigations were ceased at this point.

Complicating the search is the existence of the "Euler-Poisson-Darboux equation" [185], an unrelated partial differential equation apparently used in solving classical wave equations, as well as the similarly unrelated "Euler-Poisson equation(s)" [186, 187], a set of fluid equations (themselves an extension of the Euler equation for fluids).

# APPENDIX B

# Retro-Reflected Lattice: A Not-Quite-Successful Attempt at Implementing Transport

Before setting up the transport beams as described in Chapter 3, we tried implementing transport using only one fibre amplifier in a retro-reflected lattice configuration. While we were able to transport some atoms with this setup, the efficiencies were insufficient for future experiments. This lead to adopting the two fibre amplifier configuration described in the main text.

The first implementation of optical conveyor-belt transport [126] also used only one laser, with light split into two branches using a beam splitter. An AOM in the double-pass configuration was then placed in each branch. This configuration leads to a significant loss in power due to the double-passed AOMs, as well as having less light available in the first place due to the splitting of the beam.

Instead we opted to form the transport lattice using a retro-reflected beam, inspired by a research group in Chicago also working with Cs. Their implementation was successful and is reported in [130], although with relatively low efficiencies of $20-30\%$ and over a shorter transport distance of 28cm. Light from the laser is steered directly into the chamber, significantly increasing the power in the beam over the beam-splitter configuration. The power is recycled by retro-reflecting the

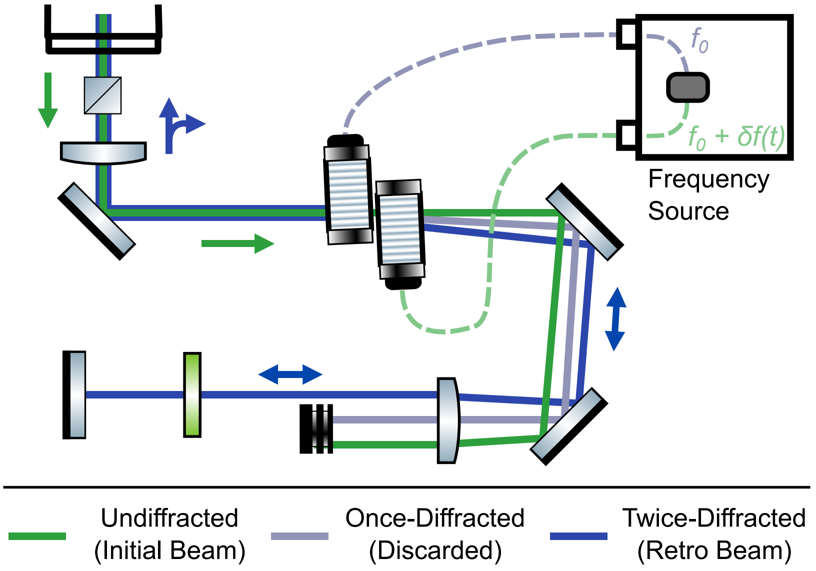

Figure B.1: Schematic of the original retro-reflected transport beam setup. Due to the retro-reflection, both AOMs needed to implement the required frequency control had to be placed in the retro beam's optical pass. This lead to a double-AOM double-pass. Component symbols are as used in Chapter 3.

initial beam to form the lattice.

However, both AOMs must be placed in the retro path to implement the required frequency control. Figure B.1 shows a sketch of the AOM setup for the retro beam. The AOMs are aligned such that light is scattered into opposite diffraction orders, $1^{\text{st}}$ for the first AOM and $-1^{\text{st}}$ for the second AOM. As before both are double-passed to ensure minimal beam deviation as the frequency is varied. Setting up this double-AOM double pass turned out to be very challenging, due to the increased complexity of having two AOMs. Additionally, the beam pointing had to be very consistent across AOM frequencies to ensure good overlap between the two transport beams.

Both AOM's are placed directly after each other, as shown in Figure B.1, such that there are three main diffraction orders. The undiffracted order (shown in green) is light unaffected by both AOMs and has the same frequency as the initial beam, the once-diffracted order (shown in blue-grey) which is light diffracted by only one AOM and hence has a frequency change of $\Delta f_{\mathrm{AOM}} = f_0$ or $\Delta f_{\mathrm{AOM}} = -(f_0 + \delta f(t))$

and the desired twice-diffracted order (shown in blue)[1].

As for the double-pass AOM setup described in Section 3.2.2, a cat's eye retroreflector is used to retro reflect the beam. It was especially important to use this method (rather than a telescope) for the retro-reflected lattice beam as, if the initial beam were to be focused, it would exceed the AOM's damage threshold. However due to the size of the AOMs, the condition that the lens is a focal length from the AOM could only be met for one AOM. We chose to align to the second AOM, which meant the frequency of the first AOM had to be kept constant.

The principle challenge when aligning this setup was correctly placing lens to avoid beam pointing deviations with frequency. What was (eventually) successful was placing two additional steering mirror after the AOMs. This allowed the once-diffracted order (equivalent ot the zeroth order of the second AOM) to be aligned along a row optical breadboard holes. The lens was thus much easier to centre on the once-diffracted, as required to parallelise the twice diffracted order for all frequency shift $\delta f(t)$ of the second AOM.

One notable feature of the retro-reflected configuration is the asymmetries in beam power. Even for a high single-pass AOM efficiency of 85%, this leads to a retro-reflected beam with a power 52% of that in the initial beam, ignoring other losses. Despite the asymmetry, this configuration will lead to a greater trap depth than splitting the light.

However this configuration still suffers from power loss due to the AOMs. This is exasperated when the second AOM is detuned away from its centre frequency, which leads to a lower diffraction efficiency. Another issue is the beam shape of the retro reflected lattice beam. Due the stringent requirements of the frequency control setup, it was not feasible to include additional beam shaping. This meant the somewhat unfavourable beam shape of the retro beam could not be corrected for, leading to reduced trap depths and hence poor transport efficiencies.

---

[1] In principle this order can contain light which was unaffected by one AOM and diffracted in to the $(-)2^{\text{nd}}$ order of the other. However due to the AOM efficiencies a negligible amount of light is diffracted this way.